NTNU
Norwegian University of
Science and Technology

Stress analysis of the structural interface between the spar and the torus in the combined wind and wave energy concept STC

Haobin Liu

Marine Technology
Submission date: June 2016
Supervisor: Zhen Gao, IMT

Norwegian University of Science and Technology
Department of Marine Technology

NTNU Trondheim
Norwegian University of Science and Technology
Department of Marine Technology – Group of Marine Structures

MSC THESIS IN MARINE TECHNOLOGY

SPRING 2016

FOR

STUD.TECHN. Haobin Liu

Structural Analysis of the Interface between the Spar and the Torus in the Combined Wind and Wave Energy Concept STC

Background:
Offshore wind energy is widely recognized as a useful renewable energy capable to satisfy the increasing energy need and to increase globally the security of energy supplies. In deep waters, floating wind turbines need to be deployed. On the other hand significant opportunities and benefits have been identified in the area of ocean wave energy and many different types of Wave Energy Converters (WECs) have been proposed. In the EU FP7 MARINA Platform Project, which deals with combined wind and wave energy devices, one novel concept, called STC (Spar-Torus-Combination) has been proposed and tested in the towing tanks of Marintek, Norway and INSEAN, Italy.

The STC concept consists of a spar floater to support a 5 MW wind turbine and an axisymmetric wave energy converter (torus) that heaves along the spar to extract energy from waves through a hydraulic power take-off system. It is moored by a three-line catenary system. In operational conditions, the torus moves along three guides attached to the spar, while in survival conditions, the torus is locked to the spar by a braking system. One of the challenges is to design the interface structure between the spar and the torus so that it can withstand the loads between the two structures during both operational and survival conditions.

The purpose of this thesis is to assess the structural responses with focus on stresses in the spar and in the rollers attached to the torus using nonlinear finite element methods and to do a comparative study of different designs of the internal structures of the spar.

Assignment:
The following tasks should be addressed in the thesis work:

1. Literature review on structural design (with focus on stiffened plates, and also structural interfaces with rollers and guides) for offshore structures. Literature review on nonlinear finite element analysis for structural contact problems.

2. Study the full-scale structural details of the spar, the roller and the torus. Establish a finite element model of these components in ABAQUS. Properly define the boundary conditions, the contact conditions and the loading conditions. Establish an analysis procedure for contact analysis with a moving torus. Perform a mesh and time step convergence study.

3. Considering one case study, discuss the spatial distribution and the time dependence of the stresses.

4. Make a variety of the designs for the internal structures of the spar and compare the maximum stresses between these designs.

5. Consider the dynamic effect of the rollers and the torus, apply the real forces converted from the measurements of the model test. Investigate the stress level of the structural components under these conditions.

6. Report and conclude on the investigation.

In the thesis the candidate shall present his personal contribution to the resolution of problem within the scope of the thesis work.

Theories and conclusions should be based on mathematical derivations and/or logic reasoning identifying the various steps in the deduction.

The candidate should utilize the existing possibilities for obtaining relevant literature.

The thesis should be organized in a rational manner to give a clear exposition of results, assessments, and conclusions. The text should be brief and to the point, with a clear language. Telegraphic language should be avoided.

The thesis shall contain the following elements: A text defining the scope, preface, list of contents, summary, main body of thesis, conclusions with recommendations for further work, list of symbols and acronyms, reference and (optional) appendices. All figures, tables and equations shall be numerated.

The supervisor may require that the candidate, in an early stage of the work, present a written plan for the completion of the work. The plan should include a budget for the use of computer and laboratory resources that will be charged to the department. Overruns shall be reported to the supervisor.

The original contribution of the candidate and material taken from other sources shall be clearly defined. Work from other sources shall be properly referenced using an acknowledged referencing system.

The thesis shall be submitted in two copies as well as an electronic copy on a CD:

- Signed by the candidate
- The text defining the scope included
- In bound volume(s)
- Drawings and/or computer prints which cannot be bound should be organized in a separate folder.

Zhen Gao
Ling Wan
Supervisors

Deadline: 10.6.2016

Abstract

The Spar Torus Combination (STC) is a typical concept which consists of a spar-type floating wind turbine (FWT) and a torus-shaped wave energy converter (WEC), which utilizes the wind energy and wave energy simultaneously. The STC concept reduces the capital costs and improves the utilization of the ocean energy. The study focuses on the interface between the spar and the torus. According to the previous numerical and experimental studies, the interface is expected to undergo extremely large wave loads . The "roller-guide" interface is designed and established in ABAQUS. Nonlinear local structural modelling of the interface is carried out in this thesis. The WEC is established to be connected to the spar cylinder with designed rollers and hydraulic supports. Rubber rollers and spring connectors are used to absorb the wave energy so that the contact stress in the interface is not significant. Different scenarios are defined to investigate the performance of the interface structure. Quasi-static analyses are performed, and the elementary dynamic effect is investigated. The results have been discussed in this thesis.

Preface

Offshore wind energy is becoming a significantly important source of renewable energy as the dramatically increasing energy demand. Due to the global warming effect, the clean energy such as wind and tidal current energy is considered as the alternative choices instead of burning coal and petroleum. Therefore, it is reasonable to consider that utilise these different energy potentials simultaneously to obtain the optimal outcome.

The Spar Torus Combination (STC) is a typical concept which consists of a spar-type floating wind turbine (FWT) and a torus-shaped wave energy converter (WEC).It has been performed that the experimental and numerical study of hydrodynamic responses of a combined wind and wave energy converter concept in survival modes in a global view. It is clear that there are good agreements between the simulation and test results of responses of motions and interface forces in the operational mode. However, several nonlinear phenomena were observed during the tests, especially in the extreme sea state in the mean water level (MWL) mode, such as slamming, Mathieu instability and vortex induced motion (VIM). Therefore, the interface mechanism design between the spar and torus is also a challenging part to ensure the serviceability and survivability of the STC concept under the extreme nonlinear sea states. Hence, the interface mechanism design and the structural configuration design become important. This paper focuses on the essential preparation study before the structural design of the interface part and an elementary structural design of the interface part between the spar and the torus. In terms of different scenarios, a nonlinear stress analysis is performed for the interface model in STC concept in ABAQUS to investigate the responses of the design.

Trondheim, 2016-6-10

Haobin Liu

Acknowledgment

I would like to express my gratitude to all those who helped me during the writing of the thesis.My deepest gratitude goes first and foremost to Professor Zhen Gao, my supervisor who has offered me many valuable suggestions in the academic studies. I do appreciate his patience, encouragement and professional instructions. He devotes a considerable portion of his time to reading my manuscripts and making suggestions for further revisions every two weeks. Also, I would like to thank Phd student Ling Wan, who gave me considerable help during the FEM modelling. He helped me to be familiar with ABAQUS and the contact theory.Without his pushing me ahead, the completion of this thesis would be impossible.

I am also greatly indebted to all my teachers who have helped me directly and indirectly in my studies. In addition, i deeply appreciate the contribution to this thesis made in various ways by my friends and fellow classmates.

Trondheim June 2016
Haobin Liu

Summary and Conclusions

The hybrid wind and wave energy converter concept consists of a spar floating wind turbine and a coaxial wave energy converter called the STC (Spar Torus Combination) concept, which has been proposed to achieve better utilization of the energy and reduce the cost of construction. However, the interface between the wave energy converter and the spar floater is expected to undergo extreme wave load in operational conditions. Therefore, an elementary interface design and a nonlinear local structural stress analysis of the interface are performed and presented in this thesis. The "roller-guide system" is deployed to connect the wave energy converter and the spar floater mechanically. The rubber rollers and hydraulic supports are used to absorb the impact energy in order to reduce the contact stress. Different scenarios are defined to investigate the performance of the interface structure. Quasi-static analyses are carried out in ABAQUS. Based on this thesis, the following conclusions can be drawn:

1. The stiffeners which are attached on the spar cylinder hull are very effective to reduce the stress and deformation of the spar.

2. The increments of stress and deformation are nonlinear for some directions of the horizontal force.

3. Larger connector stiffness achieves smaller torus displacement, but induces larger stress and deformation on the spar.

4. The stress and deformation on the spar are strongly affected by the relative heave motion of the torus. The horizontal displacement of the torus are strongly influenced by the horizontal interface force.

5. The horizontal interface force is unlikely to excite the resonance of the horizontal motion of the torus. The mass effect excites the local oscillation of the spring connector system.

Contents

List of Figures

List of Tables

Chapter 1

Introduction

Wind energy and wave energy are becoming the significant source of renewable energies in recent years. Although the large number of onshore wind turbines have been deployed rapidly, it is worth to note that the wind energy production has increased at an annual rate of 20-30% steady in report [8]. In addition, it is reported in [8] that the vast sea areas with stronger and steadier winds are available to explore, thus it is strongly recommended to employ the floating wind turbines located further from the coastline. After the first spar floating turbine was deployed in the Karmoy Island of Norway by Statoil company, an increasing number of companies began to utilize the strong wind energy potential in deeper water area[1].On account of the bright prospect of wave energy conversion in the paper [2] , it is shown that over 1000 wave energy conversion techniques are patented in Japan, North America and Europe. Wind and wave energy in the deeper water area in the sea have been exploited preliminarily.

In order to utilize the wind energy and wave energy in the vast sea areas simultaneously, the Spar Torus Combination (STC) concept involving a combination of Spar-type floating wind turbine(FWT) and wave energy converter(WEC) is considered. From the economical view, the combination concept would reduce the number of mooring line and mass of the WEC. Furthermore, it could possible to reduce the capital costs of the entire project.

1.1 Background

As with other floating structures, it is necessary to ensure the serviceability and survivability of the STC during its service life. Therefore, many structural analyses have been performed in the previous investigations. In the article [4] , some important conclusions have been obtained. Although the addition of a Torus on the Spar-type FWT decreases the standard deviation of the Spar pitch motion, the Torus increases the extreme responses on the bending moment at the spar-tower interface. Similarly, it is concluded in the report [5] that the addition of a Torus decreases the standard deviation of the STC surge and pitch motion significantly. However, due to a small heave hydrostatic stiffness of the Spar, the Torus is expected to undergo large wave loads, therefore, the interface force could be a notable problem in heave mode. What's more, in the paper [6], it is shown that the STC concept results not only in decreasing of capital investment but also in increasing the power production. This paper illustrated the detailed configuration of the mechanical connections between the Spar and the Torus,i.e. interface part, which is the focus point in the present study. Furthermore, it gave four options for defining the survival modes under extreme environmental conditions and the proper survival strategy is required to avoid significant high force in the PTO system. As the abundant previous paper indicated, it is extremely necessary to perform the further investigation of structural design and stress analysis of the interface part in the concept STC.

1.1.1 Problem Formulation

The problem emphasized in this paper is shown in the paper [12] , in the mean water level survival mode (MWL), the nonlinear phenomena such as slamming and green water have been observed. In regular wave test, it can be observed that for MWL mode, slamming was seen in heave resonance period region with wave height (H=0.04m). As well, both slamming and green water can be observed with majority of the wave periods for larger wave height (H=0.18m). It is clear that the water exit and entry of the WEC is significant under severe sea state, which will induce notable wave impact force on the structure. Consequently, the existence of slamming and green water increases the interface forces between the bodies dramatically. In addition, according to the results from paper [12] , it is obvious that the slamming increases not only the force between spar and torus in the vertical(Z-direction) but also this force in the horizontal direction due to the pitch angel when the torus is entering the water. Moreover, in irregular wave tests, slamming was observed during extreme sea states in the MWL mode while slamming seldom occurred in the SUB mode. Under extreme conditions including the extreme wind, it is necessary to point out that the strong wind increases absolute value of the vertical (Z-direction) force in minus direction, in other words, adding the extreme wind makes the effect of slamming more serious. Even though, in the SUB mode, slamming is not a severe problem, more investigation on the slamming and green water should be performed especially for the MWL mode. In a word, the interface mechanism and configuration between the spar and the torus is necessary to be investigated according to variety of sea states due to interface force and notable impact forces due to slamming.

1.1.2 Literature Survey

Since the purpose of the paper is to be structural design and analysis of the interface between the Spar and Torus in the Combination concept STC, most of all, it is vital to have a deeply understanding of the configuration of STC concept. There is an available sketch of the combined concept STC in the paper [6] as shown in Figure 1.1:

- A Spar floater is used to support a 5 MW NREL wind turbine.
- A Torus which is a donut-shape buoy can slide along the Spar freely in heave motion to extract wave energy.
- Permanent ballast is set inside the bottom of the Spar floater and an active water ballast system is installed in the Torus.
- The WEC power take-off (PTO) system is used to absorb wave power from the relative motion between the Spar and the Torus in heave.
- Bearing system is designed for limit all directions of motion except heave and yaw. End stops is used for limiting the relative heave motion between two bodies and prevent the relative yaw motion.

- Three mooring lines with clamp weights.

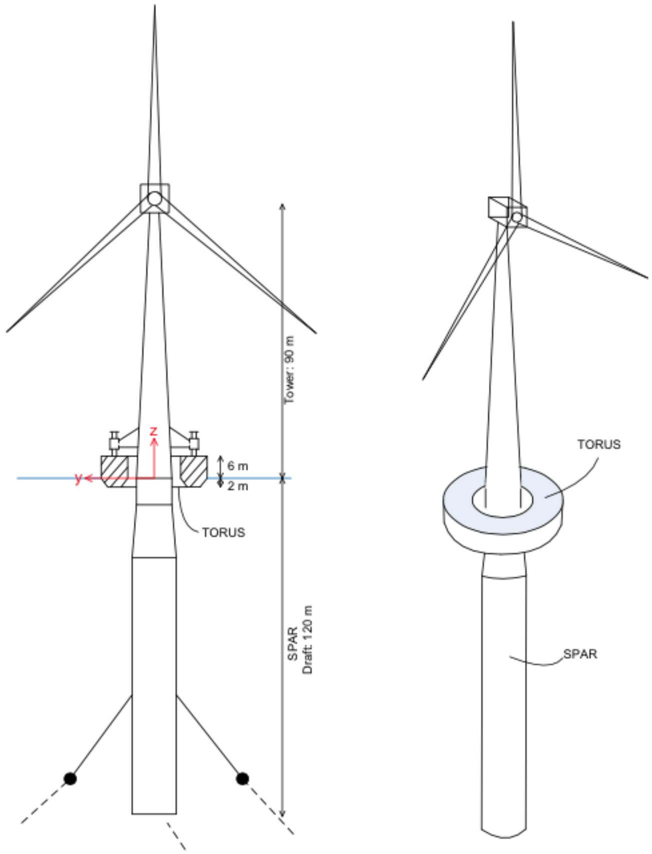

Figure 1.1: Conceptual configuration of the combined concept 'STC'(from[6])

This is a preliminary realization of the STC concept, all of the components deployed in the STC have been listed above. The properties of STC will be adjusted for specific different environment conditions, in the present study the properties are shown in the list above.

However, the dynamic and extreme responses analyses of STC with different modes have been performed in the previous investigation, in the present study, the key point is the structure of the connection between the Spar and the Torus. It is challenging to design the interface between the Spar and the Torus because of specific functions and survivability requirements. First of all, the connection between the Spar and the Torus should allow that the two bodies can freely move in heave but the two bodies move together in surge, sway, roll, pitch and yaw. Secondly, the interface is expected to experience the large loads under extreme environment conditions; therefore the interface possesses adequate strength to undergo the load effects imposed by nonlinear phenomena like slamming and green water in survival mode.

The experimental of hydrodynamic responses of a combined wind and wave energy converter concept in survival modes has been performed in [13]. In the experimental test, the STC model was downscaled by Froude scaling with a ratio of 1:50 and the model test for the survivability of the STC were performed in the towing tank of MARINTEK, Norway. Decay tests,regular wave tests,irregular waves tests and wind tests are performed orderly. Consequently, the extreme responses including motion, vertical force and horizontal force are captured for different modes. The extreme force obtained in experimental test can be utilized for designing the interface in STC concept.

In order to satisfy the requirements mentioned above, there is an elementary design of the connection between the Spar and the Torus including a main bearing system proposed in the paper [6]. The main bearing system is situated between the Spar and the Torus as shown in Figure 1.2, which is the target interface structure focused in the present study. So far, the roller-guide system is the preferred option.

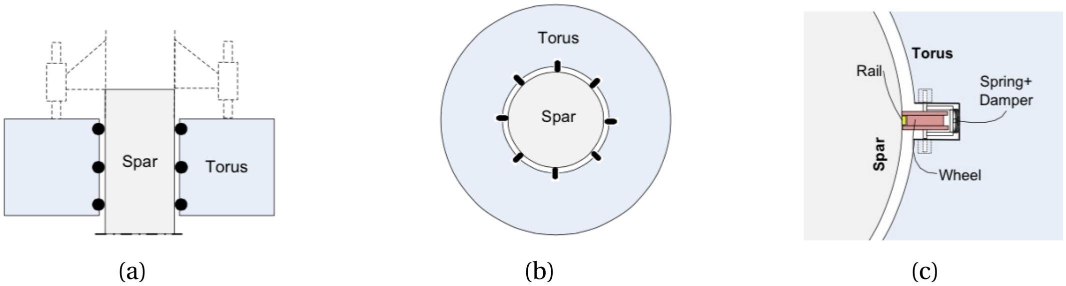

(a) (b) (c)

Figure 1.2: Main bearing system: (a) horizontal view (b) TOP VIEW and (c) WHEEL/CONTACT POINT(from[6])

1.2 Objectives

The main objectives of this Master's project are:

1. Deeply understanding of the combined concept STC and the principle of wind and wave energy absorption after related literature survey. General understanding of the STC model test and investigating the interface loads obtained in the model test by a proper consideration.

2. General realizing of the theoretical background, such as Contact in ABAQUS and nonlinear analysis in finite element method.

3. Establishing a simplified contact model in ABAQUS to investigate the appropriate material and mesh size for the further investigation of interface between the Spar and the Torus.

4. Based on the previous study, a complete structural model of the spar-torus interface is developed with proper loading conditions, kinematic constraints and contact conditions in ABAQUS.

5. Perform nonlinear quasi-static and simple dynamic stress analysis with given test scenarios in ABAQUS and discuss the results.

Chapter 2

Theoretical Background

2.1 Finite Element Method

2.1.1 Linear Finite Element Method

Finite element analysis is an approximate numerical analysis method used to solve many engineering problems such as structural mechanics, machine design and Acoustics etc. For linear finite element method (FEM) theory problems, there are three assumptions presented necessarily to simplify the calculation process, which are respectively small displacement, linear elastic material and principle of superposition apply. While the displacement is small, the equilibrium equation can be established based on the undeformed geometry. Linear elastic material implies that the strain ε are proportional to the stress σ and the material properties remain constant during the entire calculation procedure. With the superposition principle, the response of a structure by applying a system of forces is equal to the summation of the responses of the same structure applying separate forces in the system.

For plane stress problem, the finite element formulation is established as below:

Equilibrium:

$$\begin{bmatrix} \frac{\partial}{\partial x} & 0 & \frac{\partial}{\partial y} \\ 0 & \frac{\partial}{\partial y} & \frac{\partial}{\partial x} \end{bmatrix} \begin{bmatrix} \sigma_x \\ \sigma_y \\ \tau_{xy} \end{bmatrix} + \begin{bmatrix} F_x \\ F_y \end{bmatrix} = \begin{bmatrix} 0 \\ 0 \end{bmatrix} \Rightarrow \mathbf{\Delta}^T \boldsymbol{\sigma} + \mathbf{F} = \mathbf{0} \tag{2.1}$$

Compatibility:

$$\begin{bmatrix} \varepsilon_x \\ \varepsilon_y \\ \gamma_{xy} \end{bmatrix} = \begin{bmatrix} \frac{\partial}{\partial x} & 0 \\ 0 & \frac{\partial}{\partial y} \\ \frac{\partial}{\partial y} & \frac{\partial}{\partial x} \end{bmatrix} \begin{bmatrix} u \\ v \end{bmatrix} \Rightarrow \boldsymbol{\varepsilon} = \mathbf{\Delta u} \tag{2.2}$$

material law:

$$\sigma = \mathbf{C}\boldsymbol{\varepsilon} \tag{2.3}$$

After applying the natural boundary condition $\mathbf{\Phi} = \boldsymbol{\sigma}\mathbf{n}$ and the essential boundary 3+++++++6conditions $\mathbf{u} = \mathbf{u}_c$. According to the appropriate interpolation function, the displacement can be written as $\mathbf{u} = \mathbf{Nv}$, consequently, the strains and stresses are presented as $\boldsymbol{\varepsilon} = \Delta\mathbf{u} = \Delta\mathbf{Nv} = \mathbf{Bv}$ and $\boldsymbol{\sigma} = \mathbf{C}\boldsymbol{\varepsilon} = \mathbf{CBv}$ respectively. In terms of the PVD(principle of virtual displacements), the element stiffness relationship for plane stress is $\mathbf{S} = \mathbf{kv} + \mathbf{S}^o$, where $\mathbf{S}^o$is the consistent nodal force with contributions from body forces, $\mathbf{S}^o_F$, and surface tractions,$\mathbf{S}^o_\Phi$, $\mathbf{k} = \int_V \mathbf{B^T C B} dV$ is the element stiffness relationship for plane stress elements, in which $\mathbf{B} = \mathbf{\Delta N}$ and $\mathbf{C}$ is the material property matrix.

The main step of the FEM analysis can be summarized as below:

- Discretize the model structure into finite elements.
- Build the local element stiffness matrices.
- Assemble the local element stiffness matrices into global element matrix by using topology matrix.
- According to the boundary condition, a reduced matrix can be obtained.
- The global equation system $\mathbf{R} = \mathbf{Kr}$ can be solved.
- The element stresses are calculated based on displacement obtained in previous step.
- Verification of results.

However, many engineering problems include nonlinearity associated with geometrical behaviour, material behaviour or boundary condition.Therefore, the theory presented previously need to be modified to adjust the nonlinear problems.

2.1.2 Nonlinear Finite Element Method

Since the structures include nonlinear geometrical changing or boundary non-linearity in most contact problems, therefore it is necessary to follow the nonlinear load-displacement curve to obtain the solution. There are several methods to be used such as incremental procedures, iterative procedures and combined methods. Because Newton-Raphson iteration method is used in ABAQUS, hence the principle of Newton-Raphson iteration is shown below: The basic principle of nonlinear problems is to find the equilibrium state between the external load and internal element nodal forces for all steps i.e. $\mathbf{R} - \mathbf{R}_{\text{int}} = 0$.In the figure 2.1, as the example, the first and second iteration in an increment are indicated. According to the structure's initial stiffness $\mathbf{K_0}$ and $\Delta\mathbf{R}$, the displacement correction, $\mathbf{C_1}$ can be calculated. After that, the structure's configuration is updated to $\mathbf{r_1}$ based on $\mathbf{C_1}$, at the new position form a new stiffness, $\mathbf{K_1}$. Obviously, the force residual for the iteration i.e. the difference between the total applied load and the internal forces, $\mathbf{R}_1 = \mathbf{R} - \mathbf{I}_1$ is obtained. The point 1 is exactly on the curve if the residual force $\mathbf{R_1}$ is equal

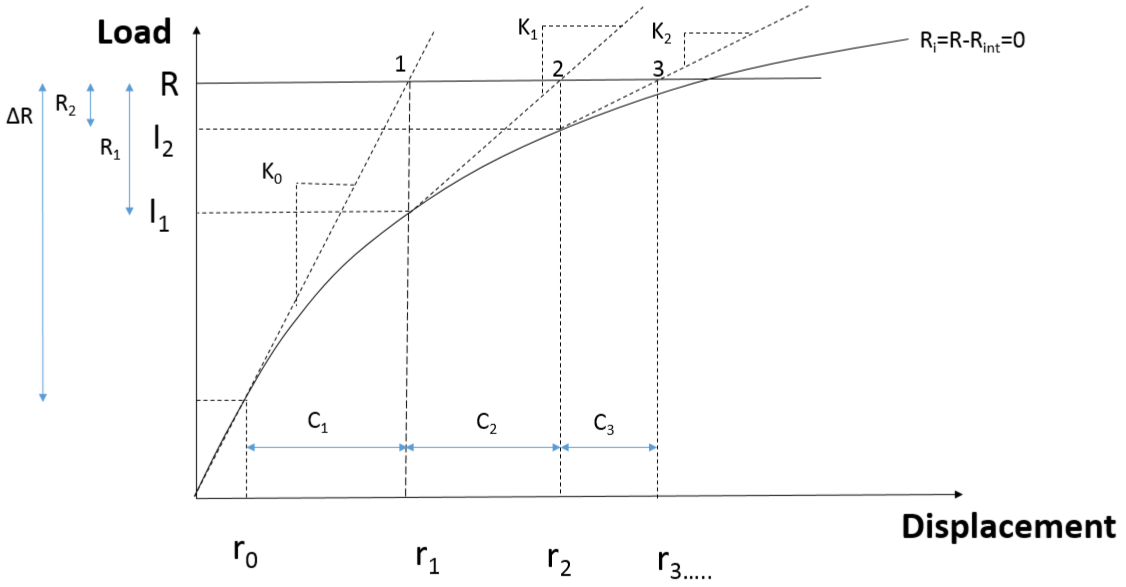

Figure 2.1: Newton-Raphson Iteration

to 0. Analogously, an updated displacement correction $\mathbf{C_2}$ and residual force $\mathbf{R}_2 = \mathbf{R} - \mathbf{I}_2$ are derived based on the new stiffness K_1. The iteration is stopped when the accuracy is acceptable, the convergence criterion usually in terms of the displacement correction :$||\mathbf{r}_{i+1} - \mathbf{r}_i|| < \varepsilon$.

In general, the iteration process can be expressed as:

$$\mathbf{r_{i+1}} - \mathbf{r_i} = \mathbf{C_{i+1}} = \mathbf{K_I^{-1}}(\mathbf{r_i})(\mathbf{R} - \mathbf{R_{int}}) \tag{2.4}$$

$$\mathbf{R} - \mathbf{R_{int}} = \mathbf{K_{I(n)}} \mathbf{C_{i+1}} \tag{2.5}$$

In each iterative step, the displacement correction $\mathbf{C_{i+1}}$ is solved based on the established $\mathbf{K_{I(n)}}$. If the condition involves the dynamic effect, the inertia term $\mathbf{M\ddot{r}}$ is supposed to be included in the equation 2.5.

In ABAQUS, the finite element models usually perform nonlinear behaviour and contain a few to large number of variables. After discretizing the virtual work equation, the equilibrium equations can be written as

$$F^N(u^M) = 0 \tag{2.6}$$

where F^N is the force component conjugate to the N^{th} variable in the problem and u^M is the value of the M^{th} variable. The elementary problem is to solve Equation 2.6 for the throughout the history of interest.

$$F(t) = \int_0^t \exp(-\lambda x)\, dx \tag{2.7}$$

According to ABAQUS theory manual [9], Abaqus/Standard commonly uses Newton's method to solve nonlinear equilibrium equations problem. Because of the convergence rates obtained in Newton's method are normally studied in ABAQUS. Assuming that after iteration i, an approximation u_i^M can be derived. Introduce c_{i+1}^M represent the difference between the approximate solution and the exact solution to the discrete equilibrium equation 2.6. This indicates that$F^N(u_i^M + c_{i+1}^M) = 0$. The left-hand side can be expanded in a Taylor series about the solution u_i^M then $F^N(u_i^M) + \frac{\partial F^N}{\partial u^P}(u_i^M)c_{i+1}^P + \frac{\partial^2 F^N}{\partial u^P \partial u^Q}(u_i^M)c_{i+1}^P c_{i+1}^Q + \ldots = 0$, assuming the u_i^M is a close approximation to the exact solution, therefore each c_{i+1}^M is small and only the first two terms will be taken into consideration. A linear system equation is obtained after neglecting the infinitesimal terms:

$$K_i^{NP} c_{i+1}^P = -F_i^N \tag{2.8}$$

where $K_i^{NP} c_{i+1}^P = -F_i^N$ is the Jacobian matrix and $F_i^N = F^N(u_i^M)$. Consequently the next approximation can be represented as $u_{i+1}^M = u_i^M + c_{i+1}^M$ and the iteration can continue afterwards. As a result of the complicated complete Jacobian matrix and expensive per iteration in Newton's method, the quasi-Newton method is introduced. The quasi-Newton method is suitable for a wide range problems, and the equation 2.8 can be written as $c_{i+1}^P = -\left[K_i^{NP}\right]^{-1} F_i^N$ in quasi-Newton method, what is more the inverse Jacobian is obtained by an iteration process.

2.2 Linear Material Theory and Nonlinear Material Hyperelasticity

In linear material theory,the stress-strain relationship is defined by Hooke's law, which is denoted by equation $\sigma = E\varepsilon$, where the σ is stress, E is elastic modulus and ε is the corresponding strain. In Figure 2.2, it is clear that the stress-strain curve becomes a straight line under elastic assumption with constant elastic modulus E.In this project, the steel material is assumed as elastic material. However, the linearity does not apply when the stress exceeds the level σ_P which is called proportionality limit. A nonlinear elasto-plastic condition prevails above this level. Consequently, the stress reaches a plateau, yield stress level, σ_P until the stress increases again. This phenomenon is denoted hardening.The dash line in the Figure 2.2 presents unloading, which occurs from a stress condition above σ_P and unloading happens along a straight line parallel with the initial linear stress-strain relationship. When the stress reaches zero, a residual plastic strain remains called ε_P.

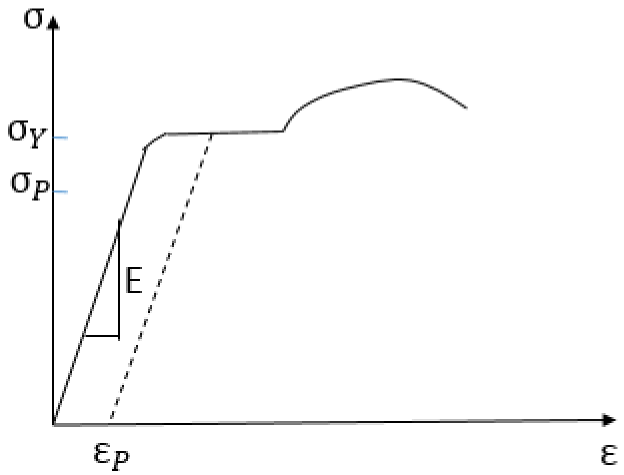

Figure 2.2: Typical mild steel stress-strain curve

For the hyperelasticity material, there is no linear region in the stress-strain curve. It is clearly shown in Figure 2.3,the rubber-like materials is defined by strain energy function instead of simply linear stress-strain relationship. What's more, the hyperelastic materials exhibit an incompressible response and the strain energy potential Moonry-Rivlin model of strain energy potential is common to be used for hyperelasticity material. In ABAQUS, there are three assumptions for hyperelastic material model.

- The hyperelastic material is isotopic and nonlinear.
- The hyperelastic material is valid for materials that exhibit instantaneous elastic response up to large strains
- The hyperelastic material model requires that geometric nonlinearity is accounted for during the analysis step.

According to the assumptions, the strain energy potential can be formulated as a function of the strain invariants. The Mooney-Rivlin model is applied in this case in ABAQUS. The strain energy is expressed as:

$$W = C_{10}(\bar{I}_1 - 3) + C_{01}(\bar{I}_2 - 3) + \frac{1}{D_1}(J^{el} - 1)^2$$

where W is the strain energy per unit of reference volume; C_{10} and C_{01} are empirically determined material constants; D_1 are temperature-dependent material parameters;$\bar{I}_1$ and $\bar{I}_2$ are the first and second deviatoric strain invariants defined as $\bar{I}_1 = \bar{\lambda_1}^2 + \bar{\lambda_2}^2 + \bar{\lambda_3}^2$ and $\bar{I}_2 = \bar{\lambda_1}^{(-2)} + \bar{\lambda_2}^{(-2)} + \bar{\lambda_3}^{(-2)}$,where $\bar{\lambda}_i = J^{-\frac{1}{3}}\lambda_i$ is the deviatoric stretches; J is the total volume ratio; J^{el} is the elastic volume ratio and λ_i are the principal stretches. Normally, the parameter D applies zero therefore the term including parameter D is neglected. Therefore, the strain energy can be expressed as

$$W = C_{10}(\bar{I}_1 - 3) + C_{01}(\bar{I}_2 - 3)$$

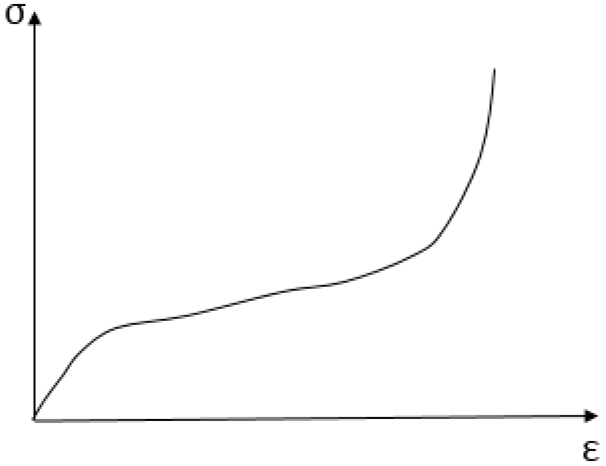

Figure 2.3: Typical rubber-like material stress-strain curve

2.3 Marine Dynamics

In marine dynamics, the waves, wind, current and tide varies with time under real ocean environment. Therefore, the dynamic response is important to be investigated. In the present study, the dynamic behaviour for a system with only one D.O.F is considered. Generally, 6 D.O.Fs are required to describe the motion of an ocean structure.

In principle, the dynamic behaviour is presented as a simple "mass-spring-damper system". It consists of a linear elastic spring with stiffness k, and a linear viscous damper with damping coefficient c. The equilibrium equation for the system can be written :

$$F_i + F_d + F_s + P(t) = 0$$

, where inertia force: $F_i = -m\ddot{u}$; damping force: $F_d = -c\dot{u}$; restoring force $F_s = -ku$ and $P(t)$ is a time-varing external force.

2.4 Contact Problem in ABAQUS

According to the [3], contact analysis is a special problem due to the severely discontinuous non-linearity during the analysis. Before establishing the FEM model, the properties of contact analysis in ABAQUS are researched. In order to understand how to define a proper intersection in modelling period.

1. In master/slave surface approach, slave nodes cannot penetrate master surface segments while nodes on the master surface can penetrate slave surface segments. Gross penetration into coarsely discretized slave surfaces can give inaccurate solutions, therefore sufficiently refined slave surface is required. The surface with softer underlying material is selected as slave surface in case of the mesh densities of two surfaces are equal.

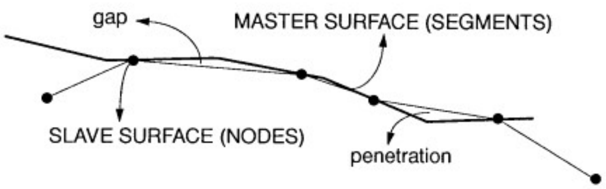

Figure 2.4: The sketch of the master-slave theory in ABAQUS/Standard (from [3])

2. In this case, "hard" contact is chosen in the pressure-Overclosure pattern, which can be explained as the definition of the contact pressure between two surfaces at a point, P, as a function of the "Overclosure" of the surface, h. In "hard contact" model,

$$p = 0, \text{for} h < 0,$$

$$h = 0, \text{for} p > 0$$

3. When defining the intersection in ABAQUS, the types of contact are divided into five categories. The finite sliding is chosen which describes contact of deformable bodies against

each other. Because finite sliding of deformable bodies against each other is the most general kinematical situation. In this mode, arbitrarily large sliding is allowed. Besides, arbitrarily large rotations and deformations of the surfaces are allowed.

Chapter 3

Material Comparison and Convergence Study

The propaedeutic finite element modelling is carried out in software ABAQUS, which is a powerful FEM software used in many nonlinear problems. Since the structural design of an interface in STC concept is a quite new topic, the material comparison and convergence test are performed to investigate the mesh density and material behaviour effect. In terms of the simplified test, the elementary choice of mesh size and material is confirmed.

3.1 Material Comparison

3.1.1 Finite Element Modelling

The material comparison and convergence test are performed on a simplified roller-plate problem in ABAQUS. These two tests are necessary to be carried out before modelling the real interface part between the spar and the torus, since the stress analysis solutions vary widely according to different roller materials and an appropriate mesh size can derive an acceptable result without enormous time consumption. Material comparison study is performed on a contact problem between a steel plate and a roller with different materials.The dimension of the plate and roller are listed in the table 3.1. The elements for roller are C3D8H type, which is 8-node linear brick element while the elements for the plate are the S4R element, which is a 4-node

Table 3.1: Data used in Material Comparison and Mesh Size Convergence Test

Dimension of plate	Length	4×4(m)
	Thickness	0.05(m)
Dimension of roller	Diameter	1(m)
	Width	0.5(m)

doubly curved thin or thick shell with reduced integration and hourglass control. The plate boundary condition (B.C.) is fixed in all the six degree of freedoms(D.O.Fs) along the edge, the inner-ring surface is kinematically coupling in six D.O.Fs with the reference point, which is located in the roller centre. Two steps are set up, the first step which is 0.1s is not only used for applying the contact force which is say 1×10^6N magnitude, but also for establishing a stable contact between the plate and roller. Corresponding to the figure 3.1, in the first 0.1s, a concentrated force -1×10^6N is applied at the reference point, where the minus sign represent the load points to negative z-axis direction. z-concentrated load is increased from 0 to -1×10^6N on the basis of ramp function and this load will be constant in the second step. After that, according to the Figure 3.2, the second step of 0.1s is implemented to make the roller rolling along the x direction from 0 to 0.785m and the turning angle is increased from 0 to 1.57m. The plate upper surface is chosen as the master surface while the outside surface of the roller is chosen as the

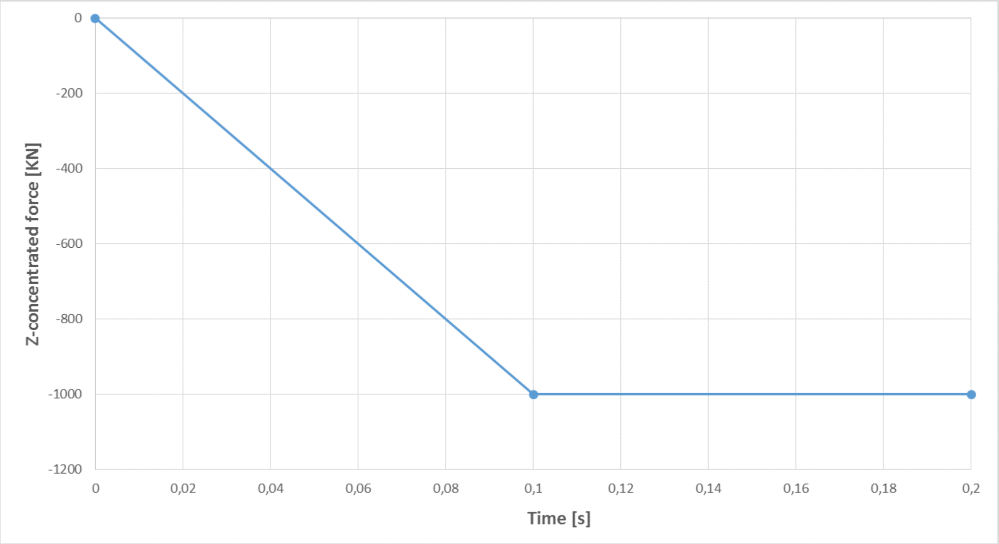

Figure 3.1: Concentrated load applied in Z direction on the reference point (roller centre)

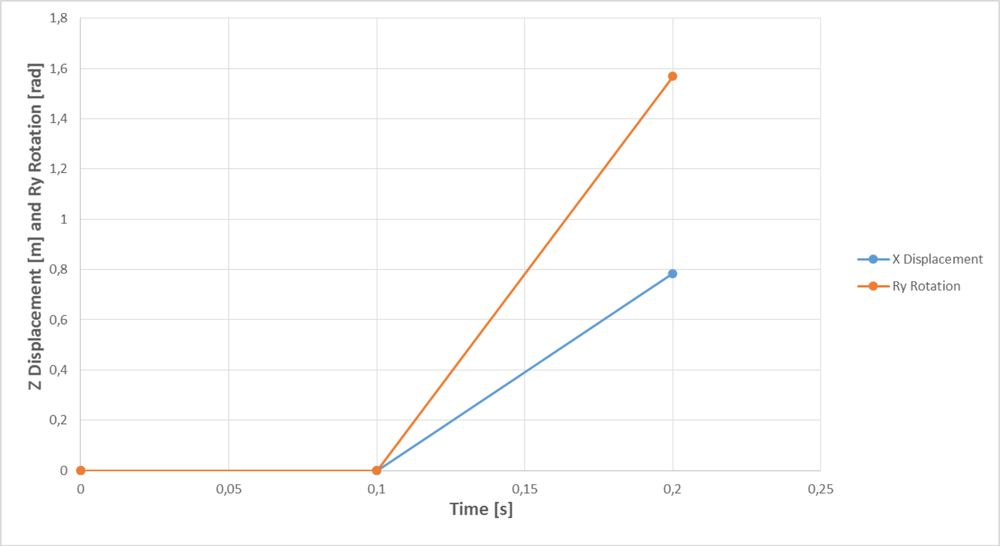

Figure 3.2: Boundary condition of X displacement and Ry rotation on the reference point (roller centre)

slave surface, it is worthy to note the slave surface should be the more finely meshed surface, therefore the mesh size of the roller should not be more than that on the plate to prevent the node penetration problem. The mesh size 0.05m for both plate and roller is chosen in material comparison study preliminary. The finite element model of the material comparison and convergence study is shown in the Figure 3.3.The Figure 3.3(a) represents the model under original condition and the Figure 3.3(b) represents the model configuration at the time 0.2s.(i.e. the end of the analysis)

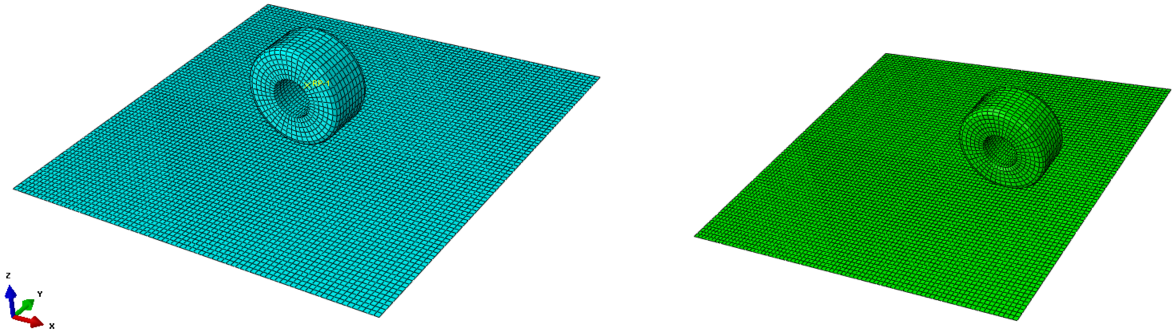

(a) (b)

Figure 3.3: FEM model of the material comparison and convergence study The model configuration at the time 0.2s

Three different materials are used in this chapter, which are Steel, Rubber 1 and Rubber 2 respectively. The detailed material properties are shown in table 3.2, In ABAQUS, the Mooney-Rivlin model is selected and different coefficients C_{10} and C_{01} are chosen corresponding to rubber 1 and rubber 2. There are three cases investigated in the material comparison study:

1. Both plate and roller apply steel material.
2. The plate applies steel material while the roller applies the rubber1 material.
3. The plate applies steel material while the roller applies the rubber 2 material.

Table 3.2: Different roller material properties

Steel	Density	7850(kg/m^3)
	Young's modulus	210(GPa)
	Poisson's ratio	0.3
Rubber1	Density	945(kg/m^3)
	C_{10}	3.2(MPa)
	C_{01}	0.8(MPa)
Rubber2	Density	1500(kg/m^3)
	C_{10}	0.84(Mpa)
	C_{01}	0.21(Mpa)

In addition, two necessary assumptions are required in the simplified model. In this chapter, the aim is to find the optimal material for the roller, no exact solution is required, hence it is possible to make assumptions which can simplify the comparison process.

1. The steel material is treated as pure linear elastic material, the plastic effect is neglected in this analysis.
2. The steel yield stress is assumed as 235MPa and the limit compression shear strength of rubber is assumed as 10MPa.
3. It is reasonable to assume the pressure uniformly distributed on the contact surface between the the steel and roller

3.1.2 Results and Discussion

The results during the time interval [0, 0.2s] are investigated. The contact areas under the same load condition corresponding to three different material rollers are shown in Figure 3.4. It is clear that the contact area is sightly larger than zero and nearly remains constant during the 0.2s for case 1 while this value reaches 0.17 m^2 and 0.27 m^2 for case 2 and case 3 respectively. Apparently, large contact areas could give rise to considerable friction force, therefore the material rubber 2 in case 3 becomes doubtful. Although the steel roller seems the optimal option because of the small contact area, further research about the average pressure is necessary since the contact area is not the only important target.

The average pressure is denoted by P which is the ratio between the contact force(F) and the contact area(A).

$$P = F/A \tag{3.1}$$

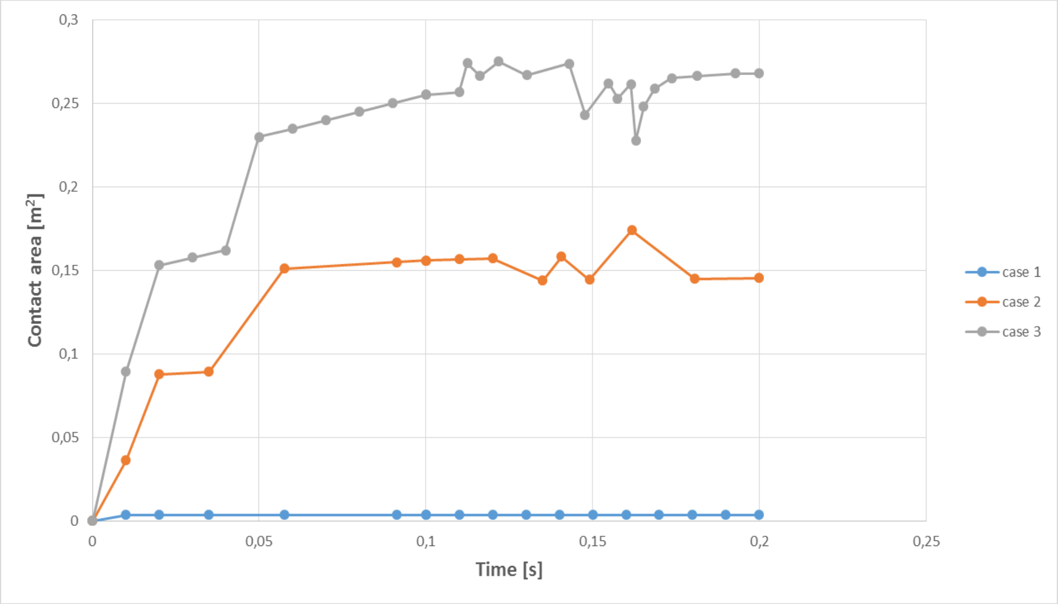

Figure 3.4: Contact area under -1×10^6N load for different material rollers

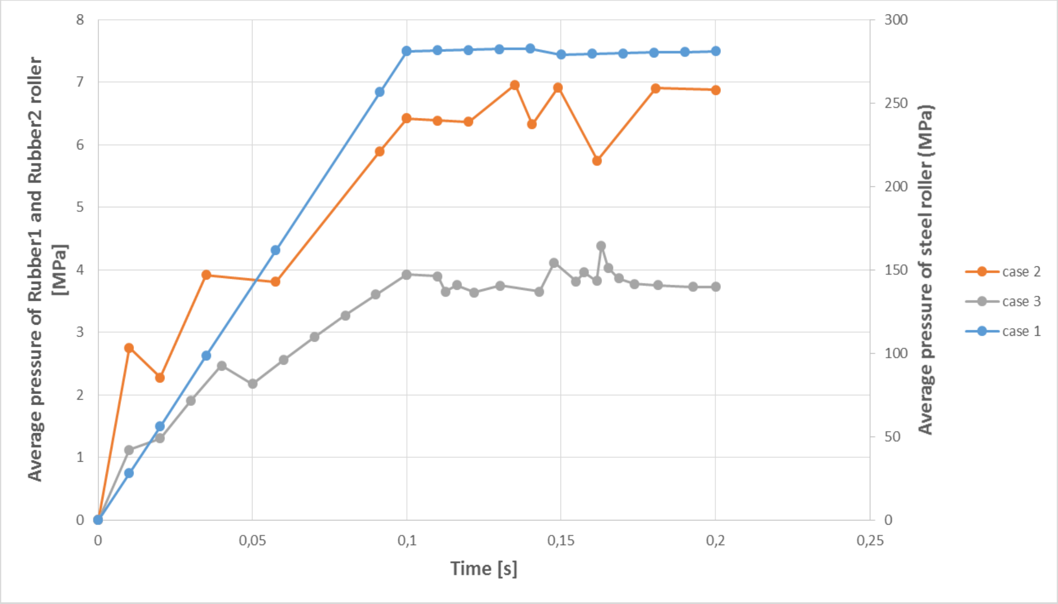

Figure 3.5: Average pressure under -1×10^6N load for different material rollers

For both of the cases, the magnitude of the contact force F is 1×10^6N, By applying the Equation 3.1, the average pressure value can be derived corresponding to time interval [0, 0.2s] for these cases. The result is demonstrated in the Figure 3.5, the maximum average pressure value for case 1 could attain to 2.75×10^8Pa during the 0.2s while the average pressure value is much smaller for case 2 and case 3 compared to case 1. For rubber1 and rubber2 roller, the maximum average pressure is 7.5×10^6 and 4.4×10^6 respectively during the analysis. The solutions are summarized in Table 3.3, in terms of the solutions in table, it is worthy to note that although the maximum contact area in case 1 is very small, the maximum average pressure has exceeded the steel yield stress assumed before. Analogously, in case 3, in spite that the maximum average pressure is acceptable, the maximum contact area is non-negligible since the width of the roller is only 0.5m. Therefore, the best way to find the appropriate material is making a compromise among these three cases.The rubber 1 material in case 2 is justifiable to be chosen for the roller material because rubber 1 has neither enormous average pressure nor immense contact. In addition, although the rubber1 material is assumed incompressible, the compression shear stress on the roller could give rise to collapse problem. The maximum shear stress at the time step 0.2s are investigated. The values of shear stress on roller in xz-direction and yz-direction are of interest and both of their values and locations are shown in Table 3.4.

Table 3.3: Results of contact area and average pressure for three cases

	case1	case2	case3
Maximum contact area[m^2]	3.6×10^{-3}	0.17	0.27
Maximum average pressure(Pa)	2.75×10^8	7.5×10^6	4.4×10^6

As can be seen from the Table 3.4, the values of shear stress for both directions are smaller than limit compression shear stress. Hence, the material rubber1 is selected to be the roller material in later study.

Table 3.4: Maximum shear stress on roller at time step 0.2s

	Magnitude(Pa)	Location on roller	Limit compression shear stress(Pa)
xz-direction shear stress	9.65×10^5	element14,node5	1×10^7
yz-direction shear stress	1.15×10^6	element14,node46	1×10^7

3.2 Mesh size Convergence test

In general, the mesh size and time parameter affect the solutions greatly in ABAQUS, for this reason, convergence test for mesh size is performed in this chapter. The convergence test is employed to find the optimal mesh size which helps the ABAQUS solver converge to the correct solution while minimizing the computer resources expended.

In convergence study, the same FEM model is used as material comparison study. However, the displacement boundary condition provides a more stable numerical calculation environment, consequently the initial 0.001m z-displacement is applied in the first analysis step instead of the -1×10^6N z-force used in previous section.The applied small displacement in the first 0.1s can steady the contact during the analysis, because it is likely to produce errors in ABAQUS in case of adding all the loads and boundary conditions in one step for contact problems. The updated initial boundary condition is shown in Figure 3.6 and the other properties are exactly identical to previous model. The boundary conditions of x-displacement and Ry-rotation are not changed, which is shown in Figure 3.2.

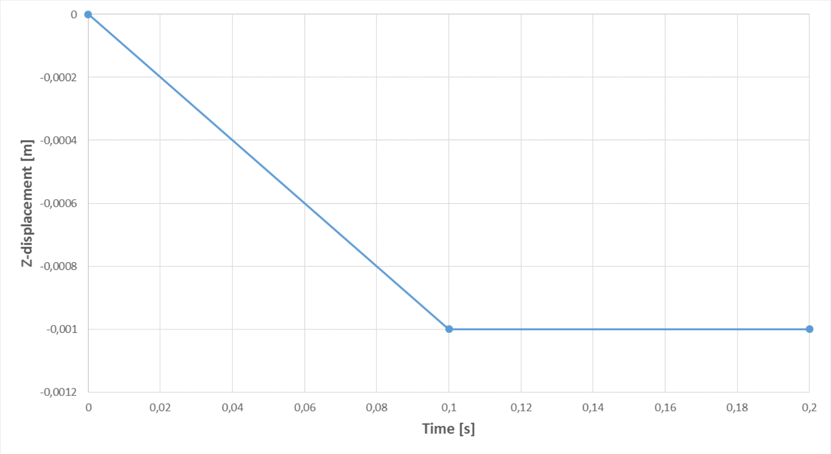

Figure 3.6: Boundary condition of Z-displacement on the reference point(roller centre)

In mesh size convergence test, different mesh density was applied. The mesh size m1 of the elements on the plate alters from 0.25m to 0.025m while the mesh size m2 of the elements on the roller alters from 0.15m to 0.025m. The detailed mesh size parameters for both the plate and roller are exhibited in Table 3.5. As mentioned before, the mesh size on the roller should not be more than that on the plate (i.e. the mesh on roller should be more refined.) Therefore, there are many bars in Table 3.5, which represent the results are inconsistent with the rule above. The results at the time step 0.2s are investigated in mesh size convergence study. The maximum Von Mises stress on the integration point of the quadrilateral element on the contact surface on the plate is shown with different mesh size m1 and m2. The results are presented in table 3.5.

Table 3.5: Maximum Von Mises stress for different mesh size combination

mesh size of plate[m] / mesh size of roller[m]	0.250	0.150	0.100	0.075	0.050	0.025
0.150	3.92×10^7	4.52×10^7	-	-	-	-
0.100	7.56×10^7	8.92×10^7	9.31×10^7	-	-	-
0.075	7.79×10^7	9.24×10^7	9.69×10^7	9.78×10^7	-	-
0.050	8.60×10^7	1.02×10^8	1.06×10^8	1.07×10^8	1.13×10^8	-
0.025	8.69×10^7	1.02×10^8	1.07×10^8	1.08×10^8	1.15×10^8	1.20×10^8

Consequently, the results are plotted in Figure 3.7. In order to assess the results intuitively. Sees from the figures below, the result of maximum Von Mises stress is approaching conver-

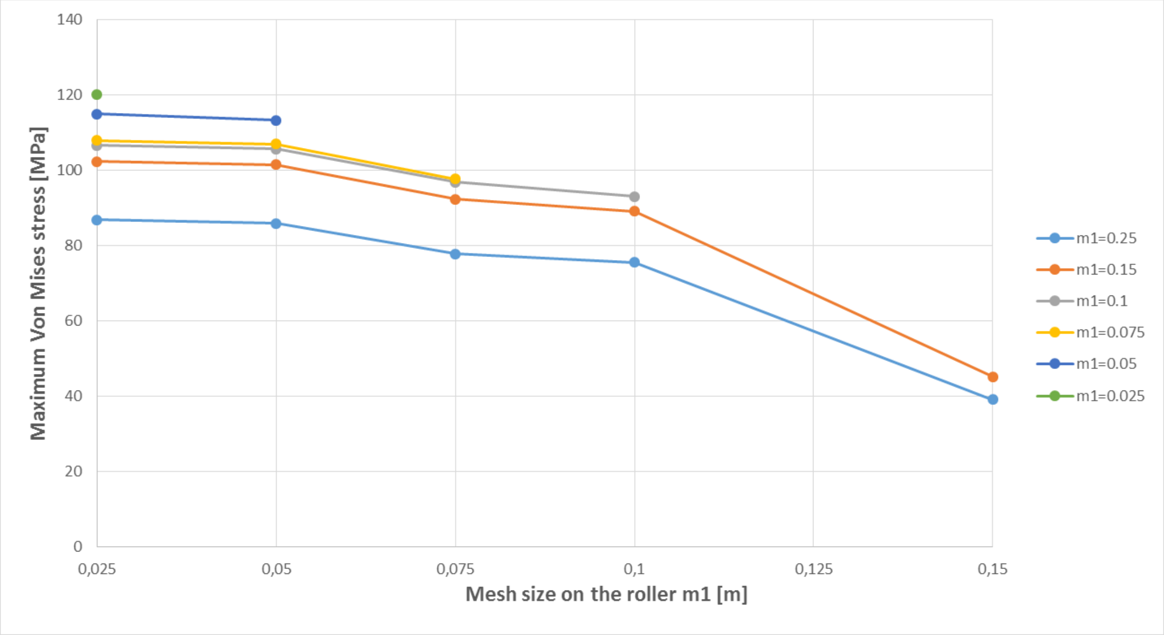

Figure 3.7: Maximum Von Mises stress under different mesh size combinations

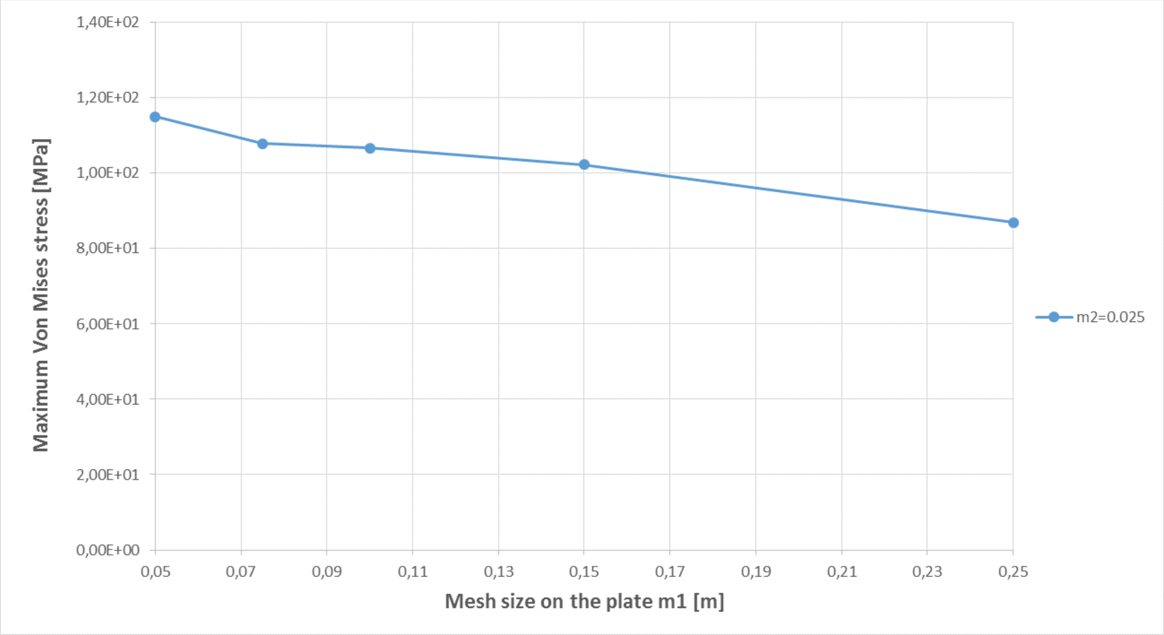

Figure 3.8: Maximum Von Mises stress under different mesh size m1 and fixed mesh size m1=0.025

gence with the decreasing mesh size of roller. What's more, the result discrepancy between the m2=0.05m and m2=0.025m is acceptable. In order to save the time consumption and computer resource, the mesh size of roller can be determined as m2=0.05m tentatively. Then the mesh size of roller m2=0.025m is fixed and the trend of varying m1 is shown in Figure 3.8. Apparently, m1=0.05m is the optimal option because the results deviation between the m2=0.05 and m2=0.025 is acceptable and the calculation time consumption is decreased dramatically in case of selecting m2=0.05m. Finally, the mesh size on both roller and plate are selected as 0.05m.

Chapter 4

Elementary Interface Design

In this chapter, an elementary interface design for the spar-torus combination concept is performed, and quasi-static nonlinear finite element analysis including geometrical nonlinear and material nonlinear is carried out for the interface design. Different scenarios are applied to investigate the effect factors of the interface design. The results are discussed and some conclusions are made, which can be used to properly design the interface.

4.1 Introduction of the interface mechanism

From the previous chapter, a simplified roller-plate problem has been established in ABAQUS in order to decide the proper mesh size and structural material. After the preparation work, the real interface part of the Spar and Torus will be designed and established in ABAQUS in this chapter.

Unfortunately, no much information or previous studies are available to design the interface between the Spar and Torus. Therefore, a coarse design is determined according to three principles.

1. The interface can uniformly undergo the wave load and the load acts on the interface, In other words, there is no severe stress concentration in the interface part.

2. Avoiding the direct contact between the Spar and Torus to ensure the normal operation of STC concept.

3. Reducing the contact area and friction force between the Spar and Torus.

Table 4.1: STC concept dimensions

Spar and Tower	Spar lower cylinder	Diameter(m)	10
		Length(m)	110
	Spar upper cylinder	Diameter(m)	6.45
		Length(m)	20
Torus	Height(m)	8	
	Outer diameter(m)	20	
	Inner diameter(m)	8	

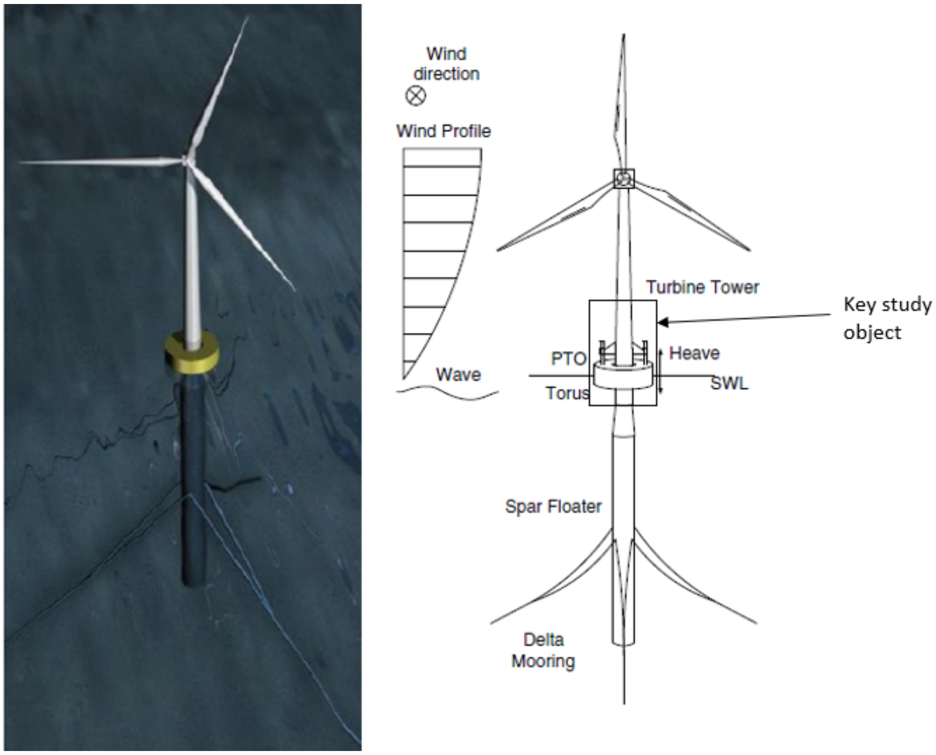

Figure 4.1: Spar torus combination (STC) concept (from [13])

The main dimensions of STC concept in the present analysis are shown in Table 4.1, and the spar torus combination concept model is shown in Figure 4.1. Since this thesis only deals with the interface part of the STC concept, only the interface part, which is shown as "Key study object" in Figure 4.2, is designed and established in ABAQUS. It is clear that in the Figure 4.3, a local model of the spar cylinder with a length of 20m corresponding to the spar upper cylinder is investigated.Based on the principles above, a roller-guide system is deployed, which allows the relative heave motion of the Torus with respect to the Spar. Nine rollers are used, and from

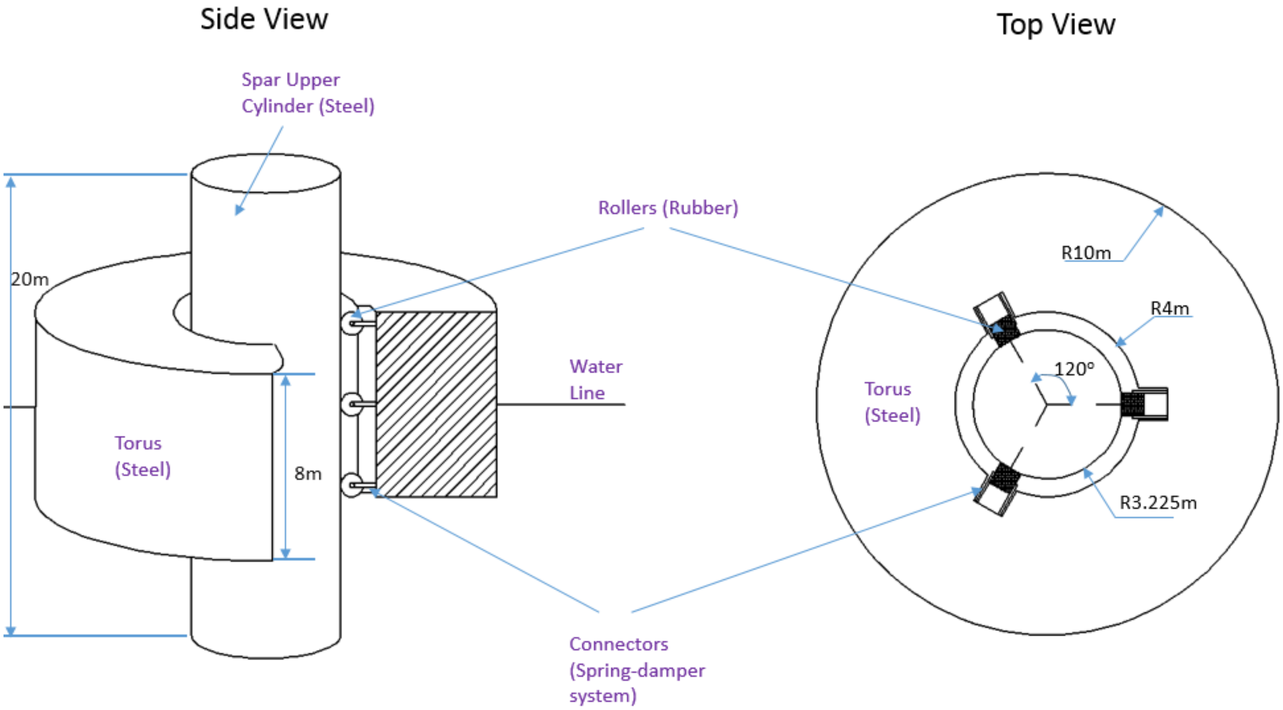

Figure 4.2: The local model of the spar-torus interface part

the side view, each three rollers are uniformly distributed on the Torus. From the top view, each three rollers are located 120 degrees apart with respect to the spar cylinder central line. Three flat tracks with 1m width are applied to the spar cylinder to ensure steady rolling condition, and the diameter of rollers are 1m. In this paper, three rollers on each track are considered, because this will be a minimum number to avoid direct contact between the Spar and Torus if one of the wheels fails. Spring-damper connectors are used to connect the rollers and the torus. The shaft of rollers are installed at one end of the connectors and can roll on the spar cylinder surface. The connectors are pre-compressed when the WEC is installed on the spar cylinder, which can ensure the stable contact between the rollers and the spar cylinder. If necessary, baffle plates can be installed on the edge of the flat track to avoid relative horizontal motion between the rollers and spar. However, the limited stroke length should be defined for the connector to avoid the impact between the torus and the spar. An end stop system should be deployed to achieve the normal operation of the connectors. It is challenging to design the interface due to the expected critical contact stress.

4.2 Numerical modelling of the interface

According to the mechanism of the interface part, the modelling of the Spar-Torus interface is completed in ABAQUS. The model of the interface part is introduced by using figures and some explanations.In Figure 4.4, it is clear that the local interface model of the STC concept consists of a spar cylindrical hull, nine rollers, and nine connectors.The materials of the spar and the torus are steel and rubber respectively, which have been determined previously. The material parameters and element type description of spar and rollers are shown in Table 4.2. The procedure of modelling the interface part is presented in terms of the different modules in ABAQUS. Besides, the global coordinate system is shown in Figure 4.3.

Table 4.2: Material parameters and element type description of spar and roller

Spar(Steel)	Density	7850(kg/m^3)
	Young's modulus	210(GPa)
	poisson's ratio	0.3
	Element type	S4R, 4 node doubly curved shell element
Roller(Rubber)	Density	945(kg/m^3)
	C_{10}	3.2(MPa)
	C_{01}	0.8(MPa)
	Element type	C3D10, 10 node quadratic solid element

- The different parts of the Spar-Torus interface are assembled after each part has been separately established. Regarding this design, the nine rollers are assembled at three levels along the Z-axis direction, with three rollers on the upper part of the Torus, three rollers on the middle part of the Torus, and three rollers on the lower part of the Torus. In Figure 4.3, each three rollers are located 120 degrees apart with respect to the spar cylinder central line.
- The simulation is divided into two phases. The first 0.2s is used to establish the stable contact between the roller and spar, and obtain the expected load amplitude because the simulation cannot normally operate if the required load rises dramatically without any transition. The initial time increment size for both two phases is 0.01s.
- In the interaction module, the contact property , kinematic coupling, and spring connector are established for interface model. The properties of contact condition and spring

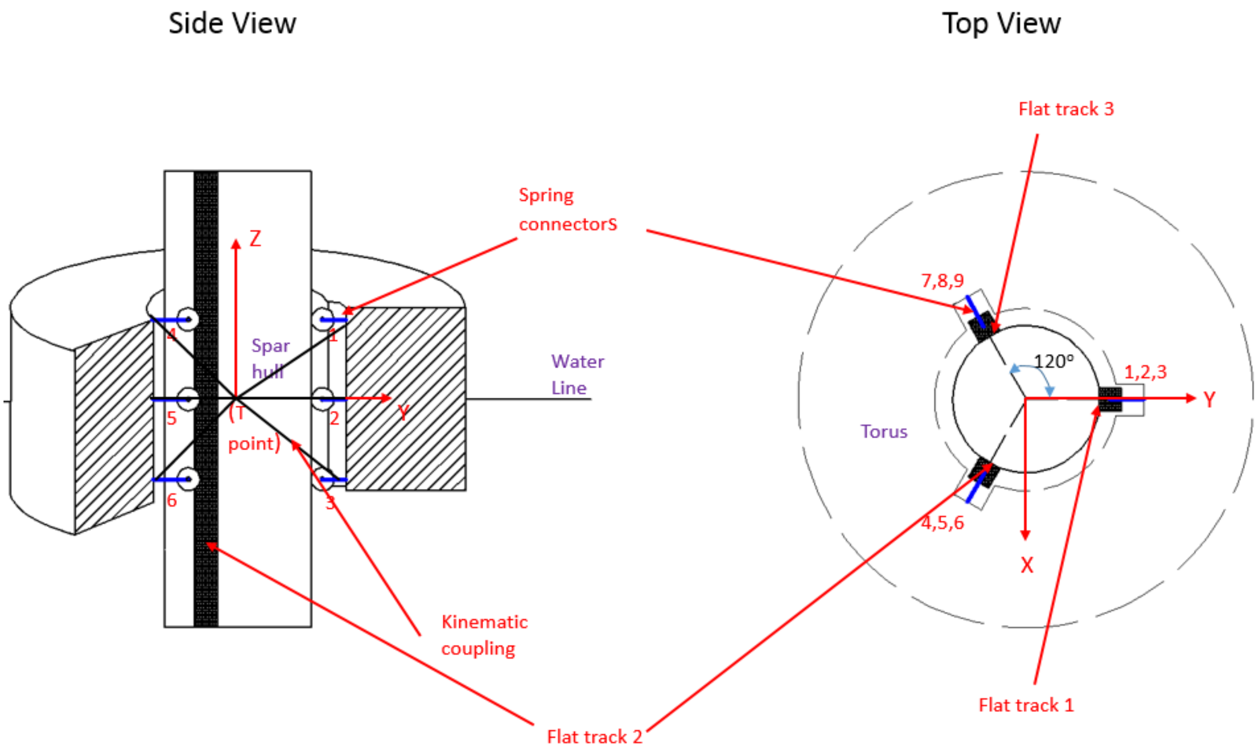

Figure 4.3: The sketch of spar-torus interface part modelling (showing spar hull, rollers, connectors, coordinate system and kinematic couplings)

connector are shown in Table 4.3. According to [11], tangential and normal contact are established between the flat track of the spar hull and the outer surface of rollers. The flat track is selected as master surface and the roller outer surface is slave surface. The spring connectors are established between the center of rollers and the corresponding end point on the torus, which is shown in Figure 4.4.It is significant that the spring connectors are only active in their axial direction. In other words, there is no relative displacement between the two ends of the connectors except in axial direction. Furthermore,it is worth noting that one end of the spring connector is pinned on the roller center so that the rollers can roll on the flat track of the spar hull. The other end of the spring connector is rigidly connected to the inner ring of the torus. This is the reason why the torus is not included in the model. Rather,the torus is taken into consideration by adding B.C on the T point, which is shown in Figure 4.4. T point represents the center of the torus part, which is kinematically coupled with the nine end points of connectors located on the torus. Moreover, kinematic couplings are established between the roller centers and the inner surface of

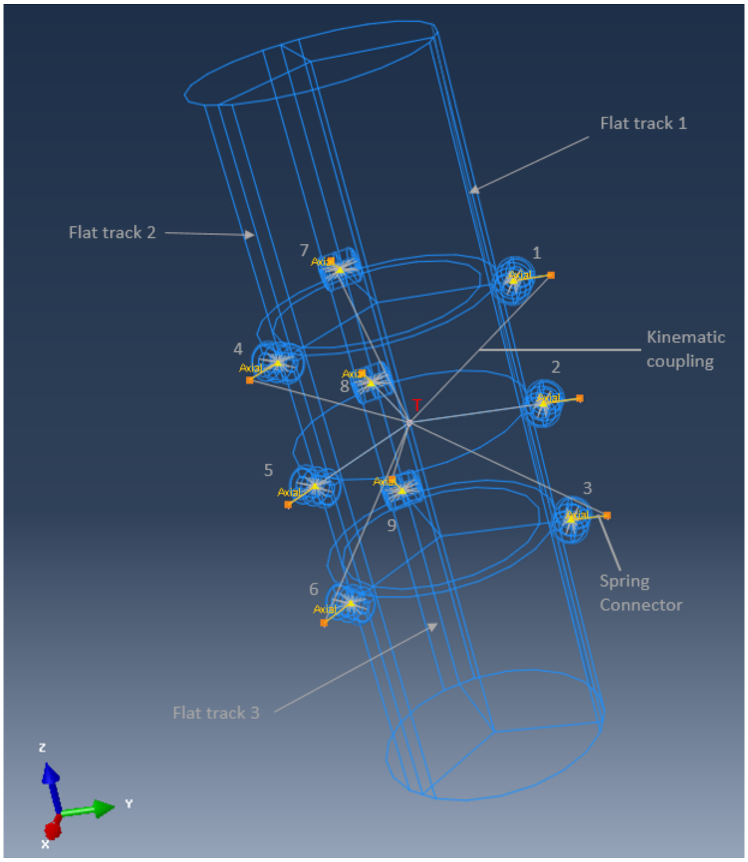

Figure 4.4: Wireframe layout of Spar-Torus interface part modelling

the rollers. The roller centers are control points, which lead the rollers to move in the 6 D.O.Fs. Basically, The T point controls the load and the motion of spring connectors' end points on the torus, and the motions of rollers follow its centers in 6 D.O.Fs.

Table 4.3: Properties of contact and spring connector

Contact	Tangential behavior	Friction formulation:Penalty. Friction coefficient:0.3.
	Normal behavior	Pressure-Overclosure:"Hard Contact". Constraint enforcement method:Penalty(standard)
Spring	Elasticity	
	Stop	
	Reference length	

- The load is added to the T point and the T point is free to move along the load direction and Z-direction. Regarding the roller center, it is free to move in three translations and roll along the flat track of spar hull under corresponding specified rotation parameter.

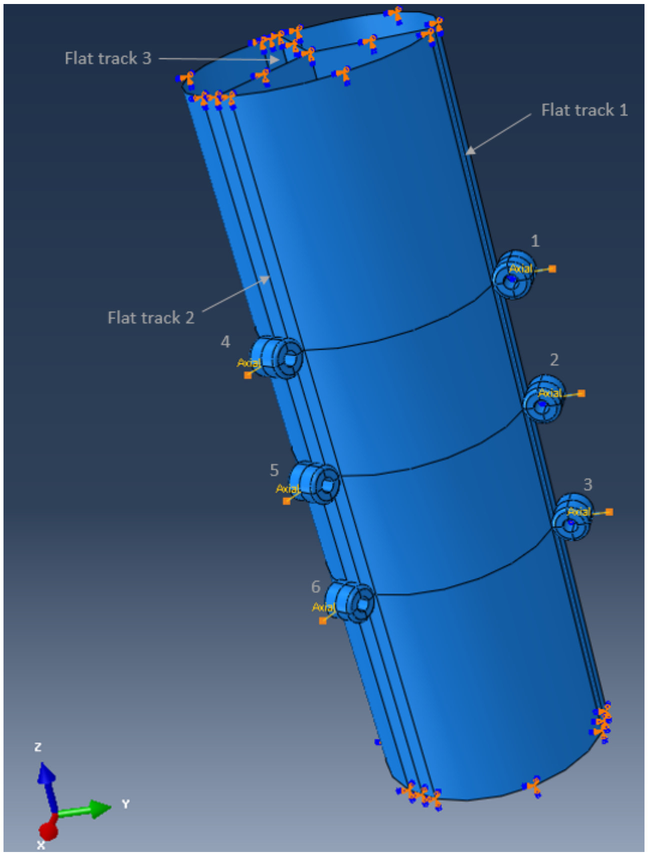

Figure 4.5: Shaded layout of Spar-Torus interface part modelling

In other words, the motion of roller center in connector axial direction is free, and the displacement of roller center only depends on the contact condition. In Figure 4.5, it can be seen that both of the top and bottom of the spar cylinder are fixed in 6 D.O.Fs, since only static local loading situation is considered so far.

- It is challenging to decide the mesh strategy since it is almost impossible for computer to calculate if the 0.05m mesh size is used for whole model. It is definitely time consuming and resource challenging. Therefore, according to [10], only the contact surface uses the 0.05m mesh size and the rest part of the spar uses coarser mesh. In Figure 4.6, it is clear that the mesh size of flat track area and the rollers are 0.05m, and the area between two flat tracks uses transitional mesh size on the curve side because this area is not significant in this simulation. The mixed mesh size can ensure the accuracy of the solutions and save the time of calculation.

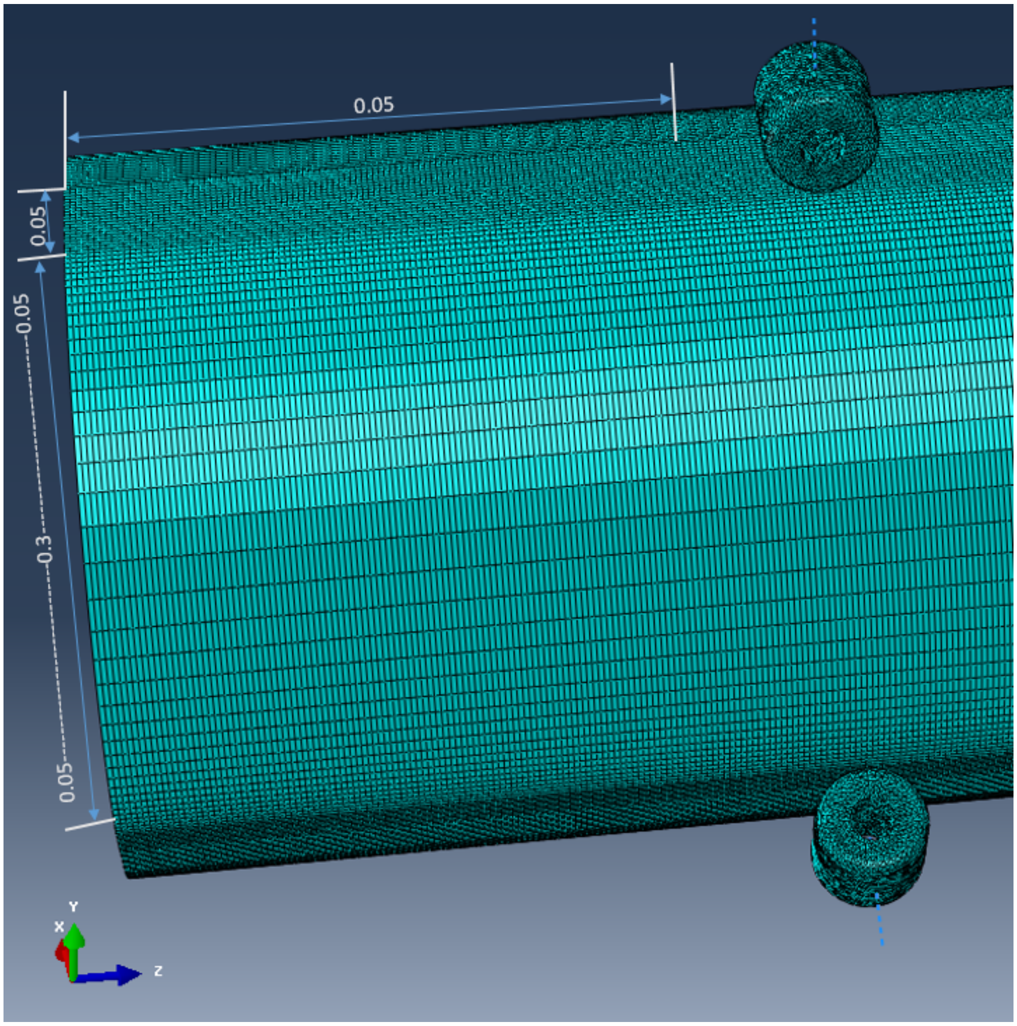

Figure 4.6: Mesh strategy for spar and rollers

4.3 Scenarios

Generally, the STC concept utilizes offshore wave energy and wind energy to produce electricity. In the STC concept, the torus moves along the flat track of the spar cylinder because of the wave load. This is to say, the torus is the main structure, which absorbs the wave load, and then the load is transferred on the rollers and spar through the spring connectors. According to the previous numerical simulations and model tests , the horizontal interface force could become significant, besides the turning moment plays an important role on structure responses. Therefore, different scenarios are defined to evaluate the performance of the interface part of the STC concept:

- the effect of different structural configurations of the spar cylinder when other conditions are fixed, such as loading magnitude and direction, spring connector properties and spar thickness;
- the effect of different horizontal interface force amplitudes and directions corresponding to different sea states. Similarly, other properties are fixed in order to investigate the effect of different loading conditions. The effect of different turning moment amplitudes and directions on the structure is investigated afterward;
- the effect of different spring connector properties under invariable loading condition and spar configuration;
- the effect of different flat track thickness under changeless loading condition and connector properties.

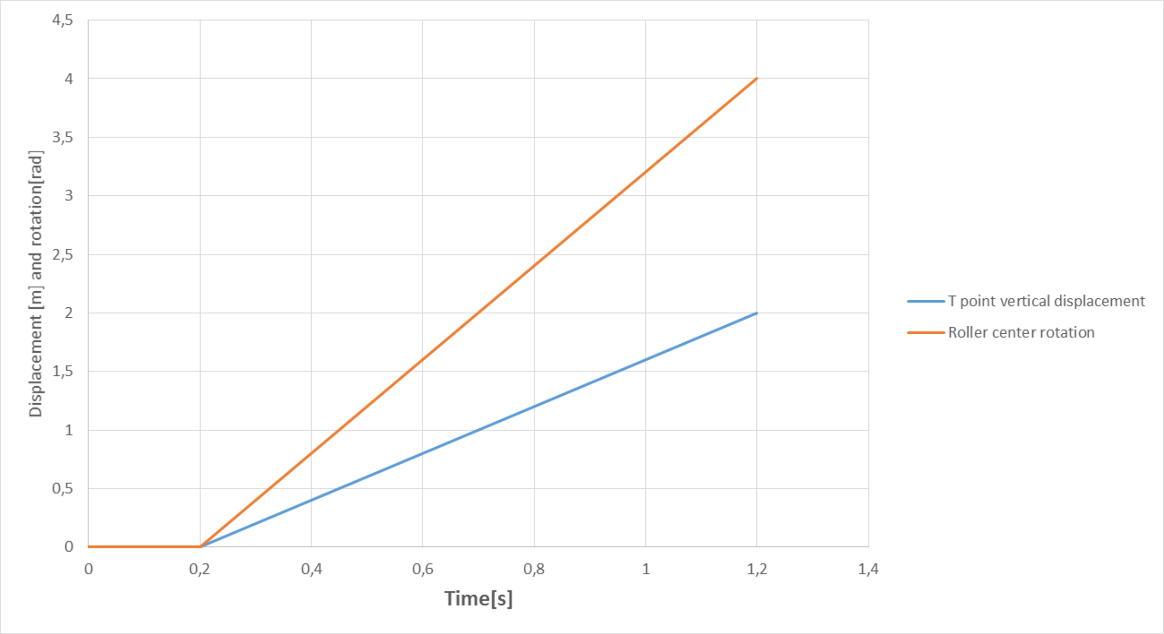

Figure 4.7: Boundary conditions to simulate the rolling process

It is necessary to apply proper B.C.s in this study to simulate the rolling process correctly. The Figure 4.7 illustrates the B.C.s applied in this study, and the rotation D.O.Fs of the T point are fixed. What's more, the X-direction translation of T point is 0 while the Y-direction translation is free, and the T point moves vertically from 0 to 2m in one second. Simultaneously, the rollers rotate 4 rad in this one second along the flat track to avoid relative sliding due to vertical motion of T point. Only the rotation with respect to its central lines is free for rollers when rotation D.O.Fs are fixed. Consequently, the scenarios are shown in a clear list.

1. Different spring connector properties are considered in this study. The detailed spring properties are shown in Figure 4.8, The spring connector is linear between the length of 0m and 2m, and the length of the spring is 2m in its neutral position. The spring connector original length is 1m without any load, and the spring can be compressed or extended under wave load. The working range is from 0.225m to 1.775m to avoid the situation that the torus and the spar influence each other. Apparently, the pre-compressions exist under the initial spring length, the corresponding pre-compressions for Spring1, Spring2, Spring3 are -1000kN, -750kN and -500kN respectively.The minus sign representing the spring connector is compressed. Consequently, the stiffness are 1000kN/m, 750kN/m and 500kN/m for Spring1, Spring2 and Spring3 respectively.

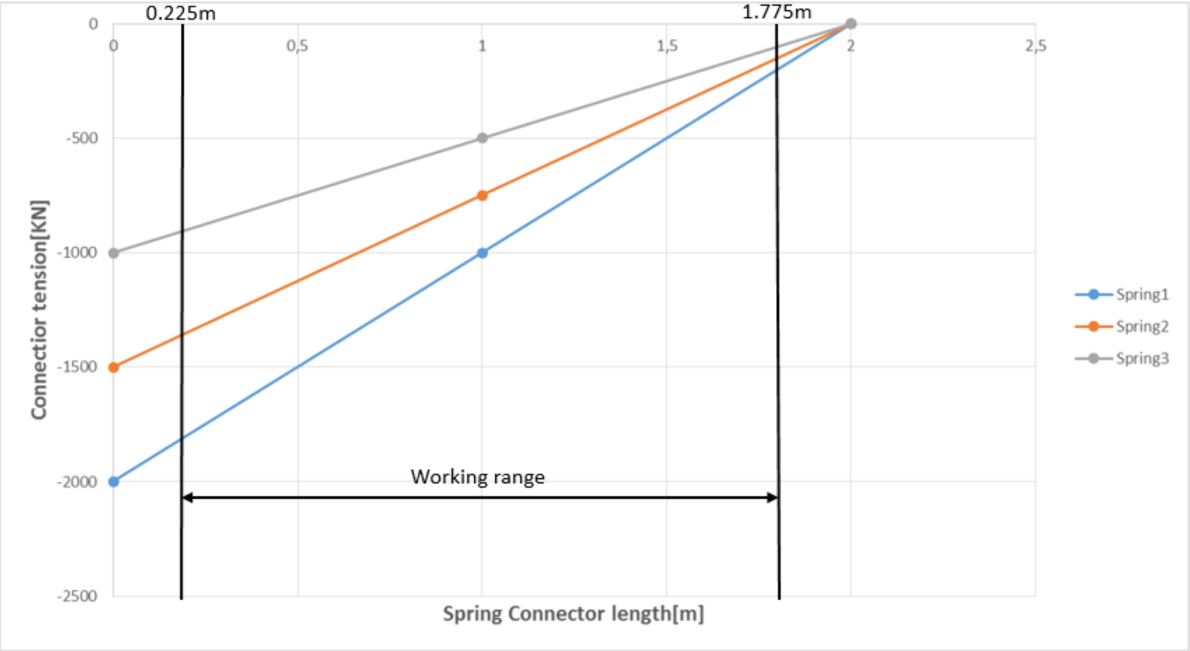

Figure 4.8: Spring connector properties

2. Regarding the horizontal interface forces, different levels and directions are applied to the simulation. In the present quasi-static study, it is assumed that

$$F^{external\ force} + F^{interface\ force} = 0$$

in the local interface model system, therefore, the interface force which is obtained in a previous model experiment can be directly added to the T point without considering the torus mass and damping parameters. If the mass of the torus is considered in the future dynamic analysis, then the equilibrium should be

$$F^{external\ force} + F^{interface\ force} = ma$$

In terms of the previous studies, the amplitudes of the horizontal interface forces could reach approximately 2000kN. Therefore, in Figure 4.9, five different horizontal force levels from 500kN to 2500kN are applied to the T point in the global Y-direction, and both +/- directions are taken into account in this study.

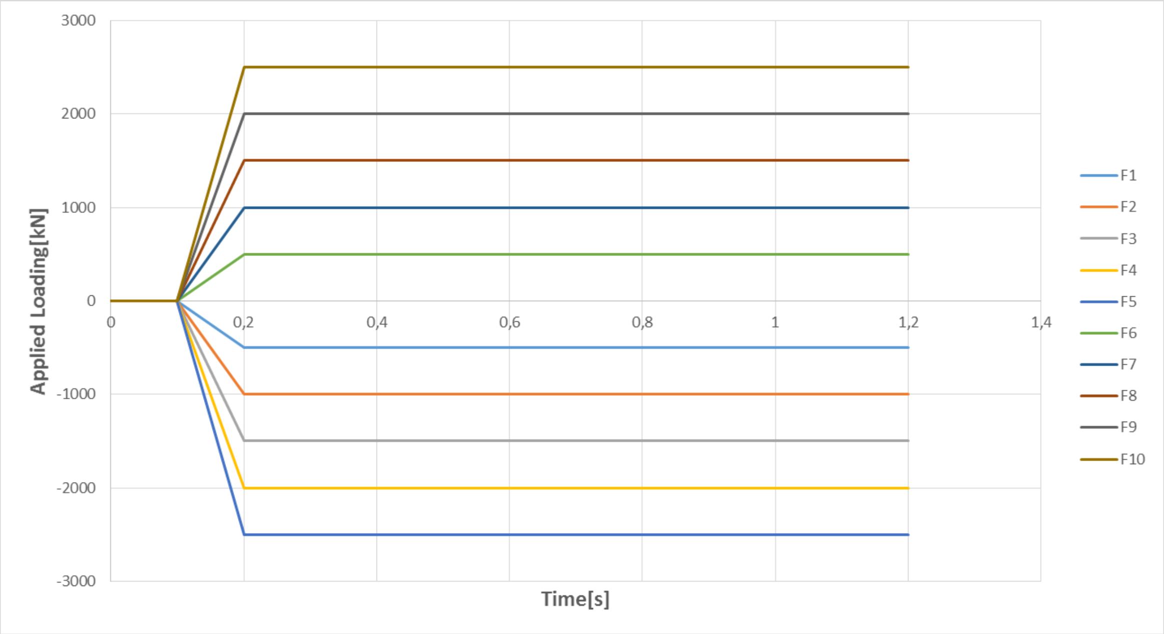

Figure 4.9: The loading time series applied to investigate the effect of horizontal interface force amplitudes and directions under different sea states

The turning moment is also an important parameter to be investigated after studying the effect of different horizontal interface force. Different amplitudes and directions of the turning moment are applied, and it is shown in Figure 4.10. Similar to different horizontal forces study, four different turning moment levels from 1000kNm to 4000kNm are applied to the T point in the global X-direction and Y-direction, and only negative direction is considered since the positive direction and negative direction turning moment lead to similar situation. The turning moment used in the negative X-direction are represented as Mx1, Mx2, Mx3 and Mx4 respectively. Similarly, the turning moment applied on negative Y-direction are represented as My1, My2, My3 and My4.

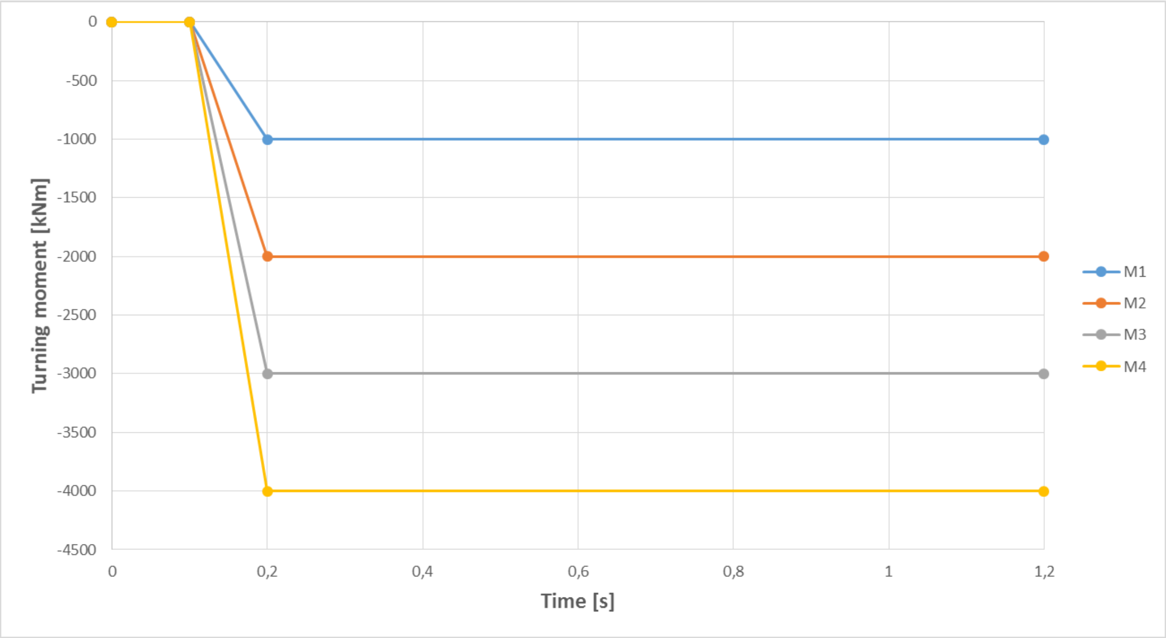

Figure 4.10: The loading time series applied to investigate the effect of turning moment amplitudes and directions under different sea states

3. The different structural configurations of spar cylinder have been designed with different stiffener combinations.

    - Configuration 1 (C1): Spar cylinder without any stiffeners;
    - Configuration 2 (C2): Spar cylinder with three vertical T-bar stiffeners attached along the flat track;
    - Configuration 3 (C3): Spar cylinder with vertical BHD attached along the flat track;
    - Configuration 4 (C4): Spar cylinder with vertical BHD attached along the flat track and horizontal rings under the roller initial positions;
    - Configuration 5 (C5): Spar cylinder with three vertical T-bar stiffeners attached along the flat track, and with horizontal central BHD and horizontal rings under the roller initial positions;
    - Configuration 6 (C6): Spar cylinder with vertical BHD attached along the flat track, and with horizontal central BHD and horizontal rings under the roller initial positions.

    The different structural configurations are shown in Figure 4.11. The thickness of the CYL and stiffeners are also presented.

4. The thickness of the spar cylinder hull plays an important role in resisting the contact stress in the spar. Therefore, different thickness of spar cylinder is studied in order to obtain a proper thickness value. The original thickness of the spar is 0.05m, and then the thickness of the flat track part on the spar is increased to 0.07m and 0.09m respectively.

4.4 Results and discussion

In this chapter, the nonlinear finite element analysis is performed according to the different scenarios presented before. The effects of the different spar configurations, different loading conditions, different spring stiffness, and different flat track thickness are investigated respectively, and the results are demonstrated afterward. The constant loading is applied to the local model and the structural responses of the spar are examined.

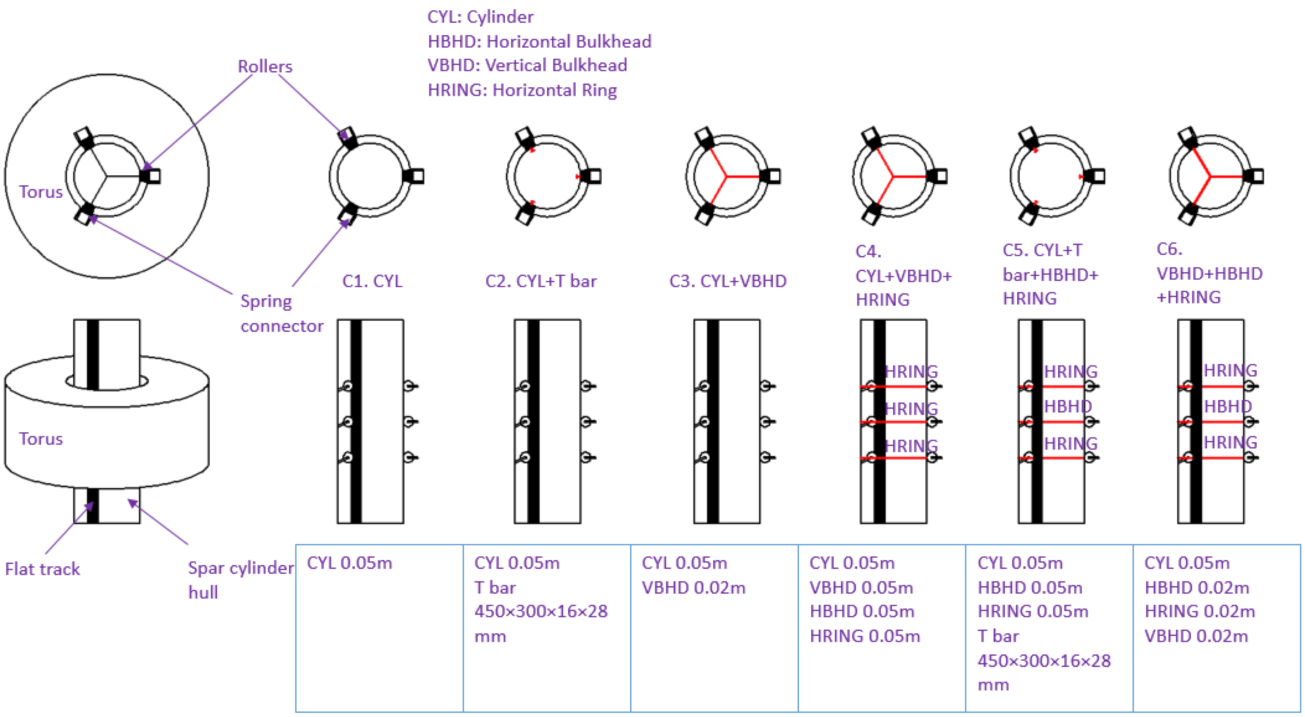

C1. CYL	C2. CYL+T bar	C3. CYL+VBHD	C4. CYL+VBHD+ HRING	C5. CYL+T bar+HBHD+ HRING	C6. VBHD+HBHD +HRING
CYL 0.05m	CYL 0.05m T bar 450×300×16×28 mm	CYL 0.05m VBHD 0.02m	CYL 0.05m VBHD 0.05m HBHD 0.05m HRING 0.05m	CYL 0.05m HBHD 0.05m HRING 0.05m T bar 450×300×16×28 mm	CYL 0.05m HBHD 0.02m HRING 0.02m VBHD 0.02m

Figure 4.11: Different spar cylinder structural configurations with different stiffener combinations

4.4.1 Different spar cylinder structural configurations

In this part, under the situation of Spring1 with stiffness=1000kN/m, F2=-1000kN, and six different structural configurations of spar cylinder are used to investigate the influence of different interface layouts. In other words, the six structural configurations from C1 to C6 are investigated under the same loading condition. The maximum Von Mises stress and the maximum deformation magnitude on the spar contact surface during the whole time series(from 0s to 1.2s) are illustrated in Figure 4.12 and Figure 4.13. Apparently, locations of the maximum Von Mises stress and maximum deformation magnitude on the spar are varying with time, but they are always on the contact surface.

In general, the maximum Von Mises stress and the maximum deformation magnitude rise sharply at the beginning of the contact process, and tend to be stable after the steady contact condition is achieved. It is clear that the spar cylinder without any stiffeners (C1) gives rise to the most significant Von Mises stress and the largest deformation magnitude on the spar contact surface during the simulation process. The configuration C2 attached with three T-bar stiffen-

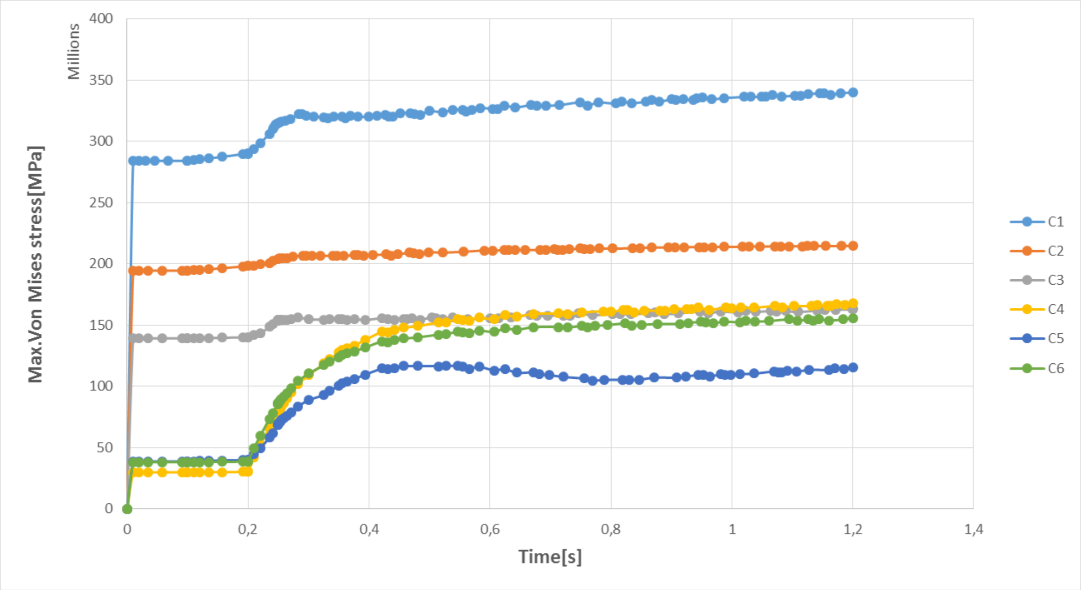

Figure 4.12: Maximum Von Mises stress on the spar contact surface during the entire simulation time series

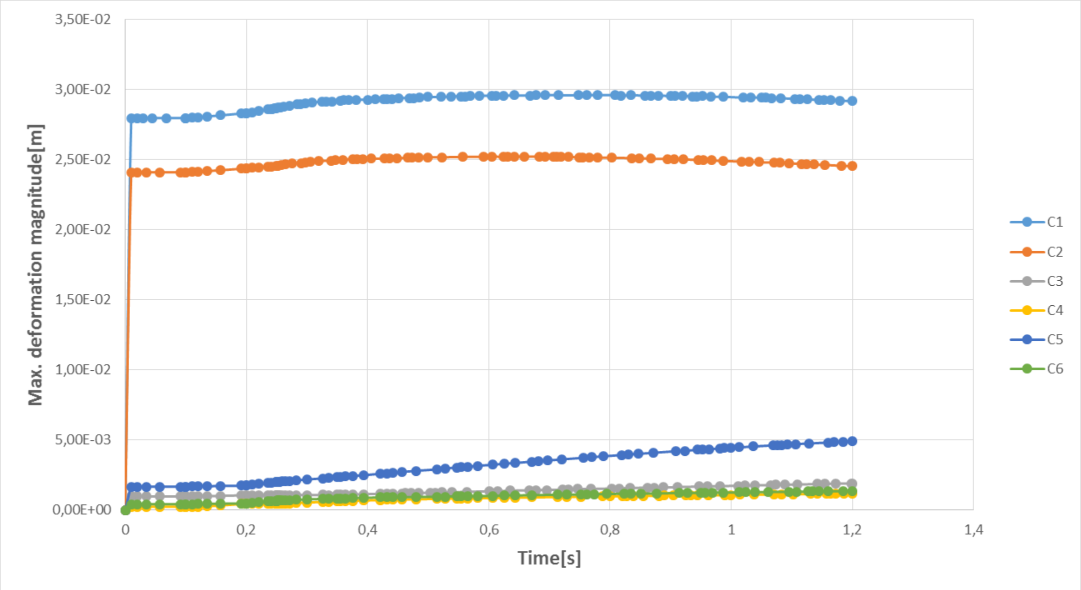

Figure 4.13: Maximum deformation magnitude on the spar contact surface during the entire simulation time series

ers reduces the maximum Von Mises stress significantly, which decreases about 38% compared against C1. However, the deformation magnitude is still relatively large. Then the vertical BHD is attached on the spar cylinder instead of T-bar (C3), the maximum Von Mises stress is reduced further and the maximum deformation magnitude is decreased dramatically compared with C2. Besides, configurations C4, C5 and C6 lead to positive effects to reduce maximum Von Mises stress and maximum deformation magnitude. By comparing C2 to C5, it is noted that the horizontal BHD and rings play a significant role in reducing both Von Mises stress and deformation magnitude on the spar contact surface. Similarly, the comparison between C3 and C6 shows the same conclusion. However, since the vertical BHD in C3 is already strong to resist the contact stress, the extra horizontal stiffeners in C6 only reduces the response with a slight degree. By comparing C4 and C6, the horizontal BHD is stronger than the horizontal ring in reducing Von Mises stress but their performances for reducing deformation magnitude are basically the same. If comparing the C1, C2, C3 with C4, C5, C6,it is also clear that the maximum Von Mises stress shows an obvious decline from 0s to 0.4s. Hence, In other words, the horizontal stiffeners are effective in reducing Von Mises stress at the beginning of the contact process. In addition, C5 gives the smallest "maximum Von Mises stress" while C4 and C6 give the smallest " maximum deformation magnitude". However, some considerable local stress concentrations are observed at the intersection between the T-bar web and horizontal rings in C5, and the value could reach to $1.9E+08$ MPa. Although the concentrated stress is a very local problem, it still should be taken into consideration to select a proper configuration. In Figure 4.14, it can be seen that the T point Y-direction displacement is not influenced significantly by different structural configurations. Therefore, it is not an effective approach by adding stiffeners to reduce the T point displacement.

In conclusion, the additional stiffeners can reduce both maximum Von Mises stress and maximum deformation magnitude on the spar, compared with pure spar cylinder hull (C1). Configurations C3, C4, C5 and C6 give acceptable Von Mises stress and deformation magnitude, but local concentrated stress problem exists in C5. Therefore, C6 might be the optimal choice since C6 gives acceptable Von Mises stress and deformation magnitude values, and the weight of the C6 will be not significant with thinner stiffeners.In addition, structural weight, feasibility, and repairability should be taken into account for real construction.

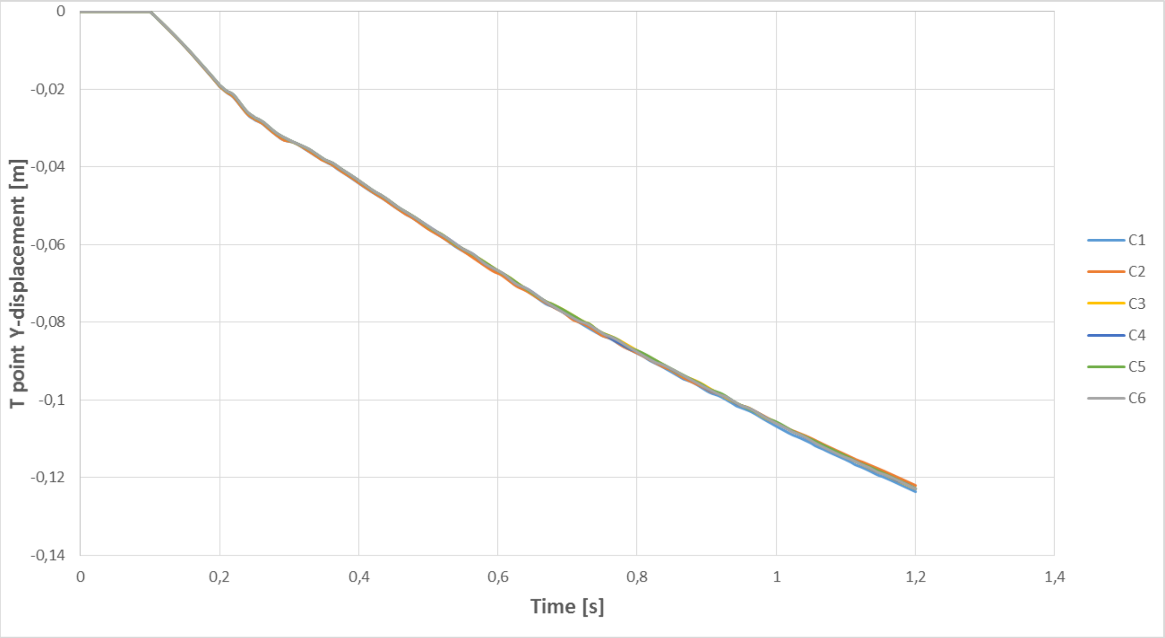

Figure 4.14: T point Y-direction displacement under Spring1 and F2 for different structural configurations

4.4.2 Different loading conditions

According to the scenario demonstrated previously, the different horizontal loading conditions are applied to the T point. The loading conditions from F1 to F10 represent different magnitudes and directions. The horizontal force magnitudes vary linearly from 500kN to 2500kN for F1-F5 in the negative Y-direction; similarly, the magnitudes vary linearly from 500kN to 2500kN for F6-F10 in the positive Y-direction, as shown in Figure 4.9. The effects of different horizontal loading conditions is investigated for C6 and Spring1=1000kN/m.

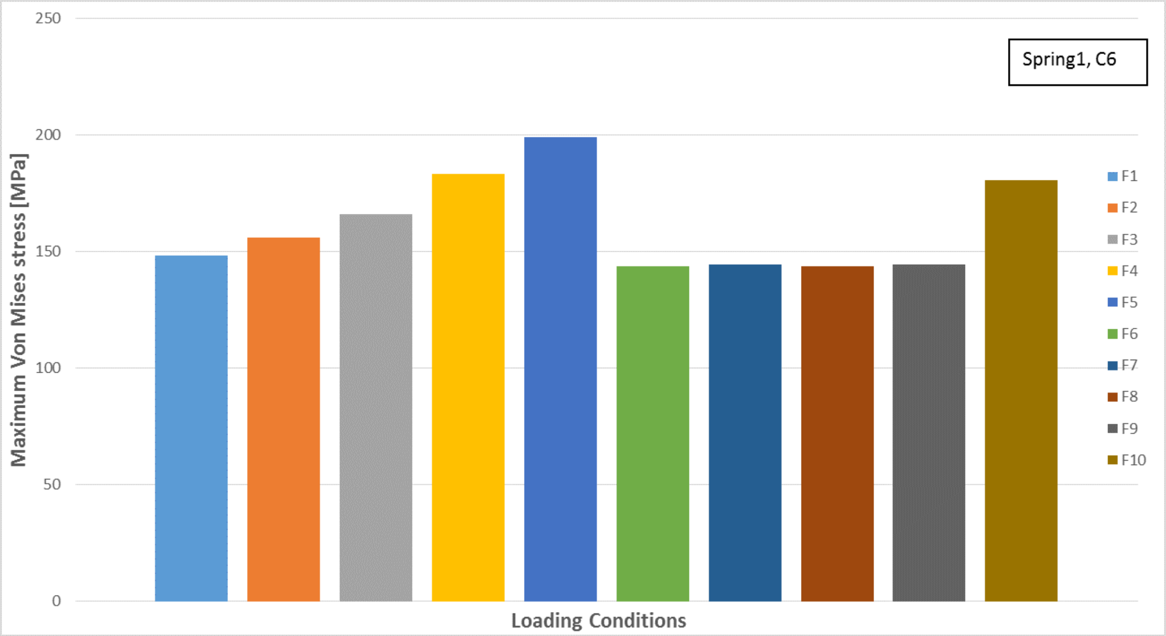

Figure 4.15: Maximum Von Mises stress on the spar cylinder hull at 1.2s under different loading conditions from F1 to F10

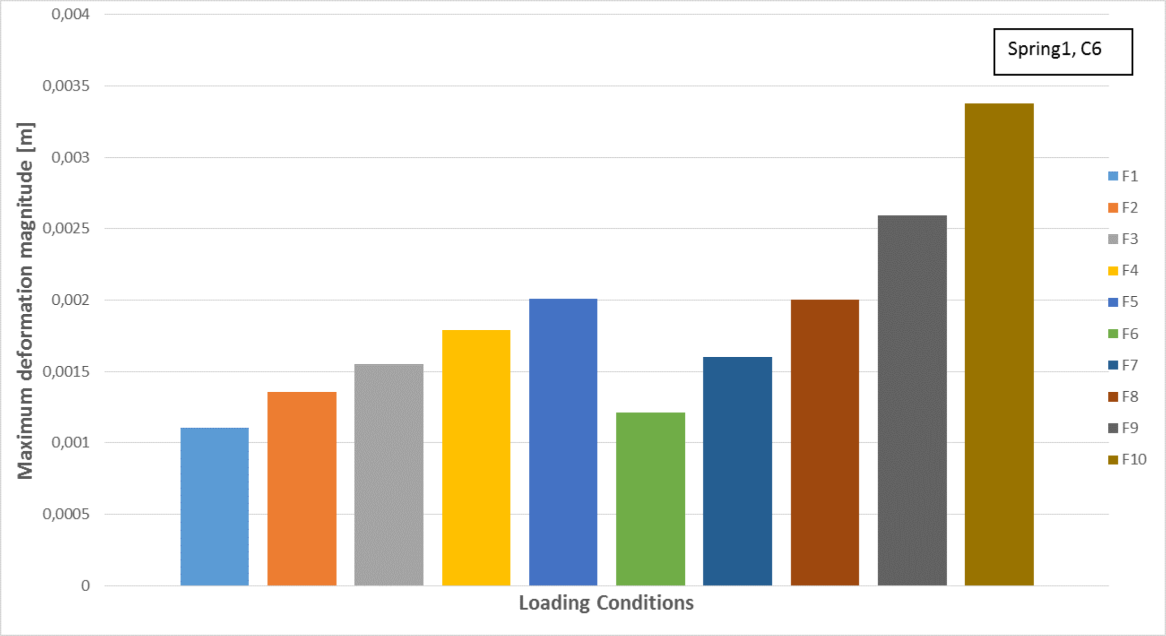

Figure 4.16: Maximum deformation magnitude on the spar cylinder hull at 1.2s under different loading conditions from F1 to F10

In Figure 4.12 and Figure 4.13, it is clear that the stress and deformation magnitude are almost invariable during the stable rolling process; therefore, the maximum Von Mises stress and maximum deformation magnitude on the spar cylinder hull at 1.2s under different horizontal loading conditions are shown in Figure 4.15 and Figure 4.16. It is clear that under negative Y direction loading (F1-F5), both Von Mises stress and deformation magnitude almost linearly increase, while under positive Y direction loading (F6-F10), the increments of maximum Von Mises stress and maximum deformation magnitude are dramatically nonlinear.

The Figure 4.17 shows the stress distribution on the spar cylinder hull at 1.2s for loading conditions F1-F5. It can be seen that under the negative loading, the maximum Von Mises stress always appears on the flat track 1 surface corresponding to where roller1 is located at 1.2s. For flat track 1, the stress distribution is symmetrical and the critical point is always located at the central line of the flat track 1. What's more, in Figure 4.18, the stress distribution on the roller3 is demonstrated for loading conditions F1-F5. The shapes of the stress critical area are similar, and the location of the critical point has no change with the increasing loading; only the stress magnitude on the roller3 increases with the rising loading. The result is attributed to the fact that for negative loading F1-F5, roller1 to roller3 are compressed more than other rollers; therefore, the rollers from 1 to 3 undertake the main loading, and the force direction is perpendicular to the flat track 1 surface on which roller1, roller2 and roller3 are located. The rolling condition is relatively stable, and both of the stress distribution and deformation magnitude distribution are similar with increasing loading from F1 to F5.

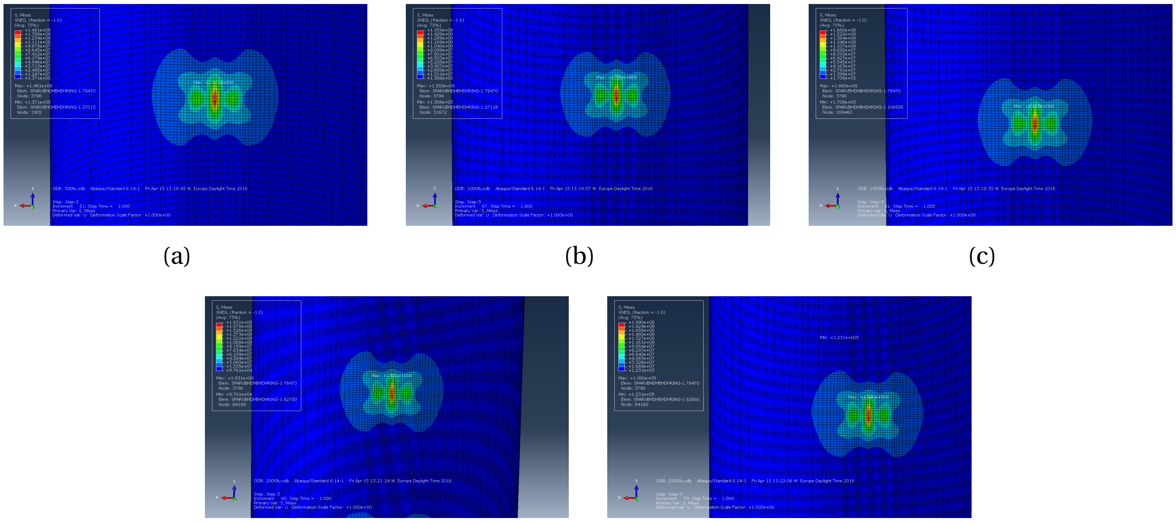

(a) (b) (c)

(d) (e)

Figure 4.17: The maximum Von Mises stress distribution on the flat track 1 outer surface at 1.2s for Spring1 and C6 under different loading conditions (a) F1(b) F2 (c) F3 (d) F4 (e) F5

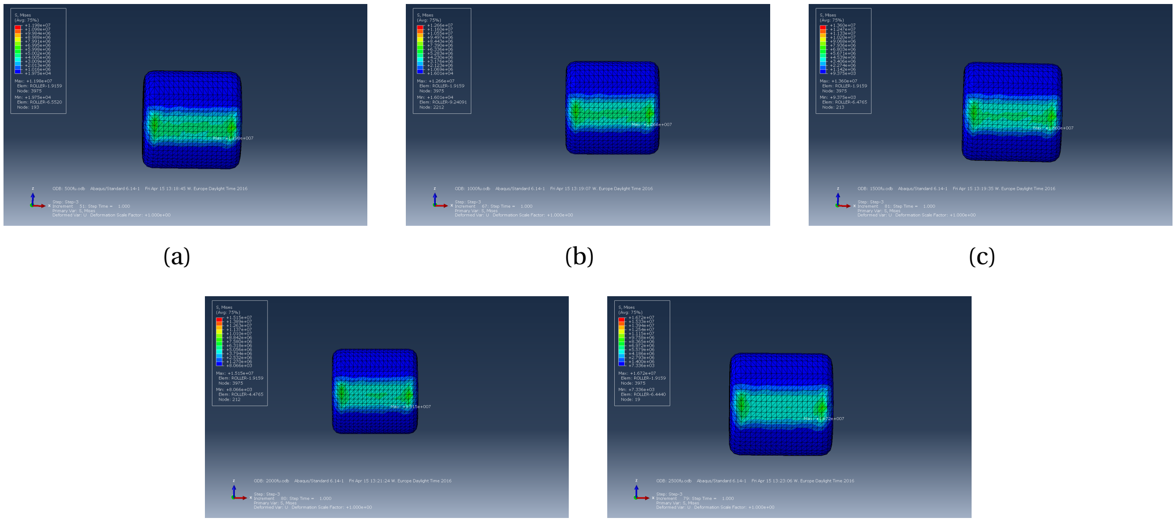

(a) (b) (c)

(d) (e)

Figure 4.18: The maximum Von Mises distribution on the roller3 at 1.2s for Spring1 and C6 under different loading conditions (a) F1(b) F2 (c) F3 (d) F4 (e) F5

Interestingly, for positive loading F6-F10, the increments of maximum Von Mises stress and maximum deformation magnitude on the spar hull are extremely nonlinear. This is probably because that, for F6-F10, the rollers of 4 to 9 instead of the rollers of 1 to 3 carry the main loadings, but the loading direction is not perpendicular to flat track 2 and flat track 3. Therefore, the contact forces for the roller1 to roller3 are relieved, while the rolling conditions of other rollers become significant. Consequently, there are two force components on the roller4 to roller9, one of the force components compresses the roller on the flat track and the other one gives rise to the lateral deviation between the roller and the flat track. In other words, the contact area will deviate from the original region and the contact area will be smaller because of the lateral deviation. It is clearly shown in Figure 4.20 that the contact area is reducing with the increasing loading level. For F10, the contact area is only about 70% of that for loading condition F6. The location of the maximum Von Mises stress is on roller9 for F6 and F7, but for F8 to F10, the location is on roller4. What's more, the location of the stress critical point is not invariable any more. For F6 and F7, the maximum Von Mises stress appears on the flat track 2 surface corresponding to where roller4 is located at 1.2s, while for F8 to F10, the maximum Von Mises stress appears on the flat track 3 surface corresponding to where roller7 is located at 1.2s. In Figure 4.19, it can also be seen that the stress distribution is not symmetrical anymore. The stress critical point is not on the central line of the flat track for F7 to F10; that is to say, the maximum Von Mises stress point deviates from the central and begins to deviate to one side. Apparently, for F7 to F10, there are two stress critical areas in the stress distribution. It means that there are mainly two areas carrying the loading instead of only one concentrated area on the central line of the flat track. The reason probably is that in Figure 4.15, the maximum Von Mises stresses on the spar from F6 to F10 do not increase as are expected. The extreme nonlinear increments of stress and deformation for positive direction loading conditions might be due to the multi-region loading support and the lateral deviation of rollers. These two concentrated stress areas can distract the large loading so that the maximum Von Mises stress on the spar can be reduced, and the stiffeners can provide adequate strength, although the rollers deviate from the original region. The maximum stress is much lower than steel yielding stress under all loading conditions; therefore, the design is feasible. However, it is necessary to optimize the interface part based on the structural weight and more severe loading conditions. Apparently, the loading conditions under real sea state are not constant, and in contrast,become more irregular. They could lead to notable responses of the interface between the spar and the torus.

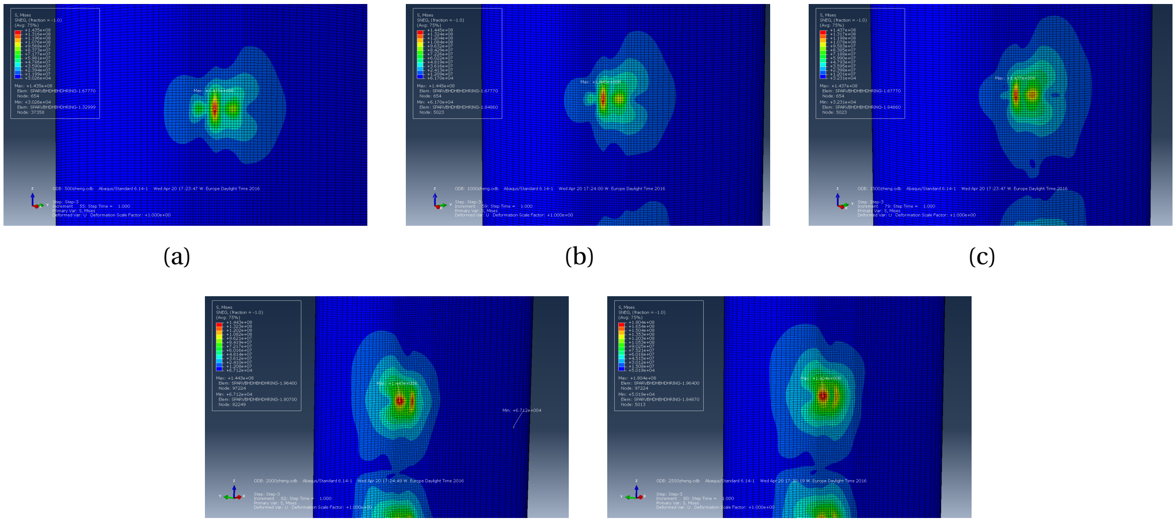
(a) (b) (c)

(d) (e)

Figure 4.19: The maximum Von Mises stress distribution on the flat track 2 outer surface at 1.2s for Spring1 and C6 under different loading conditions (a) F6(b) F7 (c) F8 (d) F9 (e) F10

In Figure 4.21(a), the T point Y-direction displacements are plotted for different loading conditions from F1 to F10. It is clear that the T point Y-direction displacements are increasing with

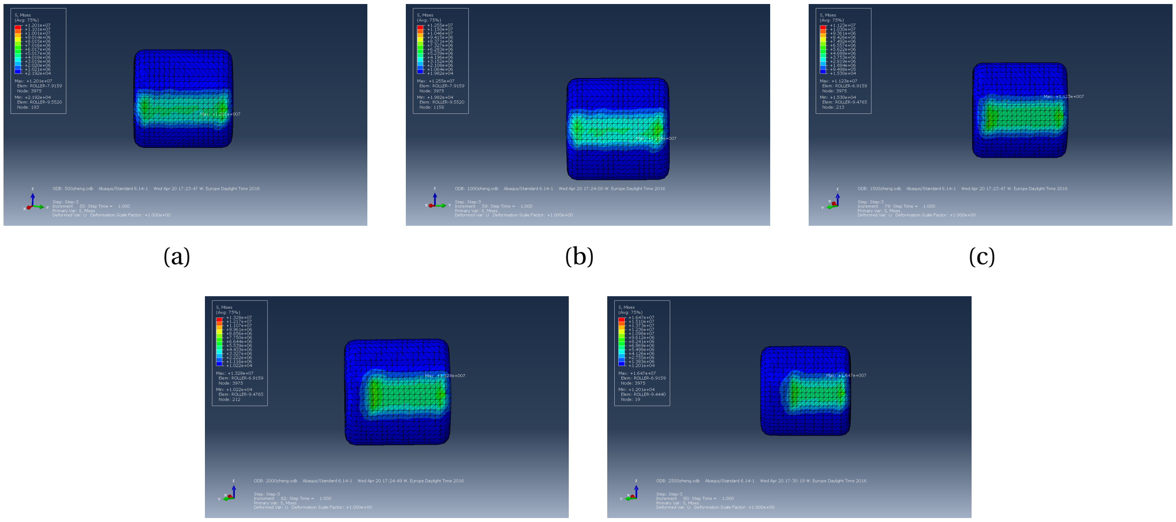

(a) (b) (c)

(d) (e)

Figure 4.20: The maximum Von Mises stress distribution on the roller4 at 1.2s for Spring1 and C6 under different loading conditions (a) F6(b) F7 (c) F8 (d) F9 (e) F10

the larger loading condition. What's more, in Figure 4.21(b), it is worth noting that the T point motions in Y-direction reveal nonlinear trend with the magnitude of the linear increasing loading. The investigation of different loading conditions illustrates that the responses of the local interface part are nonlinear under the varying loading conditions.

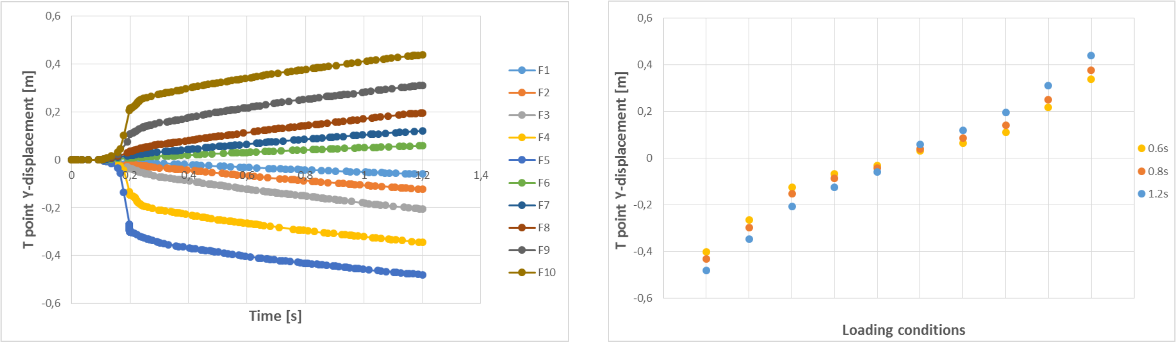

(a) (b)

Figure 4.21: The T point Y-direction displacement under different loading conditions during 1.2s rolling process in (a) and at 0.6s, 0.8s and 1.2s in (b)

Regarding the investigation of different turning moment conditions, the different turning moment conditions from Mx1 to Mx4 and from My1 to My4 are applied to the T point. The amplitudes of the turning moment are shown in Figure 4.10, and the effects of different turning moment conditions are still investigated for C6 and Spring1=1000kN/m.

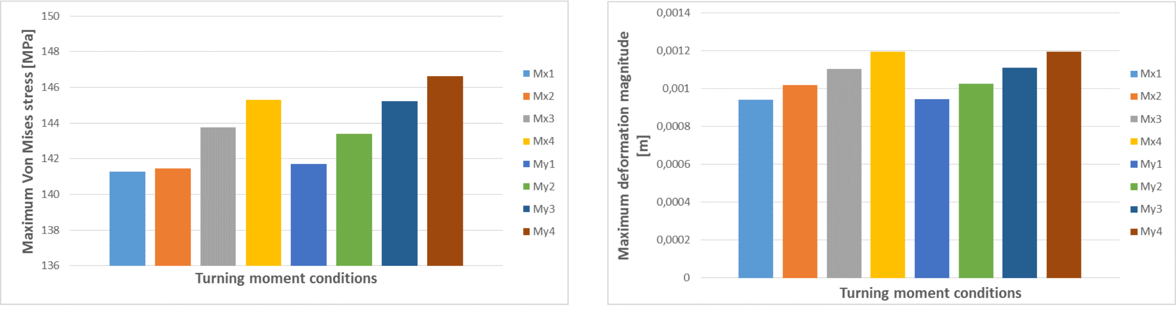

(a) (b)

Figure 4.22: (a) Maximum Von Mises stress and (b) Maximum deformation magnitude on the spar cylinder at 1.2s under different turning moment conditions from Mx1 to My4.

The maximum Von Mises stress and maximum deformation magnitude on the spar cylinder hull at 1.2s under different turning moment conditions are shown in Figure 4.22. It can be seen that for Mx1 to Mx4, the stress increments are more nonlinear than that for My1 to My4, while the deformation increments show the similar trend for Mx1 to Mx4 and My1 to My4. Thus it is necessary to investigate the detailed stress distribution at 1.2s to reveal where the nonlinear trend comes from for Mx1 to Mx4.Therefore, the Von Mises stress distributions for flat track 1 and flat track 2 under different turning moment conditions are presented in Figure 4.23. It is clear that the maximum Von Mises stress occurs on roller4 under Mx1 and Mx2 while the location of maximum Von Mises stress transfers to roller3 under Mx3 and Mx4. Besides, although the stress distribution is still bilateral symmetry for critical stress area on flat track 1, the critical stress areas, which correspond to where roller1 and roller3 are located at 1.2s, are no longer similar due to the turning moment Mx. It is because that the turning moment Mx compresses the roller3 and at the same time tensions the roller1. The local stress condition between the rollers and flat track 1 is different from the condition discussed in the previous studies, which applied constant concentrated loading condition. Similarly, it is also shown in Figure 4.23 that the stress distribution on flat track 2 has also changed due to the applied turning moment. The deviation direction of the rollers on flat track 2 is no longer coincident; the roller4 and roller6 have different deviation directions and the roller in the middle has no notable deviation anymore.

For turning moment My1 to My4, there is no remarkable nonlinear trend for both stress increments and deformation increments. But it is worth to note that the locations of the maximum Von Mises stress and maximum deformation magnitude are always located at the flat track

2 surface corresponding to where roller4 is located at 1.2s. The biggest difference between the cases under turning moment (from My1 to My4) and the previous cases is that the deviation of the rollers is observed on flat track 1.

The turning moment has an insignificant impact on T point displacement and deviation of the rollers at the middle level(i.e. roller2, roller5 and roller8). In other words, the turning moment plays an important role in deciding the local contact condition of the rollers at the upper level(i.e. roller1, roller4 and roller7) and the lower level(i.e. roller3, roller6 and roller9). Therefore, the worse deviation condition of the rollers is observed in this section, the stiffeners under the flat tracks are necessary to support the spar cylinder hull when the rollers move to one side from the central line of the flat tracks.

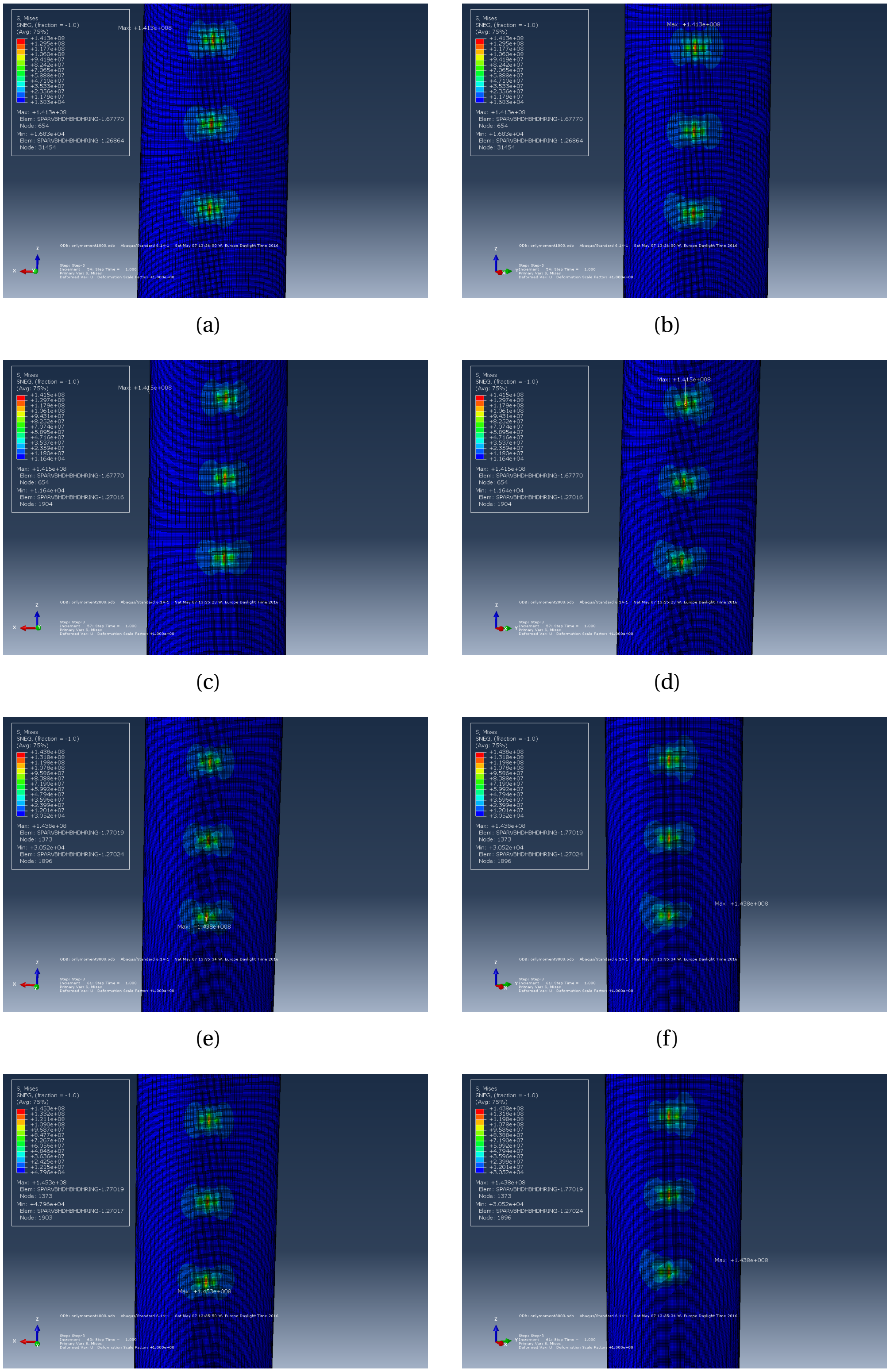

(a) (b) (c) (d) (e) (f) (g) (h)

Figure 4.23: The Von Mises stress distribution for (a)flat track 1 under Mx1 (b)flat track 2 under Mx1 (c)flat track 1 under Mx2 (d)flat track 2 under Mx2 (e)flat track 1 under Mx3 (f)flat track 2 under Mx3 (g)flat track 1 under Mx4 (h)flat track 2 under Mx4.

4.4.3 Different spring connector stiffness

The effect of different connector stiffness is investigated for structural configuration C1 and C6 respectively, since generally, C1 and C6 are two typical structures without any stiffener and with proper stiffeners respectively. The loading condition is still F2=-1000kN in the global Y-direction. The T point Y-direction displacement, the axial force in connector 2, and relative displacement in connector 2 for C1 and C6 are shown in Figure 4.24 and Figure 4.25.

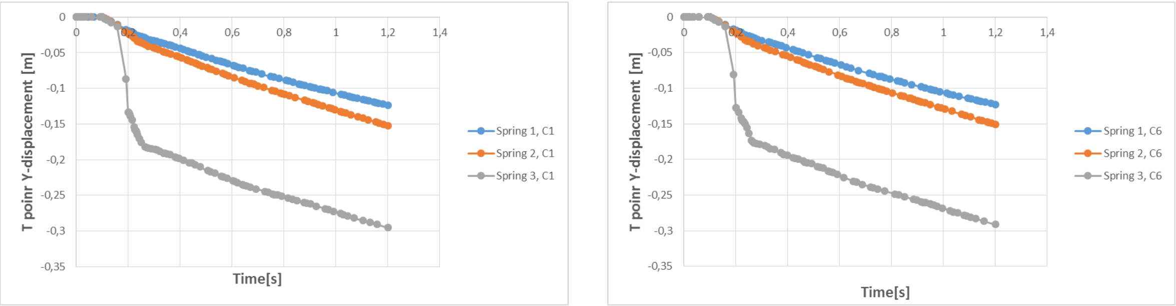

(a) (b)

Figure 4.24: T point Y direction displacement under different spring connector stiffness for structural (a) C1 and (b) C6 under loading condition F2

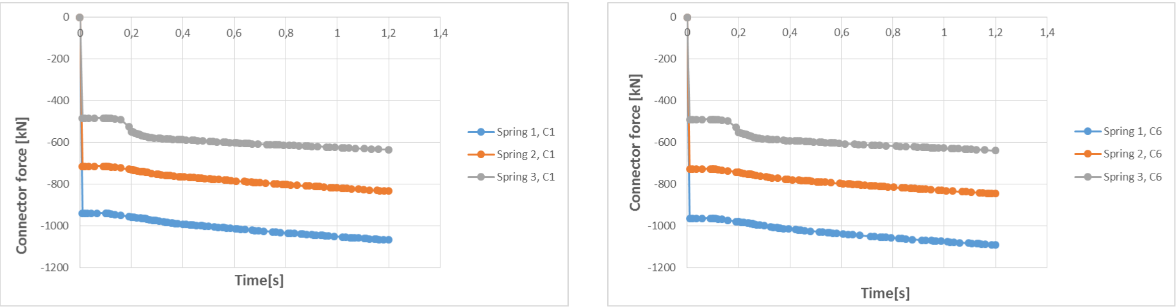

(a) (b)

Figure 4.25: Axial force for connector 2 under different spring connector stiffness for structural (a) C1 and (b) C6 under loading condition F2

It is clear that in both Figure 4.24 and Figure 4.25, the T point Y-displacement and axial force for connector 2 have a similar trend for configuration C1 and C6. For both C1 and C6, the different connector stiffness has a significant influence on the T point motion, and it is necessary to point out that higher connector stiffness leads to lower T point Y-direction motion. The T point Y-direction motion can be reduced from 0.29m to 0.12m by increasing the stiffness from

500kN/m to 1000kN/m. Therefore, the T point motion can be significantly reduced by increasing connector stiffness. Referring to Figure 4.8, the working range of the spring connector is from -0.775m to 0.775m with the initial length of 1m, and even the largest T point Y-displacement is -0.29m which is located within the working range. Moreover, it is important to reduce the T point motion because the rollers from 4 to 9 would deviate from the original location and slide to one side due to large T point motion. The contact area between the spar and the roller will be changed, which might lead to critical local stress and deformation magnitude. Therefore, smaller T point displacement is pursued in the design process. From Figure 4.25(a) and 4.25(b), it can be seen that the axial connector force increases dramatically from 0s to 0.1s due to the pre-compression, and from 0.1s to 0.2s the connector force is increased again because of the application of the loading on T point. Then the connector force rises steadily during the rolling process because the constant loading is applied to the T point from 0.2s to the end of the simulation.

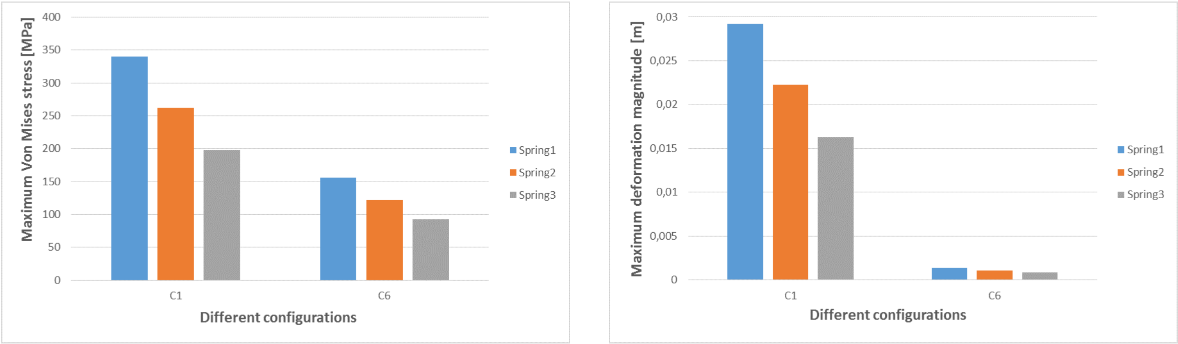

(a) (b)

Figure 4.26: (a) Maximum Von Mises stress on the spar contact surface at 1.2s under different spring stiffness for C1 and C6. (b) Maximum deformation magnitude on the spar contact surface at 1.2s under different spring stiffness for C1 and C6.

In Figure 4.26, it can be seen that larger spring stiffness introduces larger stress and deformation magnitude on the spar contact surface for both C1 and C6. However, it is previously shown in Figure 4.24 that larger spring stiffness can reduce T point Y-direction displacement significantly. Hence, compromise should be achieved among the stress level, deformation magnitude and T point motions to decide the proper spring connector stiffness.

4.4.4 Different thickness

The contact problem is quite local between the rollers and flat tracks; therefore increasing the thickness of the flat tracks is expected to reduce the stress and deformation on the spar. Consequently, the thickness of the flat track is increased from 5cm to 7cm and 9cm, as shown in Figure 4.27, the yellow parts are the flat track with increased thickness. The effect of different thickness of the flat track is investigated under the loading condition F2=-1000kN for the configuration C6.

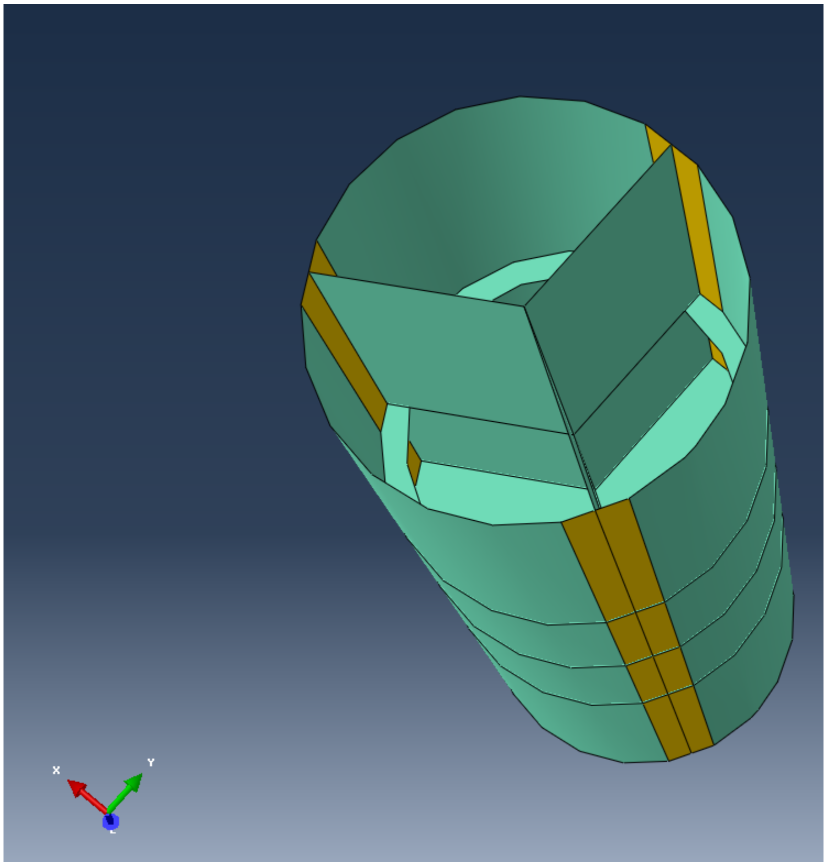

Figure 4.27: The increased thickness on the flat track for configuration C6

The Maximum Von Mises stress and maximum deformation magnitude at 1.2s on the spar cylinder under different thickness of the flat track are shown in Figure 4.28. It is clear that the stress and deformation are significantly reduced by increasing the thickness of the flat tracks. However, the first thickness increment is much more effective to reduce the stress and deformation than the second thickness increment. Therefore, it is important to choose a proper thickness of the flat track. Besides, the feasibility of weld technique should be taken into con-

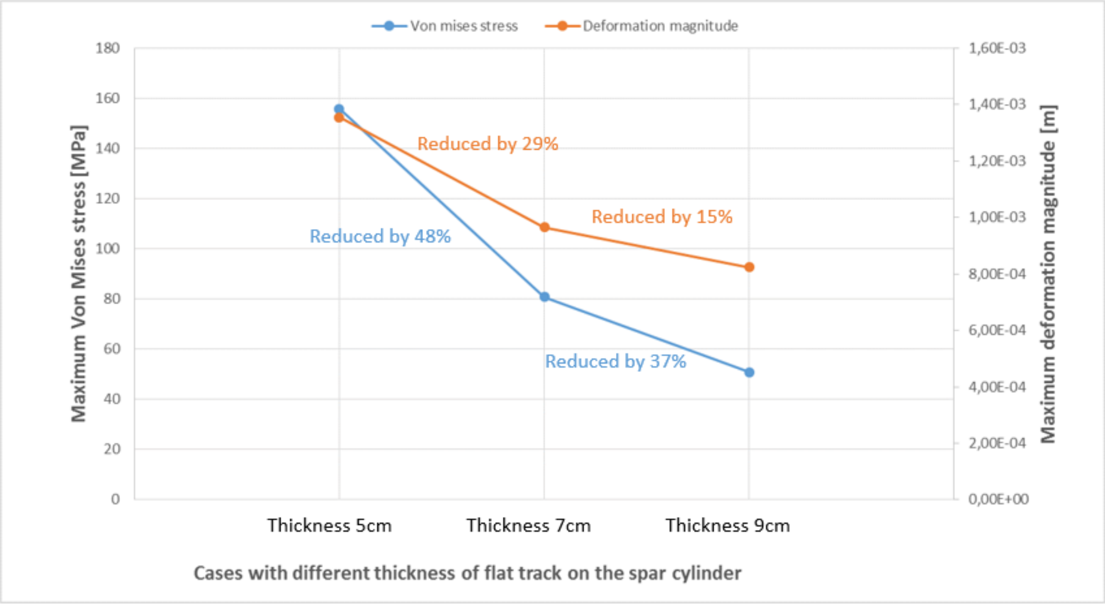

Figure 4.28: The maximum Von Mises stress and maximum deformation magnitude results comparison between the different thickness of the flat track on the spar cylinder

sideration if the thickness of the flat track is different from the spar cylinder hull. What's more, in Figure 4.29, the T point Y-direction displacement is not reduced with increasing thickness of flat tracks. Referring to the Figure 4.14, it can be concluded that both different structural configurations and different thickness of flat tracks have a negligible influence on changing T point displacement.

4.5 Summary

In this chapter, an elementary interface design is performed and a primary quasi-static nonlinear finite element analysis is achieved according to different scenarios. The local model of spar-torus interface part is established in ABAQUS under proper boundary conditions, and then the effects of different structural configurations of the spar cylinder, different constant loading conditions, different spring connector stiffness and different flat track thickness are investigated respectively. According to the results obtained in stress analysis, several conclusions can be drawn as follows:

1. For different structural configurations of the spar cylinder hull, both of the horizontal stiffeners and the VBHD located along the rolling direction are significantly effective in reduc-

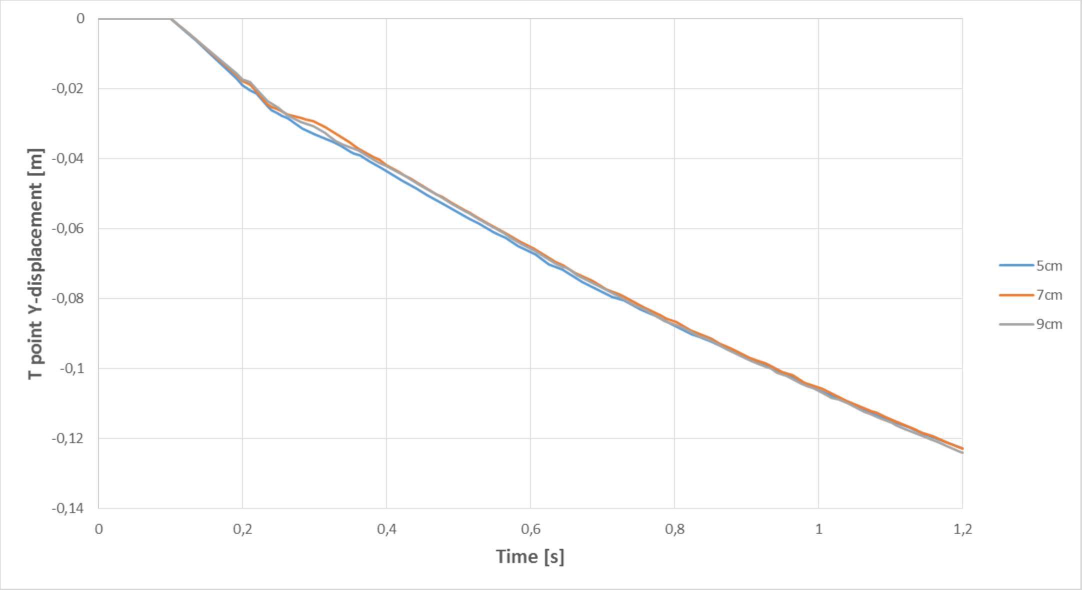

Figure 4.29: T point Y-direction displacement under Spring1 and F2 for different thickness of flat track

ing the maximum Von Mises stress and the maximum deformation magnitude on the spar.

2. For different horizontal interface force (F1 to F10), the increments of maximum Von Mises stress and maximum deformation magnitude on the spar cylinder are very nonlinear, especially for positive Y-direction loading (F6-F10). The rollers, which are located at flat track 2 and flat track 3, deviate from the original location to one side laterally; consequently, the contact areas between the rollers and the spar are reduced due to the deviation. Regarding the turning moment, the phenomenon of nonlinear stress and deformation increments is not evident anymore, but it is clear that the turning moment has a negligible effect on T point displacement.

3. For different spring connector stiffness, the smaller stiffness leads to larger T point motion, while the smaller stiffness gives rise to smaller connector force. Therefore, this indicates that it is effective to reduce the T point motion by increasing the connector stiffness. What's more, the larger stiffness also introduces larger stress and deformation magnitude on the spar contact surface. For this reason, the design should be compromised among the stress level, deformation magnitude, and T point motion.

4. For different flat track thickness, larger flat track thickness is effective in reducing the

stress and deformation magnitude on the contact surface of the spar cylinder hull. However, an appropriate thickness should be picked in order to ensure that the weight of the structure is not incredibly huge.

Chapter 5

Further Quasi-static and dynamic Nonlinear Analysis

In previous sections, the elementary interface design is performed and an elementary nonlinear stress analysis is achieved in ABAQUS. Consequently, some conclusions are achieved for the guide-roller interface structural design. However, further nonlinear analysis is required to investigate the effects under real sea state and the oscillation effect in horizontal direction.

5.1 Nonlinear quasi-static analysis under real sea state without slamming effect

In previous sections, the modelling and the response of the interface part under different scenarios have been studied. However, the constant B.C. conditions and loading conditions are applied in previous study, it is necessary to investigate the performance of the interface model by applying irregular loading and boundary condition corresponding to specified real sea state. According to the previous model test, the sea state of Hs=2m, Tp=13s is selected, and the most critical 20s are picked from the real sea state time series. The configurations C6 with Spring1=1000kN/m are investigated in this chapter.

The input information for sea state Hs=2s, Tp=13 is shown in Figure 5.1. The relative heave motion, horizontal interface force Fy and the turning moment Mx are applied at the T point

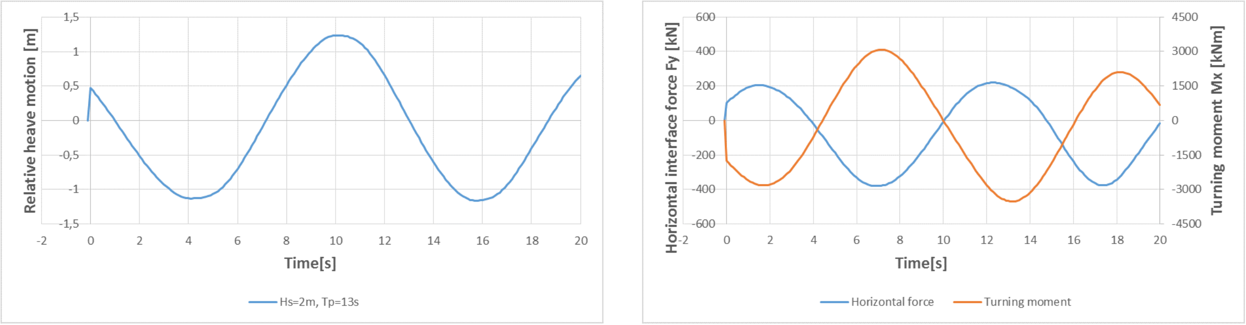

(a) (b)

Figure 5.1: The relative heave motion (a), horizontal interface force Fy and the turning moment Mx (b) corresponding to the sea state Hs=2m, Tp=13s applied to the T point for the 20s simulation time series.

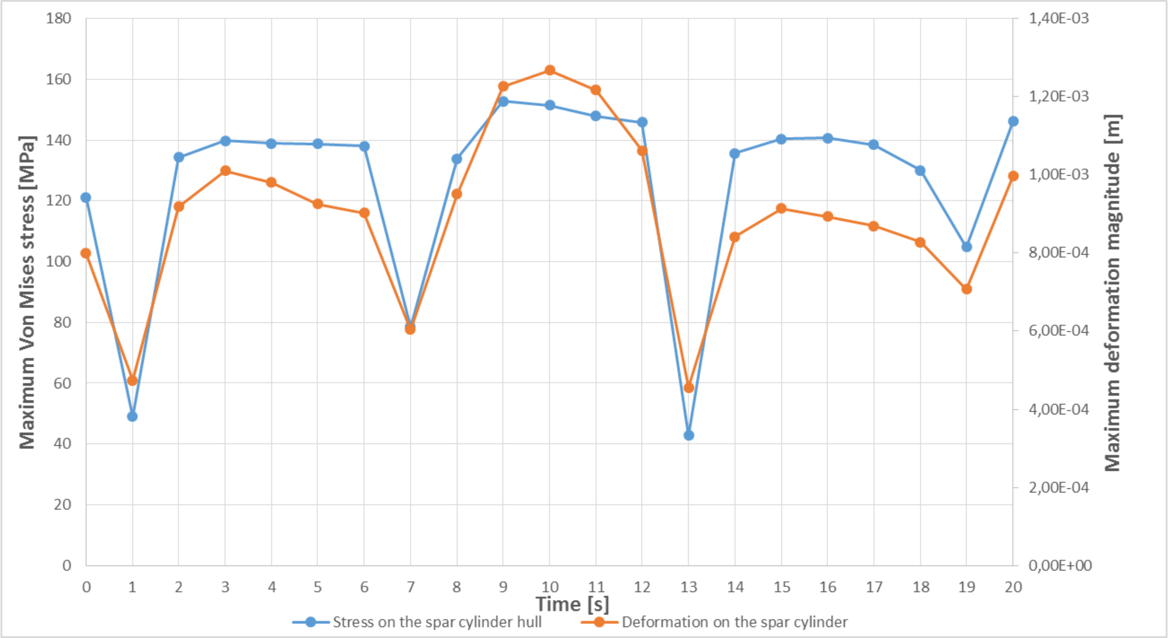

Figure 5.2: The maximum Von Mises stress and maximum deformation magnitude on the spar cylinder hull for 20s

for 20s. Similar to previous simulation, another 0.2s simulation is applied before the 20s real analysis to establish the stable boundary and loading conditions.

According to the inputs, the quasi-static nonlinear analysis for sea state Hs=2m, Tp=13s is performed in ABAQUS, and the maximum Von Mises stress and maximum deformation magnitude for the spar cylinder hull are presented in Figure 5.2, it is clear that the curve of stress and deformation have similar trend but the maximum value location is changing on the spar surface during the 20s. What's more, it can be seen that the trend of stress and deformation on the spar is roughly following the trend of the relative heave motion in Figure 5.1(a). The crest and though of the relative heave motion curve are located at about 4s, 10s and 16s, analogously, at the same timing in Figure 5.2, the stress and deformation on the spar cylinder tend to be larger than any other timing. Refer to the Figure 5.3(a), the value of the stress on the rollers fluctuates under a stable stress level, which is much lower than that on the spar cylinder hull.

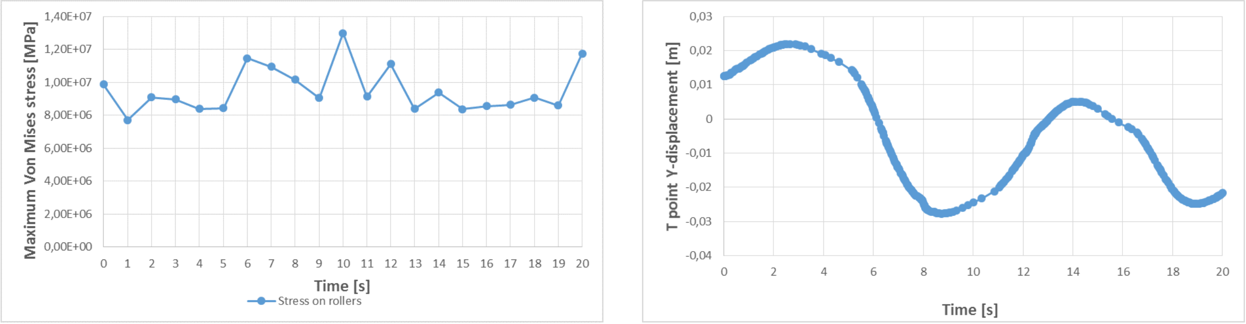

(a) (b)

Figure 5.3: (a) The maximum Von Mises stress on the rollers for the 20s. (b) The T point Y-displacement for the 20s.

Regarding the Figure 5.3(b), the curve of T point Y-displacement has the similar trend as the curve of horizontal interface force Fy in Figure 5.1(b). Actually, the fact that the T point displacement is strongly effected by horizontal interface force have been observed in previous study already. Furthermore, the turning moment has negligible influence on the T point motion as expected.

5.2 Investigation of horizontal oscillation frequency

In this section, the interface model is simplified and only the horizontal response is focused. Consequently, the horizontal motion of the T point can be simplified as a spring-mass system with one degree of freedom. Basically, the interface model in ABAQUS is used to calculate the stiffness of the spring-mass system. Then the horizontal oscillation natural frequency corresponding to the simplified system is investigated and the vertical motion of the rollers is suppressed. Besides, other boundary conditions are identical to previous local interface model. The loading conditions is assumed as shown in Figure 5.4(a), the horizontal force magnitudes vary linearly from 500kN to 2500kN for F1-F5 in the negative Y direction are applied at T point in 1.2s. It is quiet similar to the previous investigation of different loading conditions but the vertical rolling is neglectful for present study.

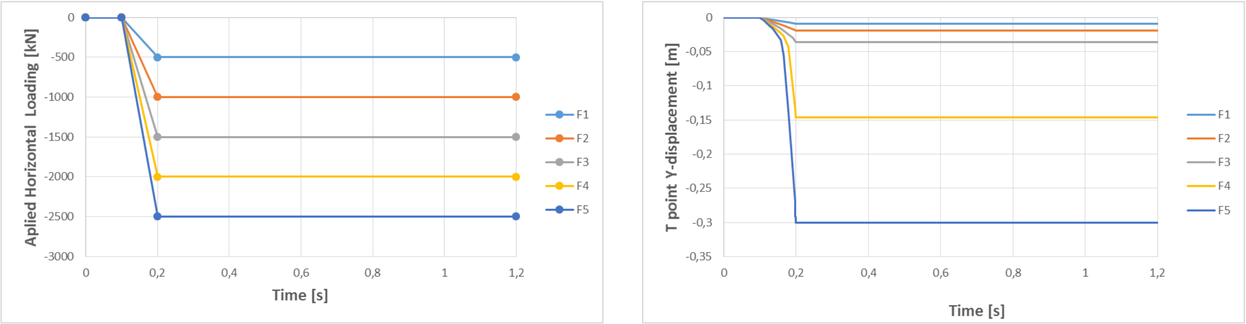

(a) (b)

Figure 5.4: (a)The loading time series applied to investigate the horizontal oscillation frequency. (b) The T point Y-direction displacement under corresponding applied loading conditions.

In Figure 5.4(b), the T point Y-direction displacement corresponding to different loading conditions (F1-F5) are plotted, and then the Force-displacement curve can be achieved. It is shown in Figure 5.5, five points are captured and the slope of the curve is obtained by using linear regression method. The stiffness of the system is obtained because it is the same as the slope of the F-X curve and the mass of the torus is $1.145 \times 10^6 kg$ from previous papers. Consequently, after the quasi-static analysis, the equations for dynamic system with one degree of freedom can be used to calculate the natural frequency of the horizontal oscillation of the interface part. The natural frequency of the horizontal oscillation for the interface part system and the horizontal force frequency corresponding to sea state Hs=2m, Tp=13s are calculated in Equation 5.1 and

5.2.

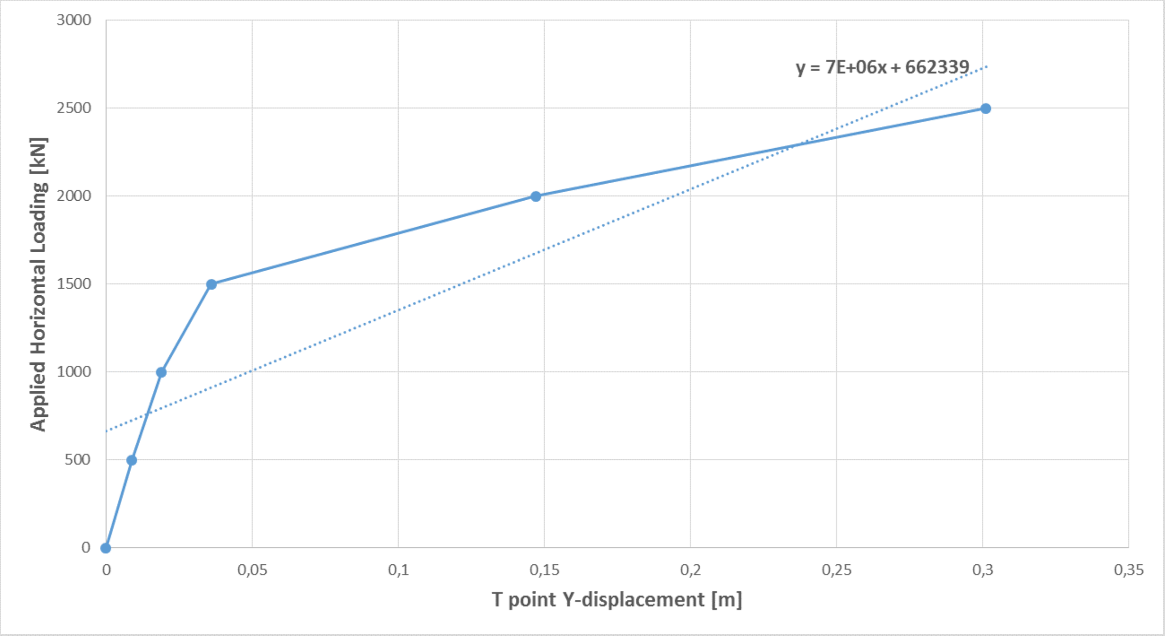

Figure 5.5: Force-displacement curve for horizontal oscillation

$$Natural \quad frequency \qquad w_0 = \sqrt{\frac{k}{m}} = \sqrt{\frac{7E+06}{1.145\times10^6}} = 2.47(rads^{-1}) \tag{5.1}$$

$$Horizontal \quad force \quad frequency \qquad w = \frac{2\pi}{T} = \frac{2\pi}{13} = 0.48(rads^{-1}) \tag{5.2}$$

The natural frequency of the horizontal oscillation is much larger than the frequency of horizontal interface force , therefore, the horizontal resonance will not be activated under horizontal interface loading corresponding to sea state Hs=2m, Tp=13s or Hs=6m, Tp=13s.

However, In Figure 5.6, it is interesting to note that the slope of the F-X curve is larger for lower horizontal loading (F1-F3), while the slope of the F-X curve is smaller for larger horizontal loading (F3-F5). In other words, the stiffness of the horizontal system is larger for lower loading range. Consequently, the natural frequency of the horizontal oscillation is larger for lower loading range, and this can be seen in Equation 5.3 and Equation 5.4. This implies that the horizontal spring-mass system without damping is more rigid under lower loading conditions, and as the increasing horizontal interface loading, the interface system begins to become more

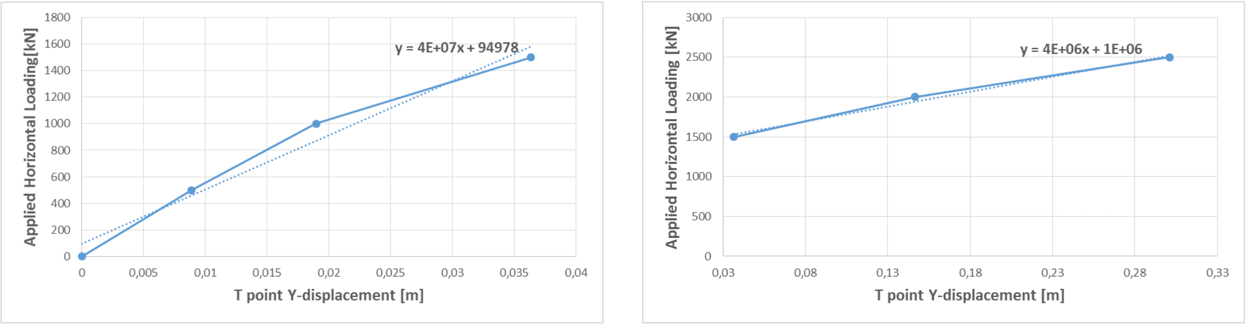

(a) (b)

Figure 5.6: (a) Force-displacement curve for horizontal oscillation corresponding to lower loading (F1-F3). (b) Force-displacement curve for horizontal oscillation corresponding to larger loading (F3-F5).

flexible. Therefore, the interface design strongly depends on the real sea state.

$$Natural\ frequency\ for\ lower\ loading\ w_0 = \sqrt{\frac{k}{m}} = \sqrt{\frac{4E+07}{1.145\times10^6}} = 5.91(rads^{-1}) \tag{5.3}$$

$$Natural\ frequency\ for\ higher\ loading\ w_0 = \sqrt{\frac{k}{m}} = \sqrt{\frac{4E+06}{1.145\times10^6}} = 1.87(rads^{-1}) \tag{5.4}$$

5.3 Elementary investigation of the rollers' mass effect

In this part, the mass of the rollers are considered, and the dynamic effect of the roller's mass are investigated consequently. The vertical motion and the T point displacement are neglected, and only the release process of the spring connector is the focus. In other words, the investigation mainly studies the rollers' mass effect during the spring connector release process.

In Figure 5.7,It can be seen that , the spring connector is released from the 0.1s to 1.2s, the local oscillation of the connector occurs immediately and the oscillation decays during the 1.2s since no extra loading is added to this system. The frequency of the local connector horizontal oscillation is very large, and the rollers' mass makes a big difference on connector force. In quasi-static analysis, the oscillation of the spring connector is not excited because of the mass is not considered at all. Therefore, it is reasonable to assume that the oscillation of the T point is also expected to happen if the mass of the T point is taken into account in dynamic analysis. The oscillation frequency of the interface structure, which includes the mass effect, is important.

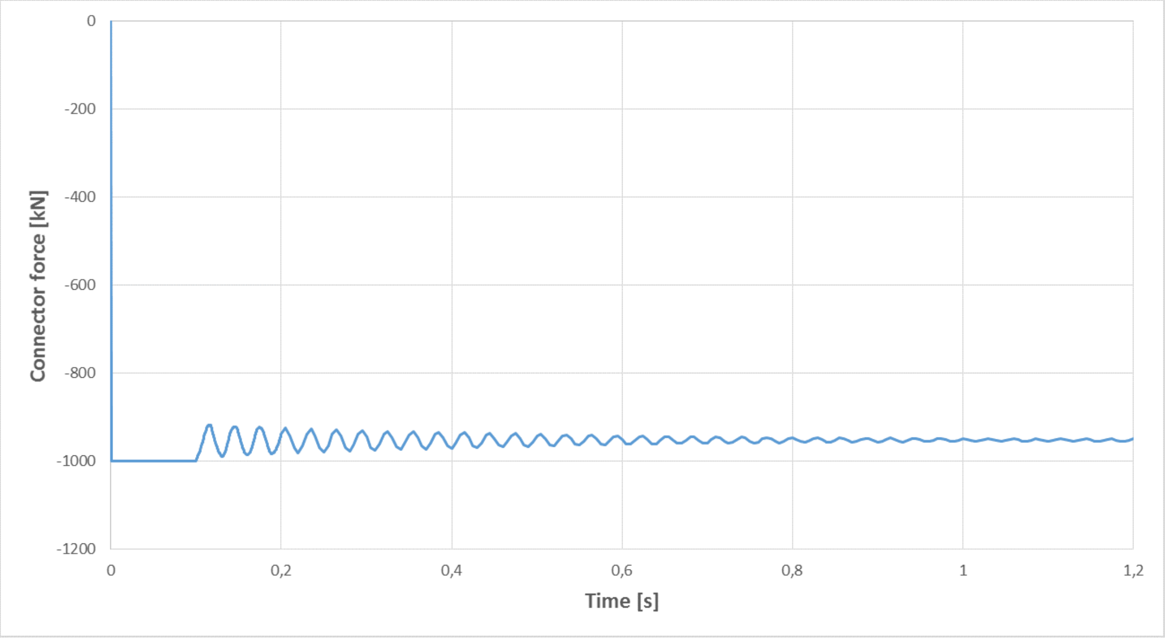

Figure 5.7: The connector force in spring connector 2 including the mass effect.

However, the global dynamic analysis is much more complicated for contact problem.

Chapter 6

Summary and Recommendations for Further Study

6.1 Conclusion

The first part of the thesis performs material comparison and convergence studies, which are performed with the simplified 3D contact model in ABAQUS as the preparation studies. The simplified 3D contact model involves a roller and a plate. The roller rolls on the plate and the nonlinear static analysis have been carried out for this process. Two different load patterns are selected for two types of investigation: force load and displacement boundary condition. For the purpose of the present study, the material of the roller is decided. Consequently, the optimal mesh size is determined in convergence study.

The main part of the thesis presents the results of a nonlinear stress analysis of the interface structure between the spar and the torus in the combined wind and wave energy concept (STC). The "connector-roller-guide" system is modelled to simulate the interface part between the spar the the torus, and the torus is assumed to be rigid compared with the interface part in the model. The contact between the rollers and the spar is stable due to the pre-compression provided by the connectors which are located between the torus and the rollers. To investigate the local interface model performance under different loading conditions, constant loadings are applied to the model. Besides, the proper boundary conditions are applied to simulate the rolling process for the interface part between the spar and the torus. The sensitivity studies are carried out to investigate the effect of different parameters for the interface design. Different scenarios are defined to investigate the effect of structural configurations, connector properties, loading conditions and flat track thickness. Furthermore, in order to investigate the model performance under real sea state, nonlinear loading and boundary conditions are applied instead of the constant loading. Consequently, the horizontal oscillation is investigated for the interface model, which neglects the vertical motion. The structural eigen-frequencies are expected to be much larger than the wave frequencies , therefore, the quasi-static nonlinear analysis is appropriate for the present study. Dynamic analysis is also important to perform in order to investigate the mass effect. Based on the present study, the following conclusions can be drawn:

- For roller material investigation, the present study with the applied contact force load produces the optimal material for roller. Rubber 1 is selected as the roller material for the future work, which is a hyperelastic material with a density of $1500 kg/m^3$, the material constants of $C_{10} = 0.84 MPa$ and $C_{01} = 0.21 MPa$.By comparing Rubber 1 with steel and Rubber 2, Rubber 1 gives the best performance with acceptable average contact pressure and contact area. In addition, Rubber 1 also accords with the compression shear stress test requirement. Therefore, material Rubber 1 is undoubtedly selected as the material for roller .

- In mesh size convergence study, different mesh size combinations are considered for both plate and roller with the applied initial displacement boundary condition. The maximum Von Mises stresses on the contact surface of the plate are plotted in the figure under different mesh size combinations. Firstly, the horizontal axis represents mesh size on the roller. Since the value of the maximum Von Mises stress on the contact surface of the plate becomes stable with the decreasing mesh size on the roller, 0.05m is chosen as the mesh size on roller from the perspective of compromise between calculation duration and solution accuracy. Consequently, the second figure is plotted and the horizontal axis denotes the mesh size on the plate. Analogically, the solution becomes stable as the mesh size decreases on the plate. Ultimately, the mesh size on both roller and plate apply 0.05 m which has sufficient accuracy without intolerable long time calculation.

- For stress analysis of the interface model, the conclusions can be drawn according to different scenarios.

1. Different spar cylinder structural configurations give distinct performance in resisting the external force. The VBHD and T-bar stiffeners located along the rolling direction are significantly effective in reducing the maximum Von Mises stress on the spar cylinder hull, and the combination of vertical and horizontal stiffeners can reduce the largest deformation magnitude on the spar as well. The location of the maximum Von Mises stress and deformation magnitude on the spar varies during the 1.2s simulation time series, but the values are relatively stable under constant loadings. In addition, the T point Y-displacement is not influenced significantly by different structural configurations under the same loading conditions.
2. In terms of increasing positive horizontal force loading (F6-F10), the increments of stress and deformation are more nonlinear than those under negative loading (F1-F5). The T point displacements in Y direction also show nonlinear trend with linearly increasing loading(F1-F10). The deviation of the rollers not only gives rise to nonlinear increments of the stress and deformation but also decreases the contact area between the rollers and the spar. For turning moment, there is no significant nonlinear trend for both increments of stress and deformation. The turning moment also has an insignificant effect on T point displacement in Y direction.
3. The connector stiffness strongly affects the T point motions, and the larger connector stiffness leads to smaller T point motion under the same loading condition. But on the other side, the larger connector stiffness introduces larger induced stress and deformation on the spar. The compromise should be achieved among the stress level, deformation magnitude and T point motions in the future design.
4. The maximum Von Mises stress and maximum deformation magnitude on the spar are reduced significantly by increasing the thickness in the contact region. However, thicker flat track has no influence on the T point motion.

- For the nonlinear analysis under real state without slamming, the trend of stress and deformation on the spar cylinder hull roughly follows the trend of relative heave motion during the 20s simulation time. Similarly, the trend of T point Y-displacement relatively follows the trend of the horizontal interface force.

- In quasi-static analysis, the natural frequency of the horizontal oscillation for the horizontal motion of the T point is much larger than the horizontal force frequency. This means that the wave-induced horizontal interface force is unlikely to excite the resonance of the T point horizontal motion. For lower horizontal force, the interface system performs stiffer in horizontal direction, conversely the interface system becomes more flexible under larger horizontal force. In simple dynamic analysis, the spring connector oscillation is excited if the roller mass is taken into account.

6.2 Discussion

In the stress analysis of the structural interface, many assumptions and simplifications have been made. However, it is significant to give a further discussion about the imperfections in the analysis.

- The steel spar is assumed to be a linear elastic material, which gives a conservative result. Because the steel spar will not fail immediately when the stress reaches the yield stress in real life. For elastic-plastic material, the material is able to sustain more stress before failure rather than yield stress. Therefore, the result based on this type of steel spar is conservative. Generally, the stress condition and distribution on the spar are the focuses in stress analysis, but the rubber rollers may get failed under large sea state as well. Especially, the deformation of the rubber material is most likely to be large, and the overlarge deformation of the rollers can definitely affect the STC concept operation.

- In the numerical modelling part, the torus is replaced by the T point because the torus is considered to be rigid enough compared with the interface system. However, actually the torus in WEC carries the hydrodynamic forces and transfers the load to the spar. If water exit and entry is considered, the upper surface and the lower surface of the torus mainly carry the slamming load. Therefore, the numerical interface model which includes torus will probably give more accurate solution.

- In the present study, the quasi-static analysis is performed, but the inertial force and the damping force in the dynamic equilibrium are not taken into consideration for the system. However, the mass of the torus and the motion of the spar are expected to affect the interface responses. The T point horizontal motion are mainly dominated by the horizontal interface force, and the mass of the torus can intensify the T point motion due to inertial force effect, whereas in the present interface model, the system is relatively stiff and the inertial parameter probably cannot make a great difference. Furthermore, the conditions of rollers should be paid more attention, such as the deformation and the stress on the rollers.

- In this thesis, the constant loading and nonlinear loading are considered, but the slamming and the spar motions are neglected. However, with regard to the STC concept, the large motions of the WEC may occur under large sea state, consequently, water exit and entry may happen and the wave impact is likely to excite the natural frequencies of the structure. Therefore, the quasi-static analysis is not enough to evaluate the performance of the interface design.

6.3 Recommendations for further study

In the present study, the elementary interface structural design and stress analysis are performed. However, there are still some issues with some modelling strategies and conclusions. Many challenges still remain pertaining to the interface design for the STC concept.Hence, further research in the following areas are recommended:

- Although three different materials have been investigated in the present study, it is possible to find a more proper material for roller. More materials may be considered in future work and a material with smaller contact average pressure and contact area should be pursued. Besides, in the present study, the steel spar is assumed to be the linear elastic material. Hence, the plastic effect can be taken into account in later study. The stress and deformation conditions of rollers should also be investigated, so that the rollers will not be failed during the STC service life.

- In the present design, many parameters still need to be investigated, for instance, the amount and arrangement of the rollers , the quantity of the flat tracks or the loading patterns which can have a great impact on the structural responses. Therefore, more scenarios should be made to ensure that this interface design is appropriate enough for the STC concept.

- For the present design, the global analysis should be carried out to investigate the global responses for the integrated STC structure. The integrated model should be established for extreme sea state, which considers the slamming extreme forces and moments on the torus and the bending moment, shear forces on the spar. The dynamic nonlinear stress analysis should be performed for the integrated STC model to investigate the performance of the interface design.

- In the present study, the interface part is the simple "roller-guide system". However, according to the previous studies, some improvements can be made in order to achieve a better interface design. For example, according to one study [7], the roller-guide system can be improved by imitating the train roller-guide system, but the numerical modelling will definitely be more difficult. The interface part certainly can be other modalities in the STC, such as ball bearing system and magnetic bearing system.

Bibliography

[1] Bagbanci, H., Karmakar, D., and Soares, C. (2012). *Review of offshore floating wind turbines concepts*, pages 553–562. CRC Press.

[2] Clément, A., McCullen, P., Falcão, A., Fiorentino, A., Gardner, F., Hammarlund, K., Lemonis, G., Lewis, T., Nielsen, K., Petroncini, S., et al. (2002). Wave energy in europe: current status and perspectives. *Renewable and sustainable energy reviews*, 6(5):405–431.

[3] Hibbit, H., Karlsson, B., and Sorensen, E. (2012). Abaqus user manual, version 6.12. *Simulia, Providence, RI.*

[4] Muliawan, M. J., Karimirad, M., Gao, Z., and Moan, T. (2013a). Extreme responses of a combined spar-type floating wind turbine and floating wave energy converter (stc) system with survival modes. *Ocean Engineering*, 65:71 – 82.

[5] Muliawan, M. J., Karimirad, M., and Moan, T. (2013b). Dynamic response and power performance of a combined spar-type floating wind turbine and coaxial floating wave energy converter. *Renewable Energy*, 50:47–57.

[6] Muliawan, M. J., Karimirad, M., Moan, T., and Gao, Z. (2012). Stc (spar-torus combination): a combined spar-type floating wind turbine and large point absorber floating wave energy converter—promising and challenging. In *ASME 2012 31st International Conference on Ocean, Offshore and Arctic Engineering*, pages 667–676. American Society of Mechanical Engineers.

[7] Okagata, Y. Design technologies for railway wheels and future prospects.

[8] Sclavounos, P. D., L. S., DiPietro, J., P. G. C. P., and De Michele, G. (2010). Floating offshore

wind turbine: tension leg platform and taught leg buoy concept supporting 3-5mw wind turbines. *European wind energy conference(EWEC);2010 Warsaw,Poland.*

[9] Systemes, D. (2013). Abaqus theory manual (6.12). *Dassault Systemes Simulia Corp., Providence, RI, Last accessed Nov*, 9:2013.

[10] Telliskivi, T. and Olofsson, U. (2001). Contact mechanics analysis of measured wheel-rail profiles using the finite element method. *Proceedings of the Institution of Mechanical Engineers, Part F: Journal of Rail and Rapid Transit*, 215(2):65–72.

[11] Telliskivi, T., Olofsson, U., Sellgren, U., and Kruse, P. (2000). A tool and a method for fe analysis of wheel and rail interaction. *Royal Institute of Technology (KTH), Stockholm, Sweden.*

[12] Wan, L., Gao, Z., and Moan, T. (2014). Model test of the stc concept in survival modes. In *ASME 2014 33rd International Conference on Ocean, Offshore and Arctic Engineering*, pages V09AT09A010–V09AT09A010. American Society of Mechanical Engineers.

[13] Wan, L., Gao, Z., and Moan, T. (2015). Experimental and numerical study of hydrodynamic responses of a combined wind and wave energy converter concept in survival modes. *Coastal Engineering*, 104:151–169.

Appendix A

Acronyms

STC	Spar Torus Combination
FWT	Floating Wind Turbine
WEC	Wave Energy Converter
MWL	Mean Water Level
VIM	Vortex Induced Motion
FEM	Finite Element Method
PTO	Power Take-off
B.C.	Boundary Condition
D.O.Fs	Degree of Freedoms
HBHD	Horizontal Bulkhead
VBHD	Vertical Bulkhead
CYL	Cylinder
HRING	Horizontal Ring

Appendix B

The Stress and Deformation Distribution

In chapter4, the effect of different structural configurations of the spar cylinder are investigated. The quasi-static nonlinear stress analysis are carried out for these six different configurations (C1-C6) in ABAQUS. The stress and deformation distribution for different configurations (C1-C6) are shown here:

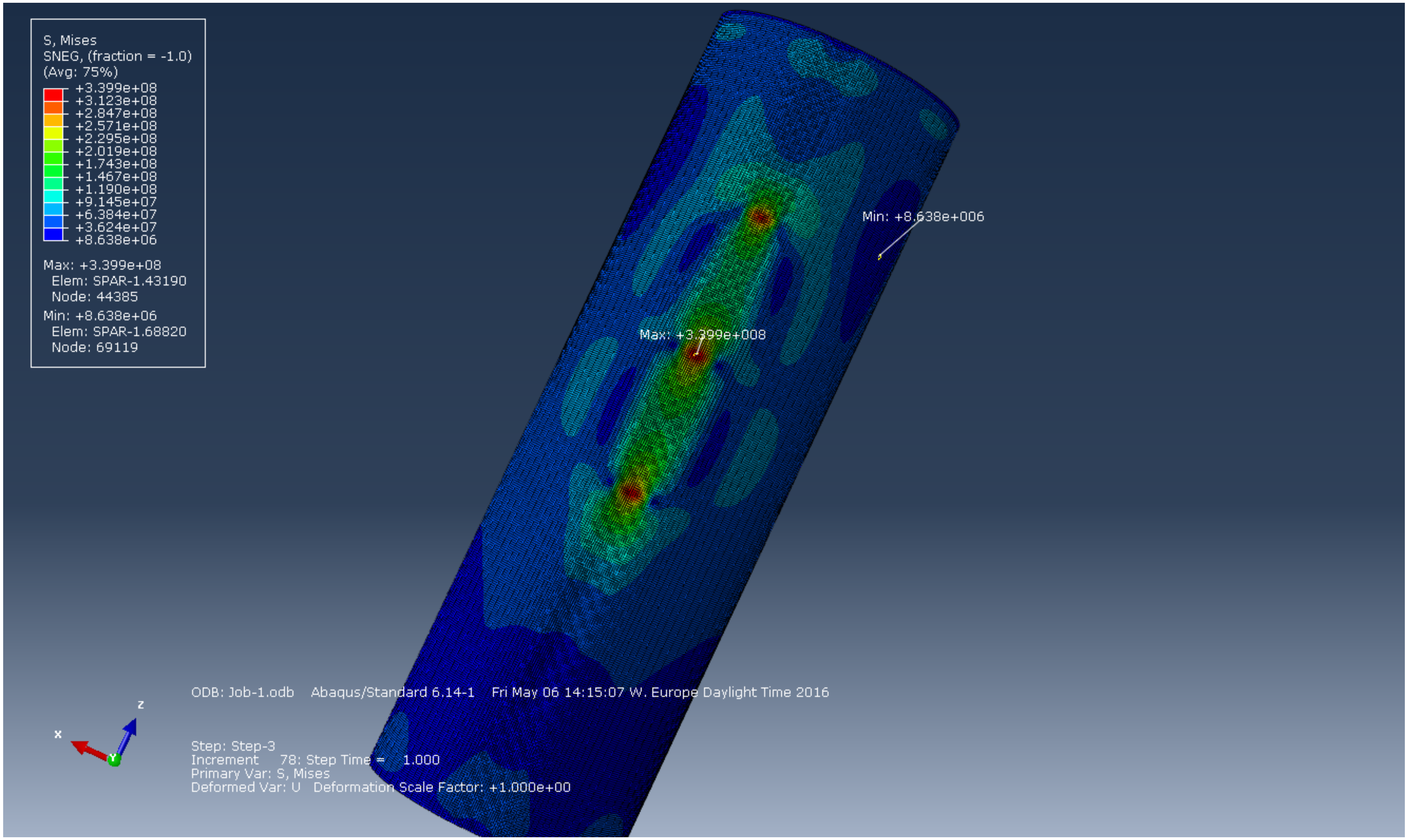

Figure B.1: The Von Mises stress distribution on the spar hull outer surface at 1.2s for C1 under Spring1 and loading F2=-1000kN

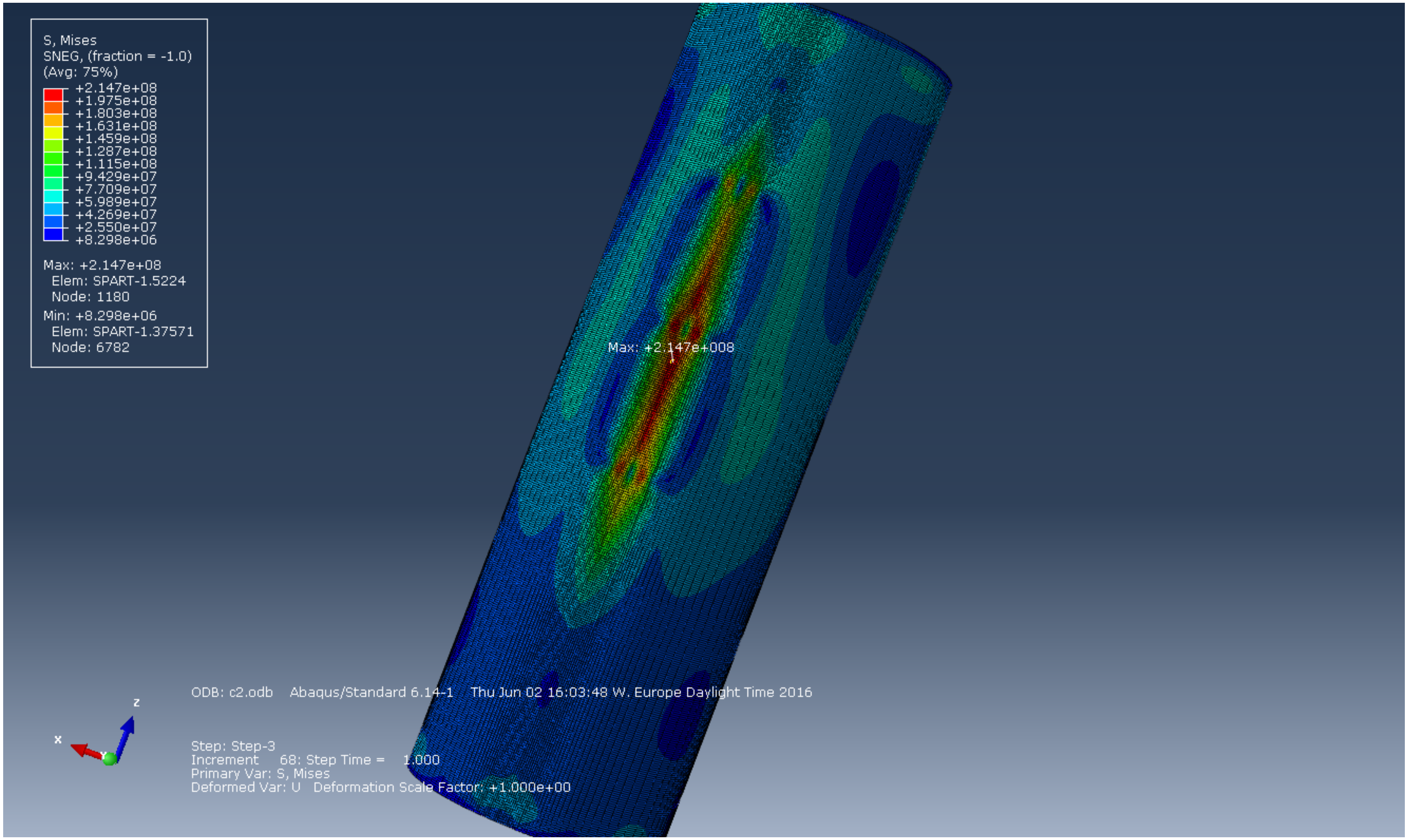

Figure B.2: The Von Mises stress distribution on the spar hull outer surface at 1.2s for C2 under Spring1 and loading F2=-1000kN

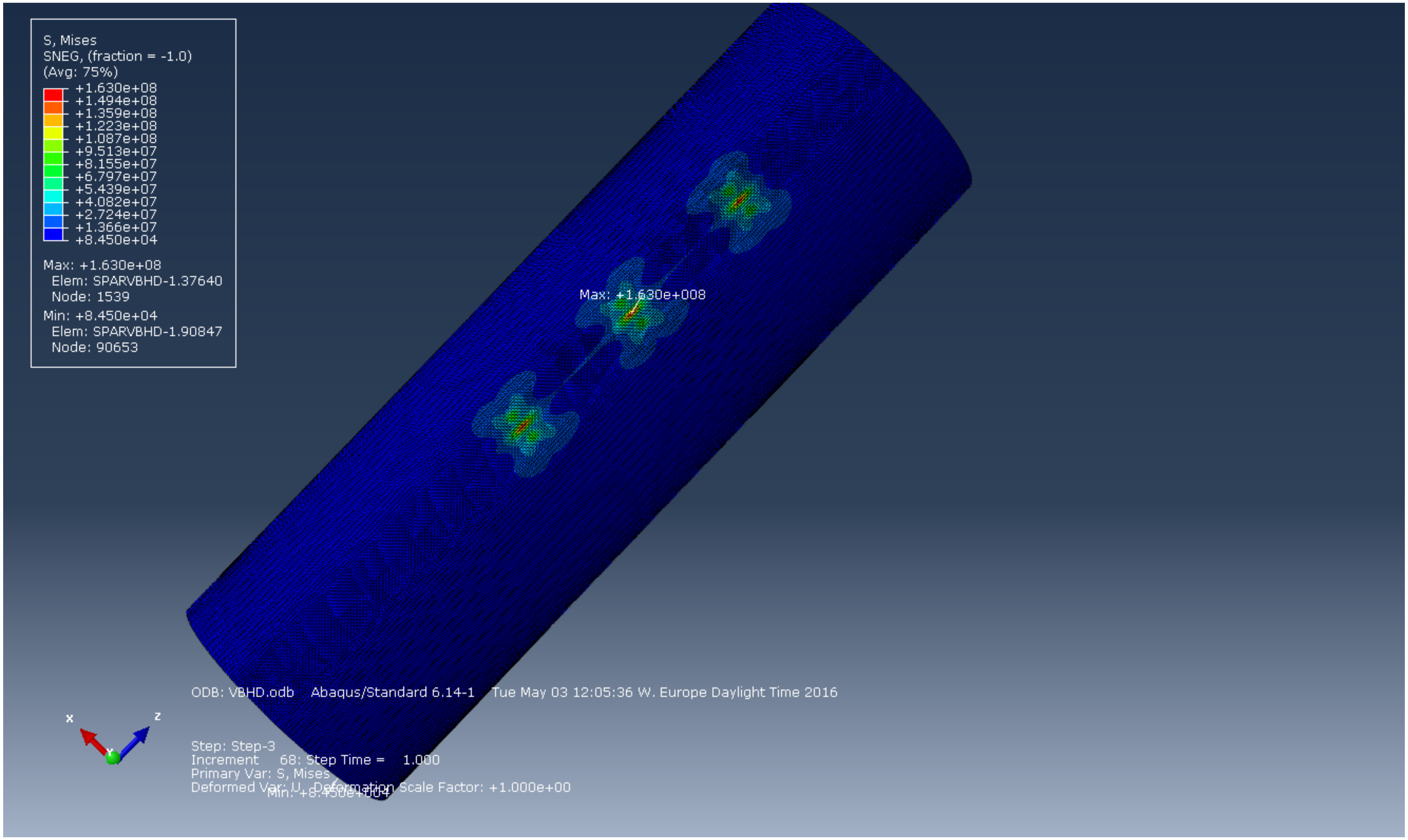

Figure B.3: The Von Mises stress distribution on the spar hull outer surface at 1.2s for C3 under Spring1 and loading F2=-1000kN

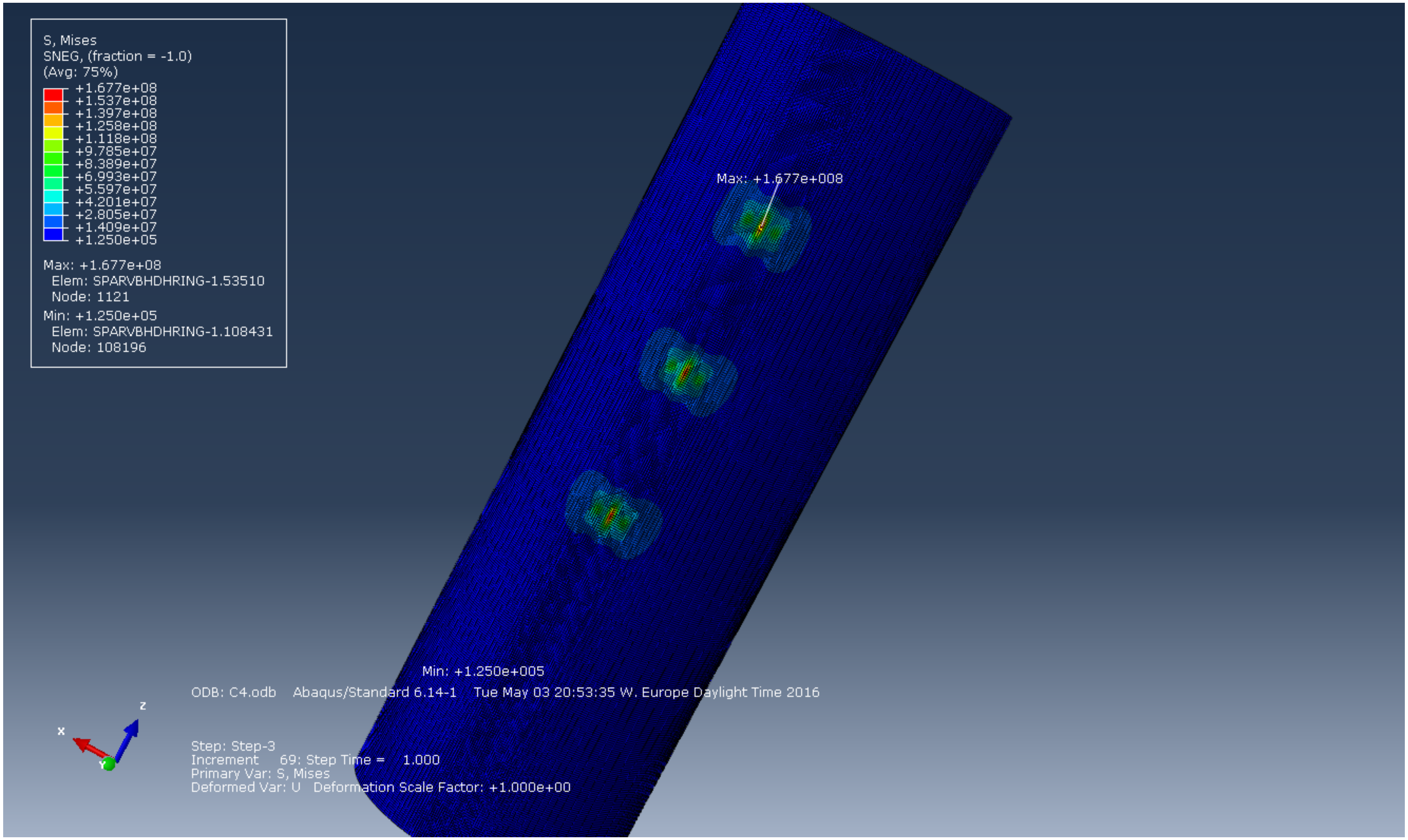

Figure B.4: The Von Mises stress distribution on the spar hull outer surface at 1.2s for C4 under Spring1 and loading F2=-1000kN

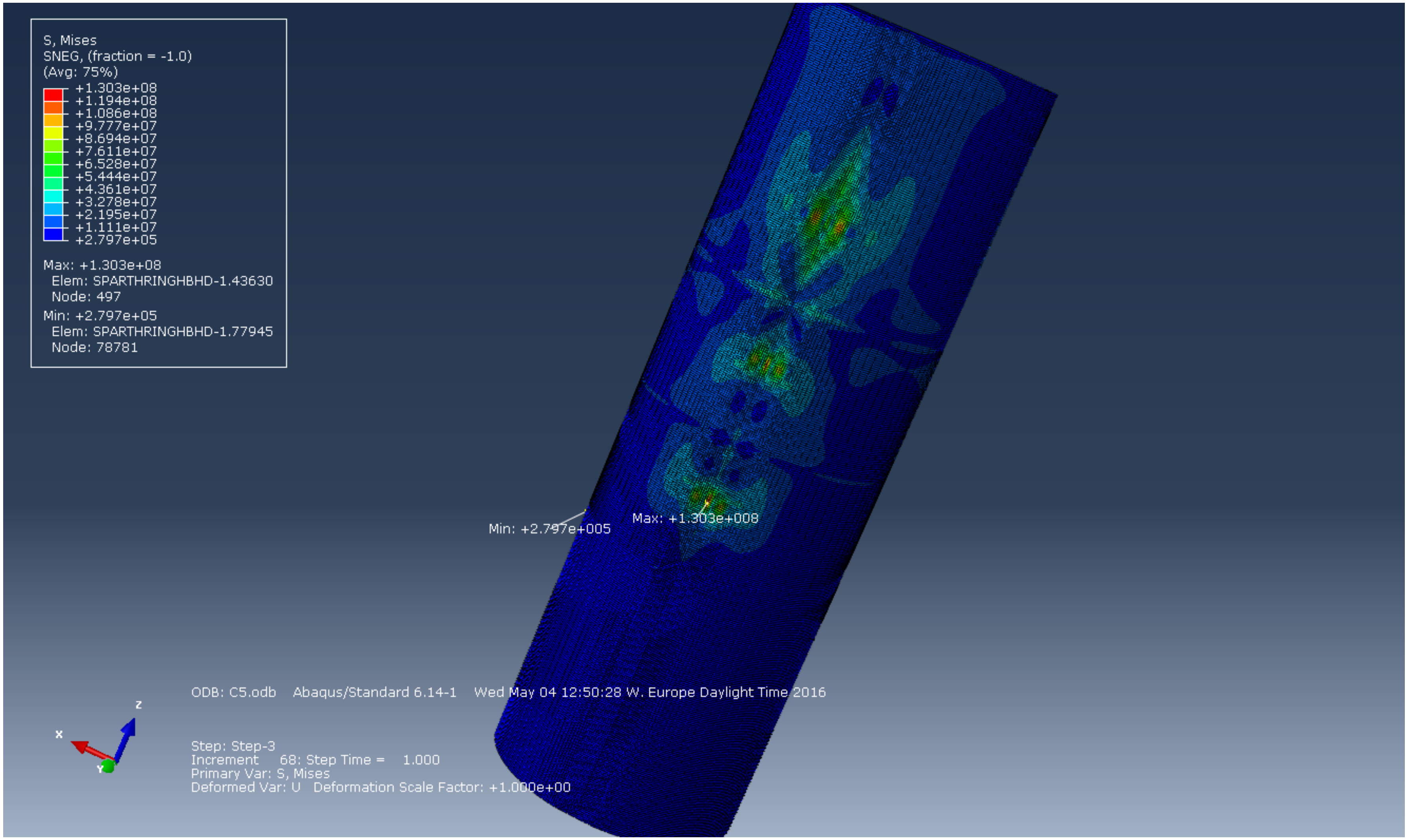

Figure B.5: The Von Mises stress distribution on the spar hull outer surface at 1.2s for C5 under Spring1 and loading F2=-1000kN

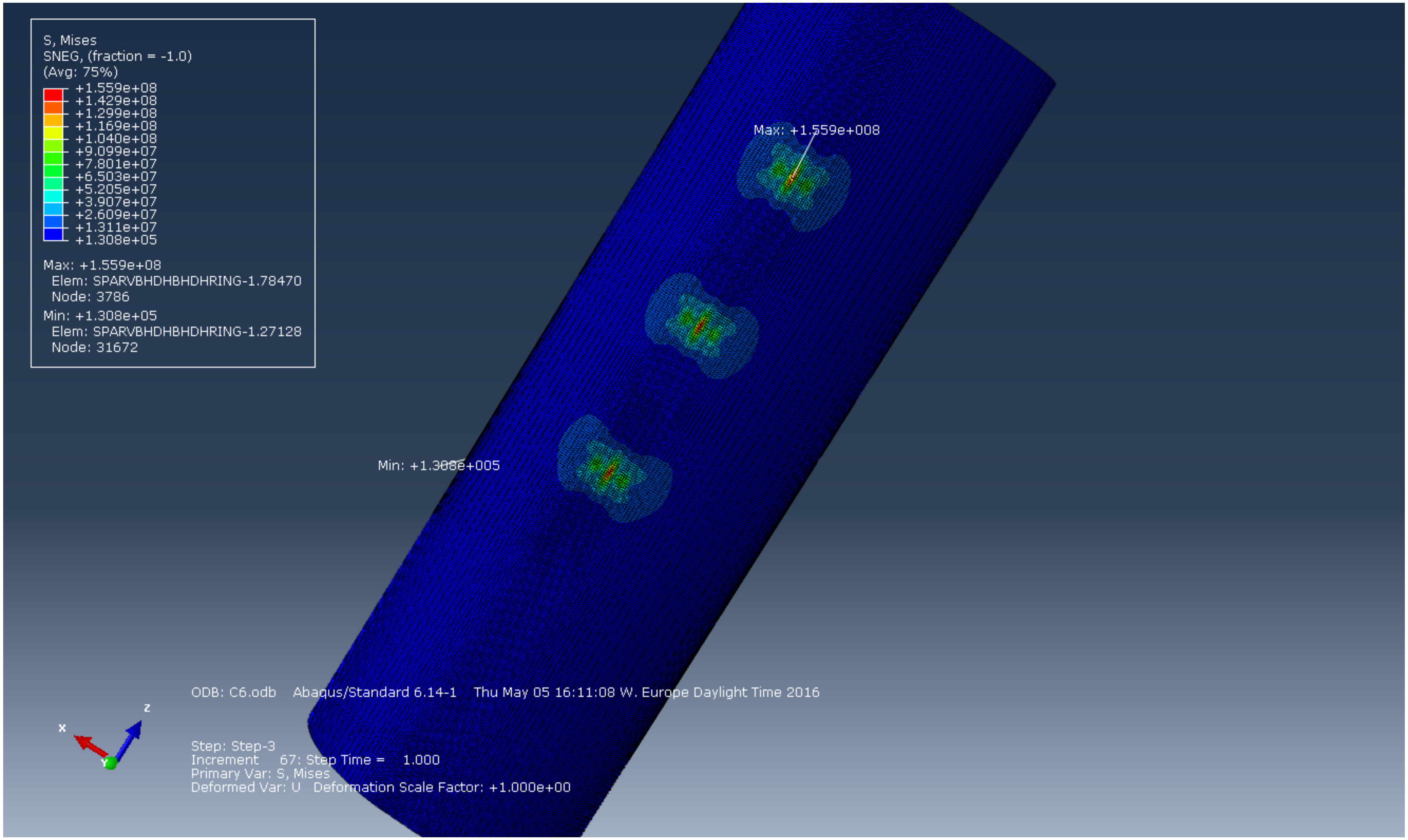

Figure B.6: The Von Mises stress distribution on the spar hull outer surface at 1.2s for C6 under Spring1 and loading F2=-1000kN

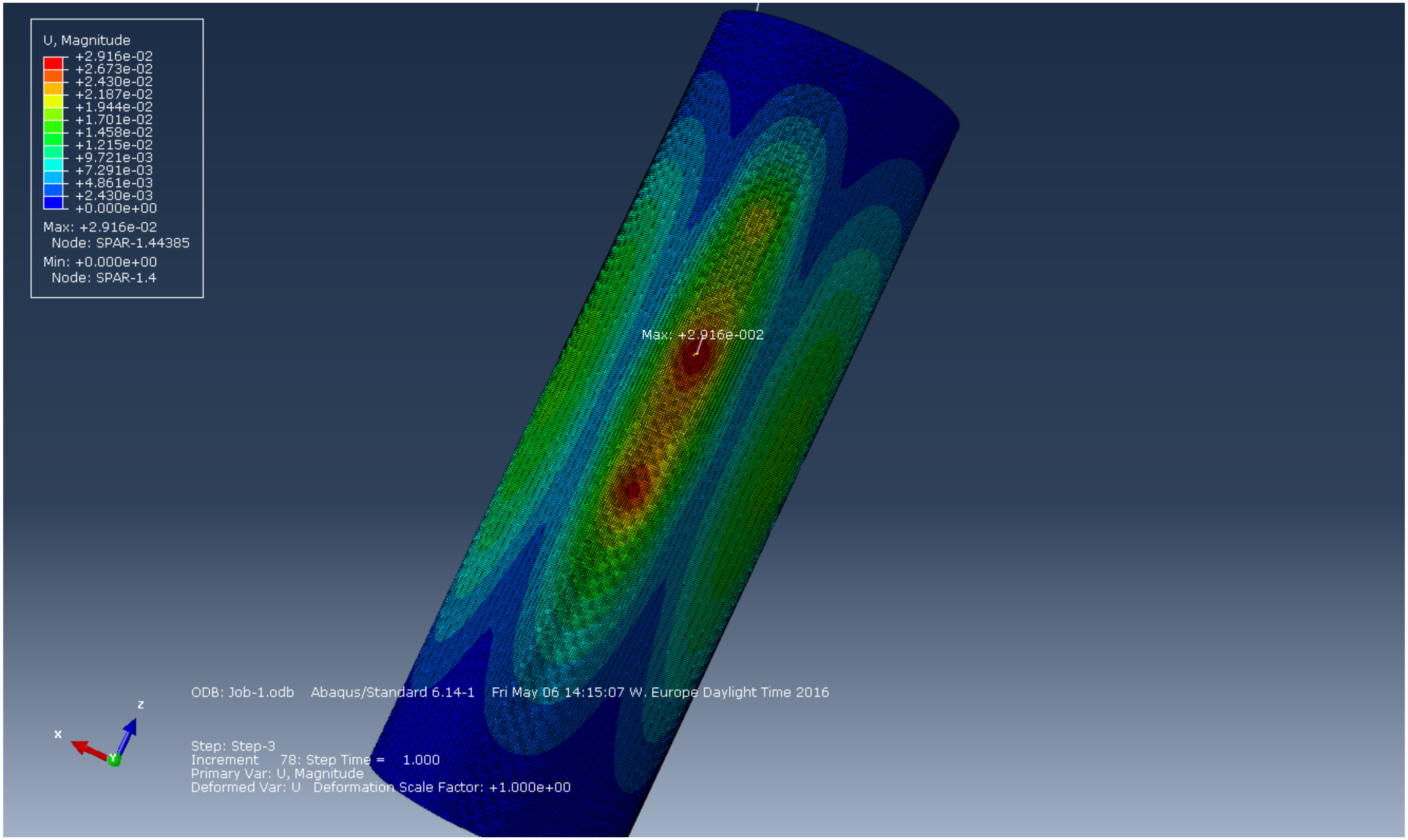

Figure B.7: The deformation magnitude distribution on the spar hull outer surface at 1.2s for C1 under Spring1 and loading F2=-1000kN

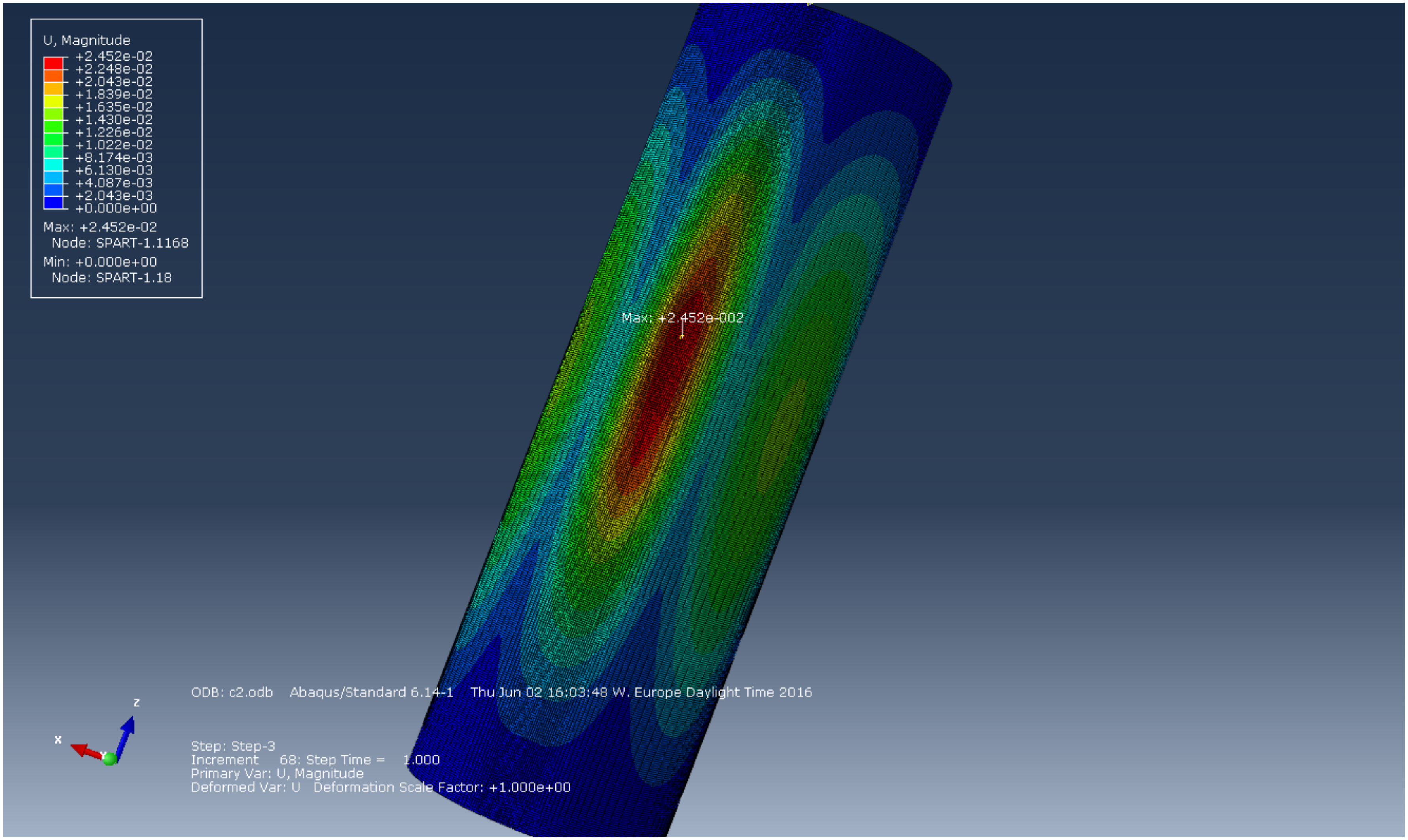

Figure B.8: The deformation magnitude distribution on the spar hull outer surface at 1.2s for C2 under Spring1 and loading F2=-1000kN

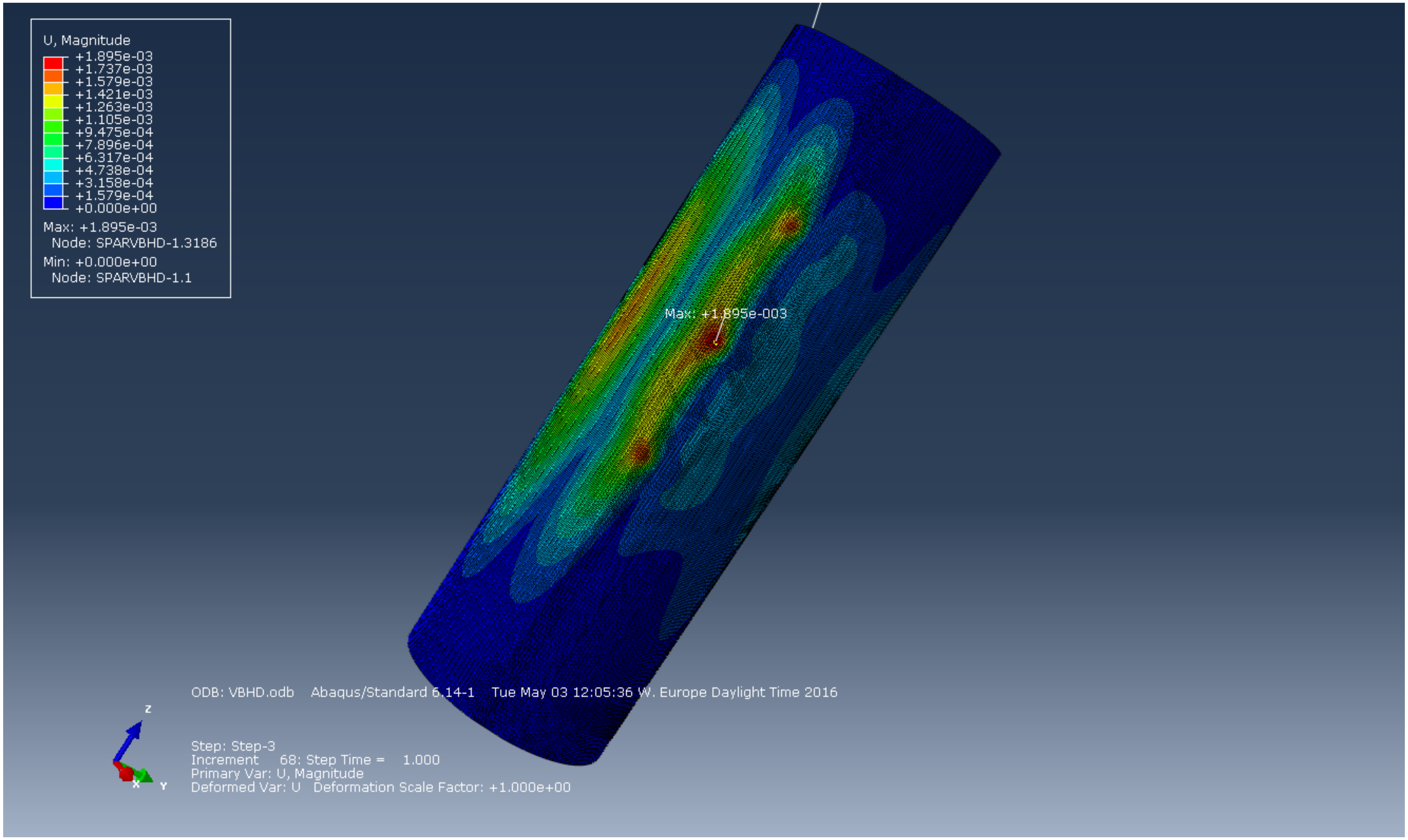

Figure B.9: The deformation magnitude distribution on the spar hull outer surface at 1.2s for C3 under Spring1 and loading F2=-1000kN

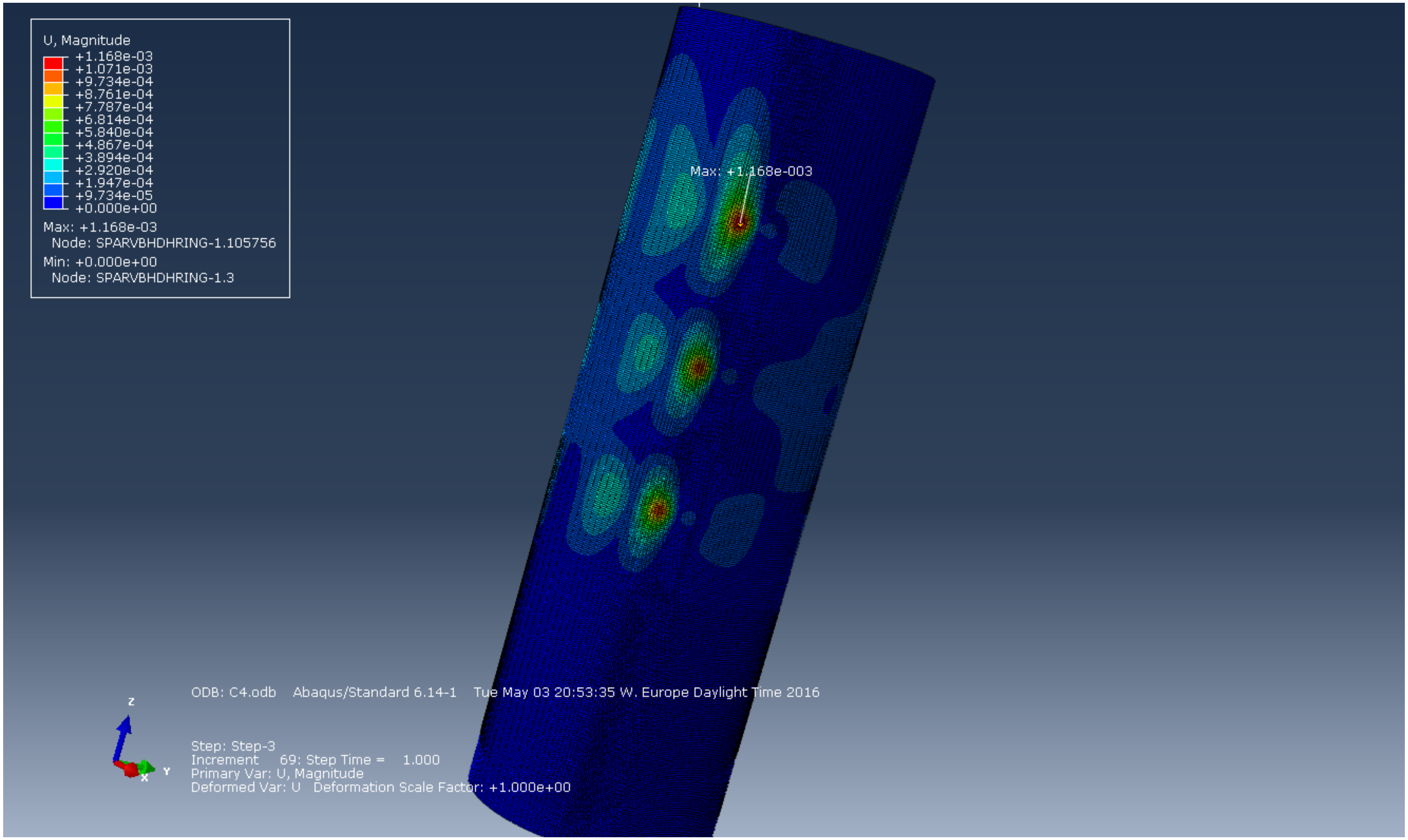

Figure B.10: The deformation magnitude distribution on the spar hull outer surface at 1.2s for C4 under Spring1 and loading F2=-1000kN

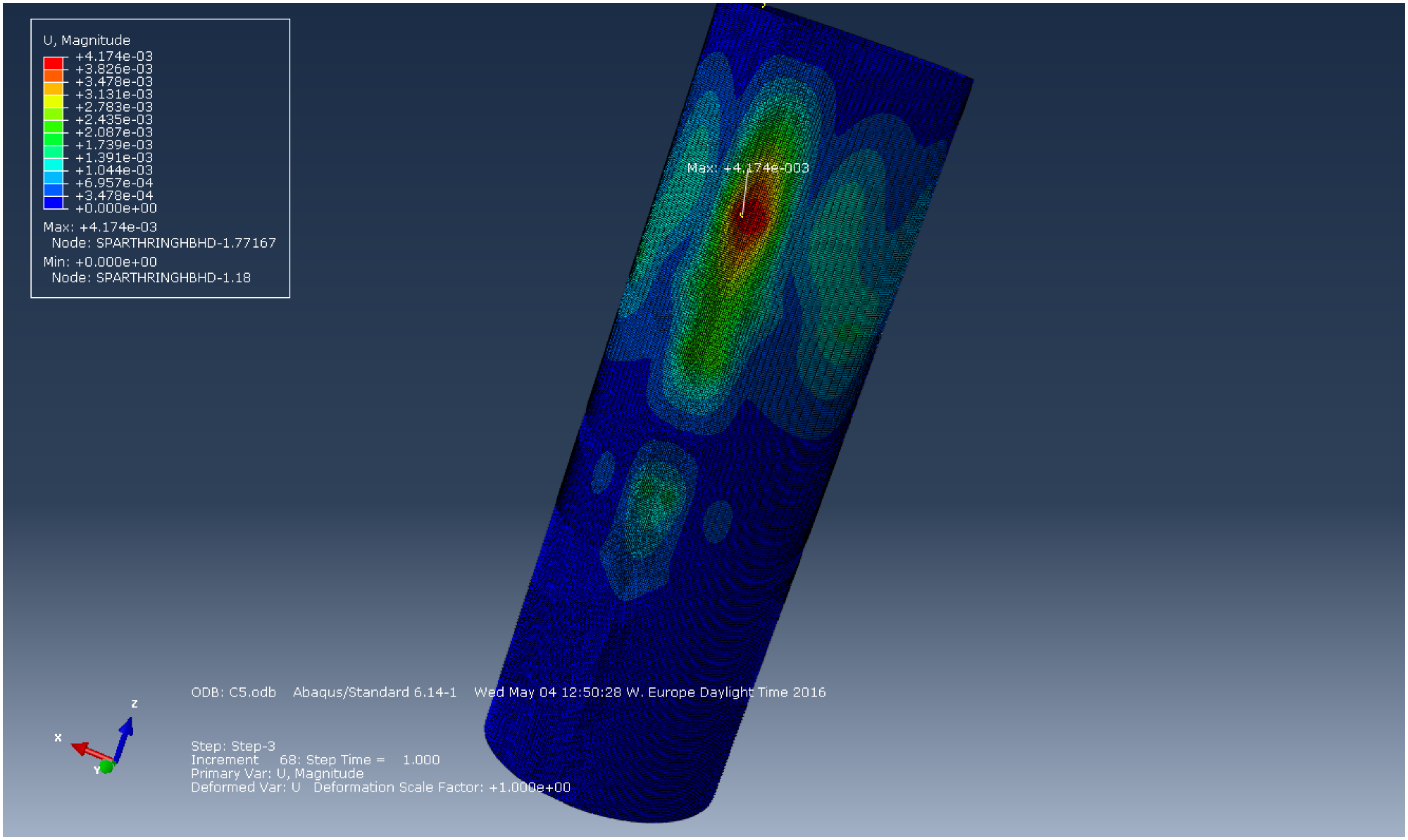

Figure B.11: The deformation magnitude distribution on the spar hull outer surface at 1.2s for C5 under Spring1 and loading F2=-1000kN

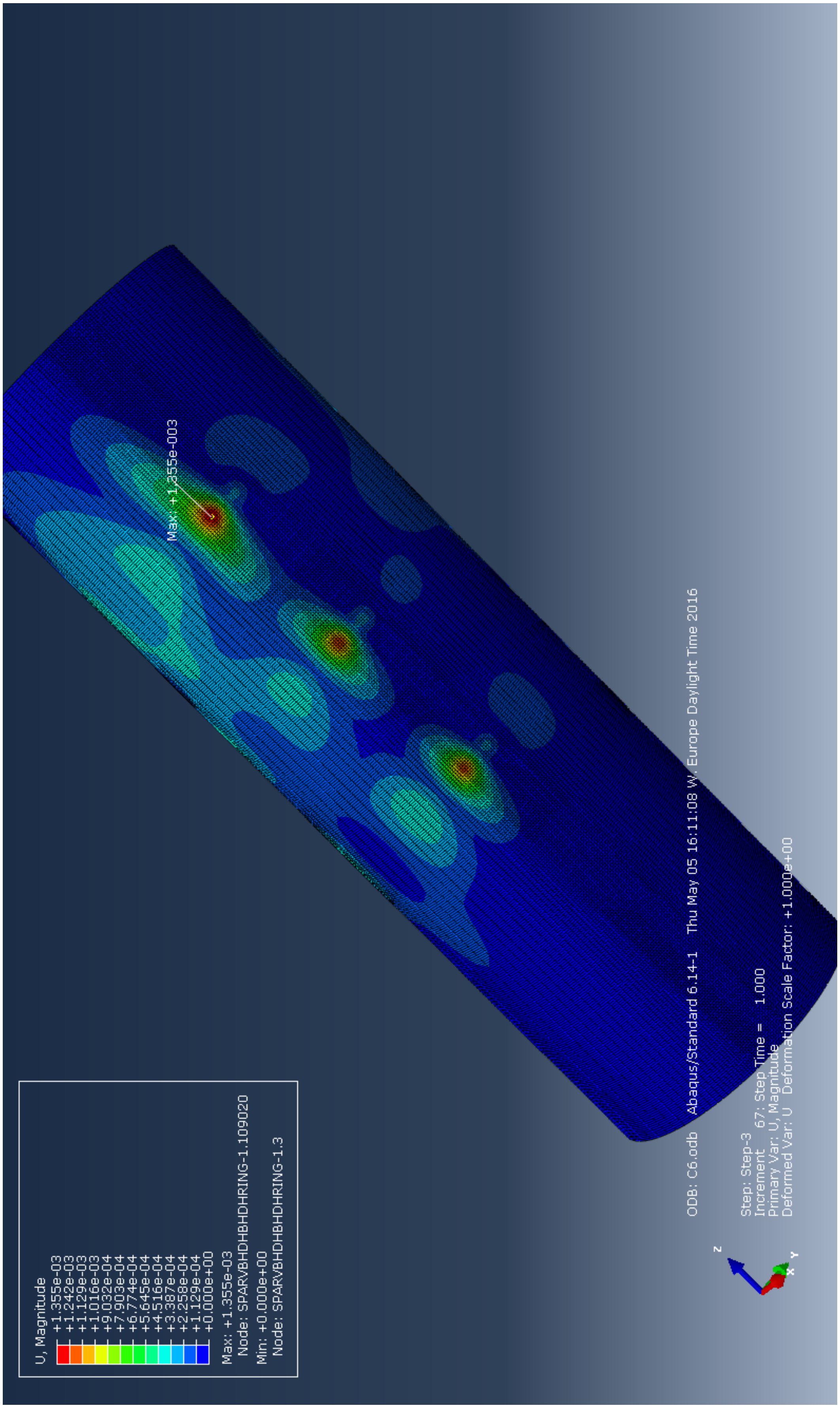

Figure B.12: The deformation magnitude distribution on the spar hull outer surface at 1.2s for C6 under Spring1 and loading F2=-1000kN